

QUENCH SENSITIVITY OF AN Al-Mg-Si-Cu ALUMINUM ALLOY

by

Naveen Sundaresan Ramesh

B.Tech., Indian Institute of Technology Madras, 2018

A THESIS SUBMITTED IN PARTIAL FULFILLMENT OF
THE REQUIREMENTS FOR THE DEGREE OF

MASTER OF APPLIED SCIENCE

in

THE FACULTY OF GRADUATE AND POSTDOCTORAL STUDIES
(Materials Engineering)

THE UNIVERSITY OF BRITISH COLUMBIA
(Vancouver)

April 2021

© Naveen Sundaresan Ramesh, 2021

The following individuals certify that they have read, and recommend to the Faculty of Graduate and Postdoctoral Studies for acceptance, the thesis entitled:

Quench sensitivity of an Al-Mg-Si-Cu aluminum alloy

submitted by Naveen Sundaresan Ramesh in partial fulfillment of the requirements for

the degree of Master of Applied Science

In Materials Engineering

Examining Committee:

Dr. Warren J. Poole, Department of Materials Engineering, UBC
Supervisor

Dr. Anoush Poursartip, Department of Materials Engineering, UBC
Supervisory Committee Member

Dr. Ben Britton, Department of Materials Engineering, UBC
Supervisory Committee Member

Abstract

The use of aluminum extrusion alloys in automotive applications is increasing due to the requirement that vehicle weight be reduced. One of the steps involved in the processing of aluminum extrusion alloys is rapid cooling (or quenching) after the solution heat treatment. The term quench sensitivity refers to the relationship between mechanical properties and the cooling rate after solution treatment. In this study, two initial microstructures were produced from the as-received alloy using different thermomechanical processing routes to study quench sensitivity: in the first case, the as-received microstructure underwent a solution treatment of 5 minutes at 550 °C to produce a predominantly unrecrystallized grain structure, and in the second case, the material was rolled at room temperature prior to a solution treatment of 5 minutes at 550 °C to produce a recrystallized grain structure.

The main objective of this study was to measure the quench sensitivity of the two initial microstructures. The variation of hardness with cooling rates was examined using a modified Jominy test, and the variation of yield strength and ultimate tensile strength with quench rates was characterized using tensile tests. Hardness, yield strength, ultimate tensile strength and ductility were found to decrease with decreasing cooling rates. The reduction in the mechanical properties was attributed to the loss of solute atoms which precipitates as coarse precipitates during slow cooling. Slow cooling typically results in a higher number of grain boundary precipitates and a wider precipitate free zone (PFZ) adjacent to the grain boundary, which increases the propensity of intergranular fracture. Finally, using a polycrystal plasticity model, the degree of strain localization within the PFZs was studied for different idealized geometries.

Lay Summary

Aluminum is gaining popularity in automobile industries to produce lighter vehicles. This increases the vehicle's fuel efficiency, reducing its environmental impact. Pure aluminum is not strong enough to be used in automotive applications. Thus, certain alloying elements are added to improve its strength and ductility. In the current study, Mg, Si and Cu are added. To achieve the maximum strength, the alloy must be heat treated. This involves heating the alloy to 550 – 560 °C and holding for several minutes, followed by controlled cooling to room temperature. It is known that higher cooling rates have higher strengths, however, high cooling rates can cause undesirable distortions in the material. Therefore, there is a need to tailor the cooling conditions to the application. The main objective of this work is to study the effect of processing parameters: cooling rates and the initial microstructure on the final performance of the alloys.

Preface

The majority of this study was conducted by Naveen Sundaresan Ramesh at The University of British Columbia under the supervision of Dr. Warren J. Poole. The extruded materials for this project were provided by Dr. Nick Parson from Rio Tinto Aluminum, Canada. The size measurements of dispersoids and constituent particles were provided by Dr. Zhijun Zhang from the Materials Engineering department, The University of British Columbia. The TEM work was conducted by Dr. Xiang Wang at McMaster University. Furthermore, the initial microstructure for the simulations was provided by Ali Khajezade from the Materials Engineering department at The University of British Columbia.

Table of Contents

Abstract.....	iii
Lay Summary	iv
Preface.....	v
Table of Contents	vi
List of Tables	xi
List of Figures.....	xiii
List of Symbols	xx
List of Abbreviations	xxi
Acknowledgements	xxiii
Chapter 1: Introduction	1
Chapter 2: Literature Review.....	4
2.1 Introduction.....	4
2.2 Processing of AA6xxx alloys.....	4
2.3 Casting	5
2.4 Homogenization.....	8
2.5 Reheat and extrusion.....	10
2.6 Cooling after extrusion	11
2.7 Ageing.....	12
2.7.1 Natural ageing.....	15
2.7.2 Artificial ageing	15

2.8	Quench Sensitivity	16
2.8.1	Factors affecting quench sensitivity.....	17
2.8.1.1	Cooling rates	17
2.8.1.1.1	Modeling of precipitates during cooling.....	20
2.8.1.1.2	Formation of precipitate free zones at grain boundaries	21
2.8.1.2	Effects of alloying elements.....	23
2.8.1.3	Effects of natural ageing after extrusion	24
2.8.1.4	Effects of dispersoids.....	24
2.8.1.5	Role of deformed structure.....	25
2.9	Fracture	26
2.9.1	Localization at the PFZ.....	30
2.10	Crystal plasticity simulations.....	32
Chapter 3: Scopes and Objectives.....		33
3.1	Scope.....	33
3.2	Objectives	33
Chapter 4: Methodology.....		35
4.1	Introduction.....	35
4.2	Initial material.....	35
4.3	Removal of PCG layer	38
4.4	Solution heat treatment and cold rolling.....	39
4.5	Modified Jominy test and hardness testing.....	40
4.6	Heat treatment of tensile samples	41
4.6.1	Water quenched and air cooled conditions	41

4.6.2	Intermediate cooling rates - Gleeble	42
4.7	Ageing.....	44
4.8	Tensile test	44
4.9	Microstructure characterization	46
4.9.1	Metallography	46
4.9.2	Scanning Electron Microscope (SEM)	46
4.9.3	Fracture surfaces	48
4.9.4	Electron Backscattered diffraction (EBSD).....	49
4.10	Polycrystal plasticity model.....	51
4.10.1	Microstructure of the model material	51
4.10.2	Constitutive laws.....	52
4.10.2.1	Elasticity.....	52
4.10.2.2	Plasticity	52
4.10.3	Parameter fit.....	53
4.10.4	Boundary condition.....	55
4.10.5	Coordinate transformation	55
Chapter 5: Results.....		56
5.1	Introduction.....	56
5.2	Initial microstructure and texture.....	56
5.3	Thermomechanical processing.....	58
5.3.1	As extruded and solution treatment	58
5.3.2	Cold rolled and solution treatment.....	60
5.4	Modified Jominy test	63

5.5	Observations on grain boundary precipitation	65
5.5.1	Recrystallized alloys	66
5.5.2	Unrecrystallized alloys.....	72
5.6	Stress-Strain response	74
5.7	Fracture surfaces	83
5.7.1	Recrystallized alloys	83
5.7.2	Unrecrystallized alloys.....	85
Chapter 6: Discussion		88
6.1	Mechanical properties.....	88
6.1.1	Fracture	90
6.2	Polycrystal plasticity.....	94
6.2.1	Observations on strain localization when PFZs are parallel and at 60° to the loading axis	95
6.2.1.1	Effect of far-field strain	97
6.2.1.2	Shear and normal strains in the coordinate system of the grain boundary ..	98
6.2.1.3	Distribution of hydrostatic stress.....	99
6.2.1.4	Effect of the ratio of flow stress in PFZ to grain interior.....	99
6.2.1.5	Effect of PFZ width.....	100
6.2.2	Observations on strain localization when PFZs are perpendicular and at 30° to the loading axis	102
6.2.2.1	Shear and normal strains in the coordinate system of the grain boundary	103
6.2.2.2	Distribution of hydrostatic stress.....	104
6.3	Effect of copper.....	105

Chapter 7: Summary and recommendations for future work.....	109
7.1 Summary	109
7.2 Recommendations for future work	110
References	112
Appendices.....	122
Appendix A.....	122
Appendix B	124

List of Tables

Table 2.1 Precipitate phases in a Al-Mg-Si system [19]	13
Table 2.2 Precipitate phases in a Al-Mg-Si-Cu system [23]	14
Table 4.1 Chemical composition of the initial alloy in wt.% (as measured by optical spectroscopy)	35
Table 4.2 Initial He pressure used for different quench rates	43
Table 4.3 Various parameters used in EBSD.....	49
Table 4.4 Bunge Euler angles for different texture components	50
Table 4.5 Parameters used in the phenomenological model [82]	53
Table 4.6 Parameters for the constitutive law for grain interior and PFZ	54
Table 5.1 Comparison of main texture components and sub-grain size for the as-received and solution treated samples, note: texture components are given in volume fraction (%)	58
Table 5.2 Summary of the major texture components for the recrystallized microstructure, note: texture components are given in volume fraction (%).....	62
Table 5.3 Cooling rates calculated as a function of distance measured from the water line for the recrystallized sample.....	63
Table 5.4 Cooling rates calculated as a function of distance measured from the water line for the unrecrystallized sample.....	63
Table 5.5 Size of grain boundary precipitates as a function of cooling rates for a recrystallized alloy.....	68
Table 5.6 Size of grain boundary precipitates as a function of cooling rates for an unrecrystallized alloy	73
Table 5.7 Summary of change in mechanical properties from >2000 °C/s to 4-5 °C/s	80

Table 5.8 Percentage of intergranular fracture, yield strengths and true fracture strains at different cooling rates for a T6 recrystallized microstructure 83

List of Figures

Figure 2.1 Temperature-time history of an aluminum extrusion alloy [6]	5
Figure 2.2 Vertical DC casting, 1-feed nozzle, 2-nozzle, 3-float valve, 4-distributor, 5-mold, 6-solidifying ingot, 7-sump, 8-water cooling sprays, 9-stool cap, 10-stool [7]	6
Figure 2.3 As-cast microstructure of alloy AA6002 with 0.6 wt.% Cu [9].....	7
Figure 2.4 An as-cast microstructure with intermetallics [10]	8
Figure 2.5 Microstructure of (a) as-cast and (b) homogenized at 590 °C for 32 hours of an Al 0.83-Si 0.7-Mg 0.18-Mn 0.27-Fe and 0.02 Zn (compositions in wt.%) [13]	9
Figure 2.6 Graph of preheat rates and the zones of β and β' formation [6]	11
Figure 2.7 Variation of hardness with quench rates for four AA6xxx alloys, with AA6060 (Al 0.43-Si 0.45-Mg 0.18-Fe), AA6005A (Al 0.73-Si 0.53-Mg 0.12-Cu 0.18-Fe 0.1-Mn), AA6061 (Al 0.62-Si 0.87-Mg 0.25-Cu 0.21-Fe 0.13-Mn 0.1-Cr) and AA6082 (Al 1.05-Si 0.75-Mg 0.05-Cu 0.15-Fe 0.6-Mn) (Note: compositions are in wt.%) [47]	17
Figure 2.8 DSC curves for cooling rates between 0.1 K/min to 375 K/min for the alloy EN AW-6005A [48].....	18
Figure 2.9 Grain boundary precipitation of Q phase in a AA6xxx alloy with Cu [52]	19
Figure 2.10 Precipitation of β phase on a dispersoid particle in a AA6xxx alloy [35].....	19
Figure 2.11 Computed isothermal transformation diagrams for four AA6xxx alloys, A1 and A2 (Al 0.98-Si 0.64-Mg 0.52-Mn 0.19-Fe) B (Al 1.32-Si 0.62-Mg 0.5-Mn 0.24-Fe), C (Al 0.69-Si 0.63-Mg 0.49-Mn 0.21-Fe) [53]	20
Figure 2.12 Dependence of PFZ width on the critical vacancy concentration X_V^C and quench rate [55].....	21

Figure 2.13 Simulation of the distribution and coarsening of particles, and the formation of precipitate free zones adjacent to the grain boundaries, at a normalized time of (a) 1 (b) 5000 (c) 8000 and (d) 9000 [56]	22
Figure 2.14 Tensile strength as a function of median cooling time (τ), showing the effect of Mn, Cr and Zr on quench sensitivity [18]	25
Figure 2.15 Transgranular and intergranular type of fracture under tensile stress [63]	28
Figure 2.16 Schematic of the deformation processes (a) with PFZ and (b) without PFZ [73].....	28
Figure 2.17 Summary of Drucker's 2D model [70] of uniform hexagonal particles separated by a perfectly-plastic matrix [76]	30
Figure 2.18 Strain localization on a grain boundary for (a) water quenched condition and (b) slow cooled samples [77].....	31
Figure 4.1 Schematic of the extrusion press, the feeder plate and the die used in the extrusion [83].....	36
Figure 4.2 Size distribution of the constituent particles present in the (a) as-cast condition and (b) as homogenized at 550 °C for 2 hours	36
Figure 4.3 Size distribution of the dispersoids present in alloy A612	37
Figure 4.4 Optical microscope image of the as-extruded microstructure, etched with Baker's reagent and viewed under polarized light (from Rio Tinto Aluminium).....	38
Figure 4.5 Variation of sample thickness with etching time for the initial material	39
Figure 4.6 Sample used for the modified Jominy tests.....	40
Figure 4.7 (a) Gleeble testing setup (b) Gleeble sample held by steel grips	42
Figure 4.8 Quench head used in the Gleeble heat treatment.....	42
Figure 4.9 Samples used for Gleeble tests	43

Figure 4.10 Geometry used for the tensile test samples	44
Figure 4.11 (a) An example of a fracture surface image taken using SEM and (b) traced edges of the fracture surface image shown in (a).....	45
Figure 4.12 Setup used for electro-etching.....	47
Figure 4.13 (a) An example of a grain boundary precipitate image taken using SEM and (b) traced precipitate particles from (a)	48
Figure 4.14 An example of a fracture surface image used to identify the mode of fracture	49
Figure 4.15 Microstructure used in the plastic deformation model.....	51
Figure 4.16 Parameter fitting from the stress strain data.....	54
Figure 5.1 Characterization of the as-received alloy (a) inverse pole figure map (b) 001, 011 and 111 pole figures and (c) histogram of the sub-grain size distribution	57
Figure 5.2 Characterization of the as-received alloy after a solution treatment of 5 min at 550 °C (a) inverse pole figure map (b) 001, 011 and 111 pole figures and (c) histogram of the sub-grain size distribution.....	59
Figure 5.3 Characterization of the as-received alloy that was cold rolled and solution treated at 550 °C for 5 min (a) inverse pole figure map (b) 001, 011 and 111 pole figures and (c) histogram of the sub-grain size distribution.....	61
Figure 5.4 (a) Large area EBSD IPF map of a recrystallized microstructure (b) 001, 011 and 111 pole figures.....	62
Figure 5.5 Cooling curves measured from the modified Jominy quench test for (a) recrystallized and (b) unrecrystallized microstructure	64
Figure 5.6 Comparison of Vickers hardness with cooling rate for recrystallized and unrecrystallized microstructures (measured within 10 minutes of the quench)	65

Figure 5.7 Secondary electron SEM micrographs of recrystallized microstructure at different cooling rates (a) water quenched (b) 112 °C/s (c) 32 °C/s (d) ≈ 7 °C/s (AC) (T4) 67

Figure 5.8 FEGSEM micrograph of a water quenched recrystallized microstructure (a) back scattered electron image (b) secondary electron image (T4) 68

Figure 5.9 FEGSEM micrograph of a recrystallized microstructure cooled at ≈ 7 °C/s (a) secondary electron image (b) back scattered electron image (T4) 69

Figure 5.10 High-angle annular dar-field (HAADF) image of a T4 recrystallized sample cooled at 10 °C/s [87] 70

Figure 5.11 (a) Energy dispersive spectroscopy (EDS) data for the grain boundary particle (blue arrow) (b) EDS data for a point in the grain interior (orange arrow) (c) Selected area diffraction (SAD) pattern for the grain boundary precipitate, indicated by a blue arrow, observed in a T4 tempered A612 recrystallized sample, cooled at 10 °C/s [87] 71

Figure 5.12 Secondary electron SEM micrographs of unrecrystallized microstructure at different cooling rates (a) water quenched (b) 198 °C/s (c) 33 °C/s (d) ≈ 7 °C/s (AC) (T4).....72

Figure 5.13 Variation of average major axis size of grain boundary precipitates for recrystallized and unrecrystallized microstructures, note: for the cooling rate of 2000 °C/s, the data points have been slightly offset so they can more easily be seen in the graph. For both cases no GB precipitation were observed, i.e., the major axis size = 0 73

Figure 5.14 Variation of number density of precipitates per grain boundary, for recrystallized and unrecrystallized microstructures, note: for the cooling rate of 2000 °C/s, the data points have been slightly offset so they can more easily be seen in the graph. For both cases no GB precipitation were observed, i.e., the number density = 0 74

Figure 5.15 T4 tensile testing results; engineering stress - engineering strain for (a) recrystallized and (c) unrecrystallized; true Stress - true Strain (b) recrystallized and (d) unrecrystallized.....	75
Figure 5.16 T6 tensile testing results; engineering stress - engineering strain for (a) recrystallized and (c) unrecrystallized; true stress - true strain for (b) recrystallized and (d) unrecrystallized ..	76
Figure 5.17 Variation of yield strength with cooling rate for both unrecrystallized and recrystallized microstructures for (a) T4 temper and (b) T6 temper	77
Figure 5.18 Variation of ultimate tensile strength with cooling rate for both unrecrystallized and recrystallized microstructures for (a) T4 temper and (b) T6 temper	79
Figure 5.19 T4 temper (a) Variation of true fracture stress with cooling rate (b) Variation of true fracture strain with cooling rate	81
Figure 5.20 T6 temper (a) Variation of true fracture stress with cooling rate (b) Variation of true fracture strain with cooling rate	82
Figure 5.21 Variation of true fracture strain with yield stress for a T4 tempered recrystallized material	84
Figure 5.22 Variation of true fracture strain with yield stress for a T6 tempered recrystallized material	85
Figure 5.23 High magnification fracture surface images of unrecrystallized microstructure cooled at (a) >2000 °C/s and (b) 10 °C/s	86
Figure 5.24 Variation of true fracture strain with yield stress for a T4 tempered unrecrystallized material	87
Figure 5.25 Variation of true fracture strain with yield stress for a T6 tempered unrecrystallized material	87

Figure 6.1 Decrease in yield strength with respect to the water quenched condition, versus cooling rates for a recrystallized and unrecrystallized microstructure; (a) T4 and (b) T6 tempered	89
Figure 6.2 Variation of true fracture strain with yield stress. Note: Arrows indicate decreasing cooling rate.....	91
Figure 6.3 Variation of percentage of intergranular fracture for a T6 recrystallized microstructure with (a) true fracture strain and (b) cooling rate	92
Figure 6.4 Macroscopic tensile curve of the initial microstructure with the presence of PFZs ...	94
Figure 6.5 Contour plot of the normalized strain for $a/h = 85$ with a uniaxial tensile load parallel to the grain boundary	95
Figure 6.6 Magnitude of normalized strain along (a) line 1 (0° boundary) and (b) line 2 (60° boundary)	96
Figure 6.7 Evolution of normalized strain at the 60° boundary for a microstructure with the loading axis parallel to the grain boundary.....	97
Figure 6.8 Magnitude of normalized strain components along the 60° boundary, far-field strain of 5%	98
Figure 6.9 Contour plot of the hydrostatic stress for $a/h = 85$ with a uniaxial tensile load parallel to the grain boundary, far-field strain of 5%.....	99
Figure 6.10 Magnitude of normalized strain across the 60° boundary (line 2) with varying PFZ strengths at far-field strains of 5%	100
Figure 6.11 Magnitude of normalized strain on the 60° boundary (line 2) for a microstructure with $a/h = 85$ and $a/h = 45$	101

Figure 6.12 Magnitude of normalized strain on the 60° boundary (line 2) for microstructures with a/h = 85 and a/h = 45 at (a) 5% strain and (b) 7.5% strain	101
Figure 6.13 Contour plot of the normalized strain for a/h = 85 with a uniaxial tensile load perpendicular to the grain boundary	102
Figure 6.14 Magnitude of normalized strain along (a) line 3 (30° boundary) and (b) line 4 (90° boundary)	103
Figure 6.15 Magnitude of normalized strain components along the 30° boundary	103
Figure 6.16 Contour plot of the hydrostatic stress for a/h = 85 with a uniaxial load perpendicular to the grain boundary	104
Figure 6.17 Variation of yield stress with cooling rate for alloys with and without Cu at T4 temper for (a) recrystallized microstructure and (b) unrecrystallized microstructure	106
Figure 6.18 Variation of yield stress with cooling rate for alloys with and without Cu at T6 temper for (a) recrystallized microstructure and (b) unrecrystallized microstructure	107

List of Symbols

Symbol	Definition
a	Side of the hexagon used in polycrystal plasticity simulation
C	Elastic stiffness tensor
e	Engineering strain
E	Green Lagrange strain
\dot{F}	Deformation gradient rate tensor
h	Precipitate free zone thickness used in the polycrystal plasticity simulation
$h_{\alpha\alpha'}$	Latent hardening parameter
R_m	Tensile strength (N/mm ²)
s	Engineering stress
S	Second Piola Kirchhoff stress
t_f	Final thickness of a cold rolled sample
t_i	Initial thickness of a cold rolled sample
X_c	Fraction transformed
X_v	Vacancy concentration
X_v^c	Critical vacancy concentration
Z	Atomic number
$\dot{\gamma}$	Shear rate
ε	True strain
σ	True stress
τ	Shear stress

List of Abbreviations

Abbreviation	Definition
BSE	Back Scattered Electron
CI	Confidence Index
CP	Crystal Plasticity
CR	Cold Rolled
DAMASK	Düsseldorf Advanced Material Simulation Kit
DC	Direct Chill
DIC	Digital Image Correlation
DSC	Differential Scanning Calorimetry
EBSD	Electron Back Scattered Diffraction
ED	Extrusion Direction
EDS	Energy Dispersive Spectroscopy
EPMA	Electron Probe Micro-Analyzer
FEGSEM	Field Emission Gun Scanning Electron Microscopy
FEM	Finite Element Method
FFT	Fast Fourier Transform
HAADF	High-angle Annular Dark-field
HDC	Horizontal Direct Chill
IPF	Inverse Pole Figure
JMAK	Johnson-Mehl-Avrami-Kolmogorov
NA	Natural Ageing
ND	Normal Direction

OIM	Orientation Imaging Microscopy
PALS	Positron Annihilation Lifetime Spectroscopy
PCG	Peripheral Coarse Grain
PFZ	Precipitate Free Zone
SAD	Selective Area Diffraction
SE	Secondary Electron
TD	Transverse Direction
TEM	Transmission Electron Microscope
UTS	Ultimate Tensile Stress
VDC	Vertical Direct Chill

Acknowledgements

First and foremost, I would like to express my sincere gratitude to my supervisor Dr. Warren J. Poole for his continued support and guidance throughout this project. Many thanks to his encouraging comments that always kept me motivated. I am grateful to Rio Tinto Aluminium and NSERC Canada for providing financial support during my work. Special thanks to Dr. Nick Parson for his valuable feedback during the meetings.

Many thanks to my officemates, Ali, Andrew, Anna, Freddy, Mojtaba, Shuheng, Wendel, Will and Zhijun for all their help and discussions, academic or otherwise. Special thanks to Brian Tran, Sabayasachi Roy and Zhijun Zhang for their invaluable support in the labs. I would also like to thank the staff of the Materials engineering department, Ross, David, Carl and Wonsang, from the machine shop, Marlon and Marie, from the stores, Heli, the SEM technician, and Michelle and Becky, for their continuous help.

I would further like to thank my coffee buddies for all the never-ending discussions at Tim Hortons. I really appreciate all my friends – hiking group, travel group, ‘piano/concert’ buddies, badminton buddies, ‘virtual gaming during pandemic’ buddies, and roommates for helping me create a great work-life balance.

Finally, I would like to sincerely thank my Mom, Dad, Praveen (twin), Uncle, and family for their constant support, love, and encouragement.

Chapter 1: Introduction

Aluminum, an abundantly available light metal, with high strength to weight ratio, has been commercially produced since 1888. A breakthrough in the use of aluminum alloys in the automotive industry occurred in 1961 when Land Rover produced V-8 engine blocks made of aluminum. Since then, the use of aluminum in automotive industries has grown continuously, from 40kg/car in 1976 to 155kg/car in 2015 [1,2], making it the second most used material in vehicles. A recent study estimated that a 10% reduction in vehicle weight can cut the fuel consumption by $\approx 6-8\%$ [3]. Currently, with electric vehicles gaining popularity, the demand for aluminum alloys is on the rise. By 2030, the combined requirement for aluminum body sheets and extrusions, in electric vehicles, is estimated to be 10 million tons [4]. Further, aluminum is also one of the most recyclable metals. An energy equivalent of 21 barrels of oil is saved for every ton of aluminum recycled [5], and on average, over 90% of aluminum scrap is recycled at the end of a vehicle's life (translating to more than half a million tons a year).

In terms of processing, there are two main categories of aluminum alloys: cast alloys and wrought alloys. Wrought alloys include extrusion products which are typically used in battery boxes, frames/sub-frames, rockers, and roof headers of a car. The high strength wrought alloys that are currently being used have a yield strength of ≈ 350 MPa. The target for the next generation alloys is to achieve a yield strength of >400 MPa and a true fracture strain of 0.4-0.7. Among the wrought alloys, AA6xxx extrusion alloys are widely used in the automotive industries, owing to their excellent combination of strength, formability, durability, and corrosion resistance. AA6xxx alloys typically achieve their strength through the formation of a fine distribution of metastable Mg-Si (β'') precipitates.

The current work is part of a larger ongoing project between industry partner Rio Tinto Aluminium and The University of British Columbia, which attempts to develop a model to simulate the complete production process for AA6xxx alloys. For an AA6xxx alloy, the processing route typically involves direct chill (DC) casting, homogenization, re-heating, extrusion, quenching and ageing. The focus of this study is on the effect of cooling conditions, after extrusion, on the mechanical properties of AA6xxx alloys with Cu additions. Generally, as the cooling rate decreases, the strength decreases. The loss of properties at reduced quench rates is referred to as quench sensitivity. Quench sensitivity of an alloy is affected by cooling rates, alloying elements, and the presence of heterogeneous nucleation sites like sub-grain/grain boundaries, dispersoids and dislocations. Apart from lowering the strength of alloys, lower cooling rates also lead to a formation of a wider precipitate free zone (PFZ), which could affect the ductility of the alloy.

In this work, two initial microstructures of an alloy Al, 0.7 wt.% Mg, 1.0 wt.% Si with 0.6 wt.% Cu, were used to study quench sensitivity. The material of interest was cast and extruded by Rio Tinto Aluminium. The as-extruded materials were used to produce two grain structures, predominantly unrecrystallized and recrystallized. These alloys were then solution treated at a temperature high enough to create a supersaturated solid solution, and were cooled at various controlled cooling rates ranging from 4 °C/s to >2000 °C/s. The alloys were subsequently aged, either at room temperature for 7 days (T4) or at 180 °C for 4 hours (T6). After processing the alloys, modified Jominy tests and tensile tests were used to examine the effect of cooling rates on hardness, yield stress, ductility, and fracture behavior. The effect of quench rates on grain

boundary precipitation was qualitatively and semi-quantitatively studied using a field emission gun scanning electron microscope (FEGSEM).

Finally, an open source software crystal plasticity model was used to study plastic deformation behavior of an aluminum alloy with precipitate free zones (PFZ). This model was used to study the effects of various parameters on strain localization within the PFZs.

Chapter 2: Literature Review

2.1 Introduction

In our day to day lives, aluminum is one of the most widely used metals. Its applications include those in the automotive, packaging, and aerospace industries. In terms of processing, there are two types of aluminum alloys; cast alloys and wrought alloys. Among the wrought alloys, the AA6xxx alloys are widely used. This is attributed to their combination of good specific strength, stiffness, ease of joining, and good corrosion resistance.

The major alloying elements of AA6xxx alloys are Mg and Si, which strengthen the alloy, due to the formation of a fine distribution (1-5nm in size) of metastable Mg-Si intermetallic precipitates. Apart from Mg and Si, other alloying elements are Cu, Mn, and Cr. Some elements like Fe, Ni, Cr, Ti can enter the alloy during the extraction of aluminum and remain as impurities. The main objective of adding Cu is to increase the final strength of the alloy as it provides additional precipitation strengthening. Elements such as Mn and Cr can form precipitates known as dispersoids that preserve the fibrous grain structure during extrusion, resulting in an increase in strength.

2.2 Processing of AA6xxx alloys

Figure 2.1 shows an example of a typical extrusion processing route for a AA6xxx alloy [6].

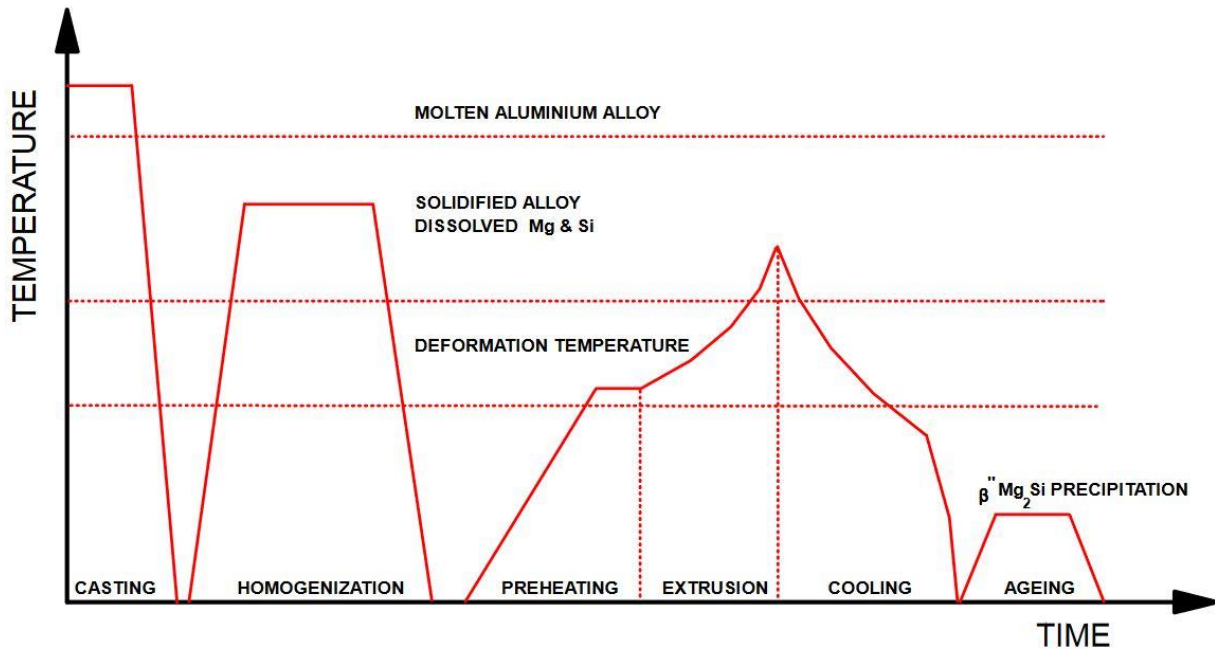


Figure 2.1: Temperature-time history of an aluminum extrusion alloy [6]

The processing of an aluminum extrusion alloy generally involves the following stages.

- Direct Chill (DC) casting
- Homogenization (temperature of 500 – 590 °C and a hold time of 1 – 10 h)
- Reheat and extrusion (typical temperatures of ≈500 °C and a ram speed of 2-30 mm/s)
- Cooling (air cool, spray quench, standing wave tank)
- Ageing (natural ageing or artificial ageing)

2.3 Casting

Generally, AA6xxx alloys are produced by direct chill continuous casting. This process is used to produce ingots for sheet rolling or cylindrical billets for extruded profiles. Casting is done either by vertical DC (VDC) or horizontal DC (HDC) processes. Figure 2.2 shows a schematic

representation of VDC. Molten metal is poured into the mold until a certain desired level is reached, after which the bottom block is gradually lowered. Cooling water circulates in pipes inside the mold and removes heat through the mold walls, which contributes to the primary cooling process [7,8]. The bottom block continues to be lowered and more liquid is poured into the mold to maintain a constant level in the mold. Once the ingot leaves the bottom of the mold, water is directly sprayed on its surface, contributing to the secondary cooling. This process is continued until the desired length of the ingot is achieved.

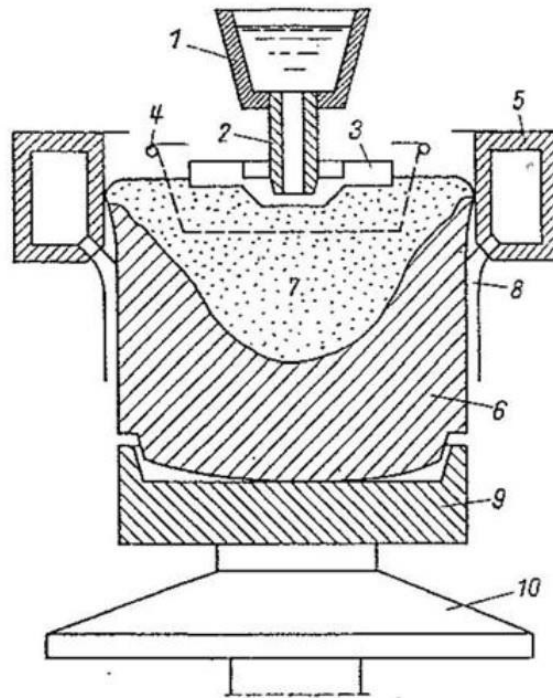


Figure 2.2: Vertical DC casting, 1-feed nozzle, 2-nozzle, 3-float valve, 4-distributor, 5-mold, 6-solidifying ingot, 7-sump, 8-water cooling sprays, 9-stool cap, 10-stool [7]

Figure 2.3 shows an EBSD map of an as-cast microstructure of AA6012 with 0.6 wt.% Cu addition [9]. The grain structure is equiaxed (a TiB_2 inoculant was added to the melt) with an average equivalent area diameter of $95\mu\text{m}$.

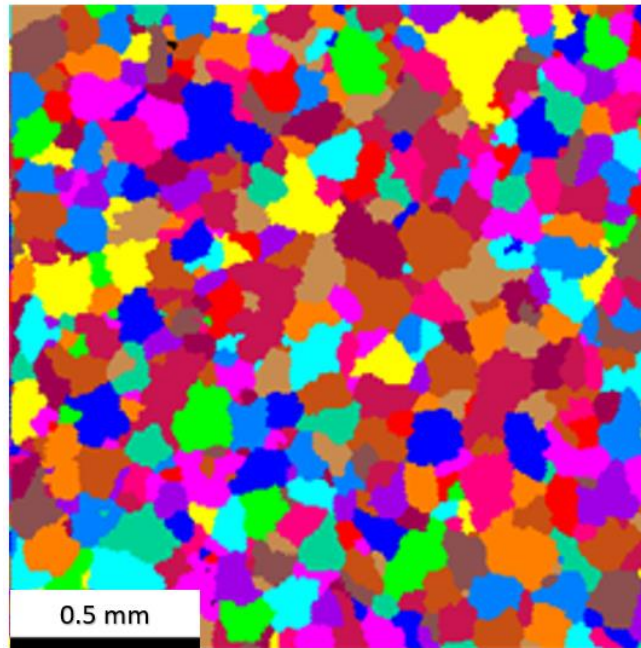


Figure 2.3: As-cast microstructure of alloy AA6002 with 0.6 wt.% Cu [9]

In aluminum alloys of commercial purity, there are several impurities such as Fe, Ni, Cr that remain as they can only be removed at a significant cost. Among these, Fe is one of the most important impurities. During solidification, it forms brittle, hard intermetallic compounds such as $\text{Al}_8\text{Fe}_2\text{Si}$ and β (Al_5FeSi). Figure 2.4 shows an example of an as-cast microstructure for a AA6xxx alloy (Al, 0.9 Mg, 1.6 Si, 0.07 Fe) with different phases identified [10]. Liu et al. [10] used Electron Probe X-ray Microanalysis (EPMA) and X-ray diffraction on phenol extracted particles to identify the intermetallics in the microstructure as Si, π ($\text{Al}_8\text{Si}_6\text{Mg}_3\text{Fe}$), Mg_2Si , and β (Al_5FeSi). The addition of Mn has a significant effect on the as-cast structure with a tendency to promote the α - $\text{Al}(\text{MnFe})\text{Si}$ phase over the β - Al_5FeSi phase, and typically the aluminum

dendrites are supersaturated in Mn after solidification [11]. After casting, aluminum alloys are typically subjected to homogenization heat treatment.

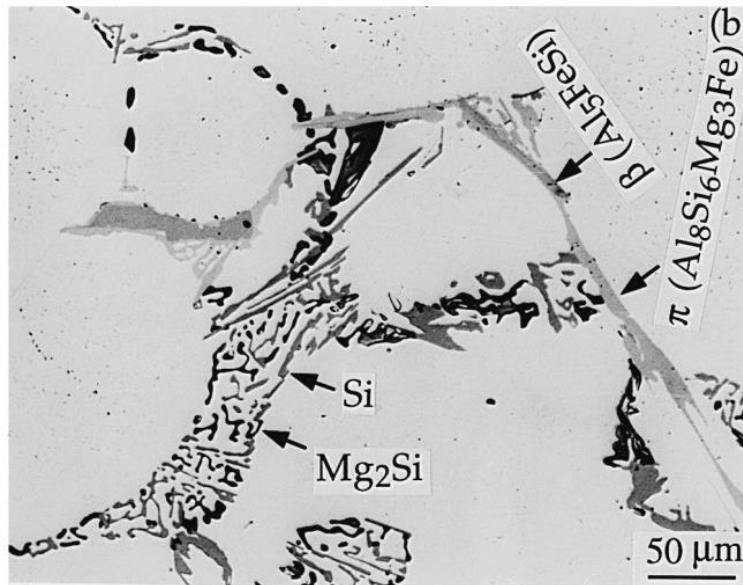


Figure 2.4: An as-cast microstructure with intermetallics [10]

2.4 Homogenization

Non-equilibrium solidification during casting leads to micro-segregation of Mg and Si.

Homogenization is a heat treatment process that is conducted to eliminate micro-segregation and dissolve coarse Mg₂Si particles. An industrial homogenization practice typically consists of a relatively slow heating rate (50-200 °C/h) to avoid large thermal gradients, a hold time of 1-10 h, at 500 – 590 °C, followed by cooling to ambient temperature. In Mn containing alloys, a transformation of plate-like β – Al₅FeSi to rounded α – Al(MnFe)Si can occur depending on the level of Mn and soaking temperature/time [12]. This transformation is important as the plate-like β phase is believed to be responsible for poor surface finish and poor formability of Al extrusions

[11]. Figure 2.5a and 2.5b show an example of an as-cast and as-homogenized (32 hours at 590° C) microstructure with 0.7 wt.% Mg, 0.8 wt.% Si, 0.2 wt. % Mn, 0.3 wt.% Fe [13]. The presence of spheroidized α -particles can be seen in Figure 2.5b.

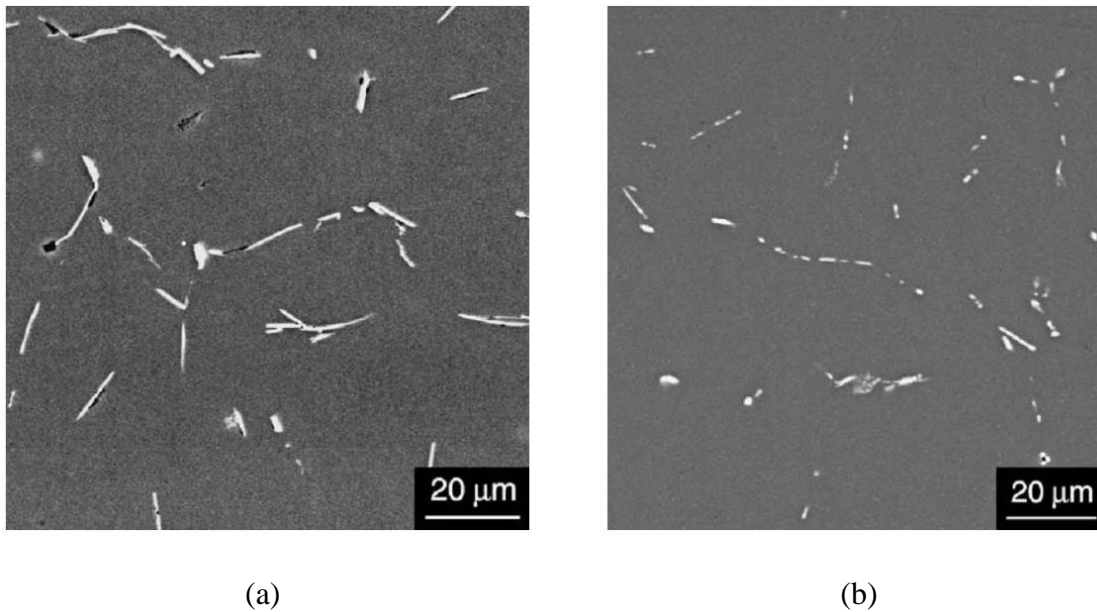


Figure 2.5: Microstructure of (a) as-cast and (b) homogenized at 590°C for 32 hours of an Al 0.83-Si 0.7-Mg 0.18-Mn 0.27-Fe (compositions in wt.%) [13]

During homogenization, secondary particles (dispersoids) can also precipitate within the primary aluminum grains [14]. Dispersoids usually form during the heating stages in alloys containing transition metals such as Cr, Mn and Zr. They are generally introduced in the alloys to retard recrystallization [15,16], which helps in preserving the fibrous structure produced during extrusion. The radius and volume fraction of dispersoids are the significant factors that inhibit recrystallization, during and after extrusion, by Zener drag [17]. The final step during a homogenization heat treatment, after the soaking cycle, is cooling. Slow cooling tends to produce coarse Mg_2Si particles that may not dissolve during preheating before extrusion. The presence of

these particles may cause incipient melting during extrusion [12], and thus, cooling should be controlled to minimize this possibility.

2.5 Reheat and extrusion

After homogenization, Mg and Si can be in the form of precipitates or be retained as solutes in solution. The presence of Mg-Si based particles may increase the flow stress of the billet which in-turn limits the extrusion speed [6]. On the other hand, the presence of coarse Mg₂Si precipitates can result in reduced mechanical properties after the subsequent extrusion and ageing process, since some of the Mg and Si is lost to these coarse particles. Thus, one of the purposes of reheating before extrusion is to dissolve these particles.

This dissolution depends on [18]:

- Size and distribution of precipitates after homogenization
- The temperature and holding time above the solvus temperature

Rapid precipitation of Mg₂Si occurs in the temperature range of 300 °C to 425 °C [18]. This will result in the formation of coarse Mg-Si precipitates unless this temperature range is traversed rapidly. Figure 2.6 shows a plot of preheat rates and the zones of β and β' formation.

AA6xxx alloys are generally extruded using direct extrusion, which involves the process of exerting a hydraulic force in the billet in a container through the aperture of a stationary die [6]. During extrusion, the key parameters that control the deformed state and stored energy are temperature, strain rate, extrusion ratio and alloying elements. In the current work, we used an initial billet temperature of 480 °C, which then increased to 550-560 °C during extrusion, i.e.,

above the solid solution temperature, resulting in the complete dissolution of Mg-Si precipitates after extrusion.

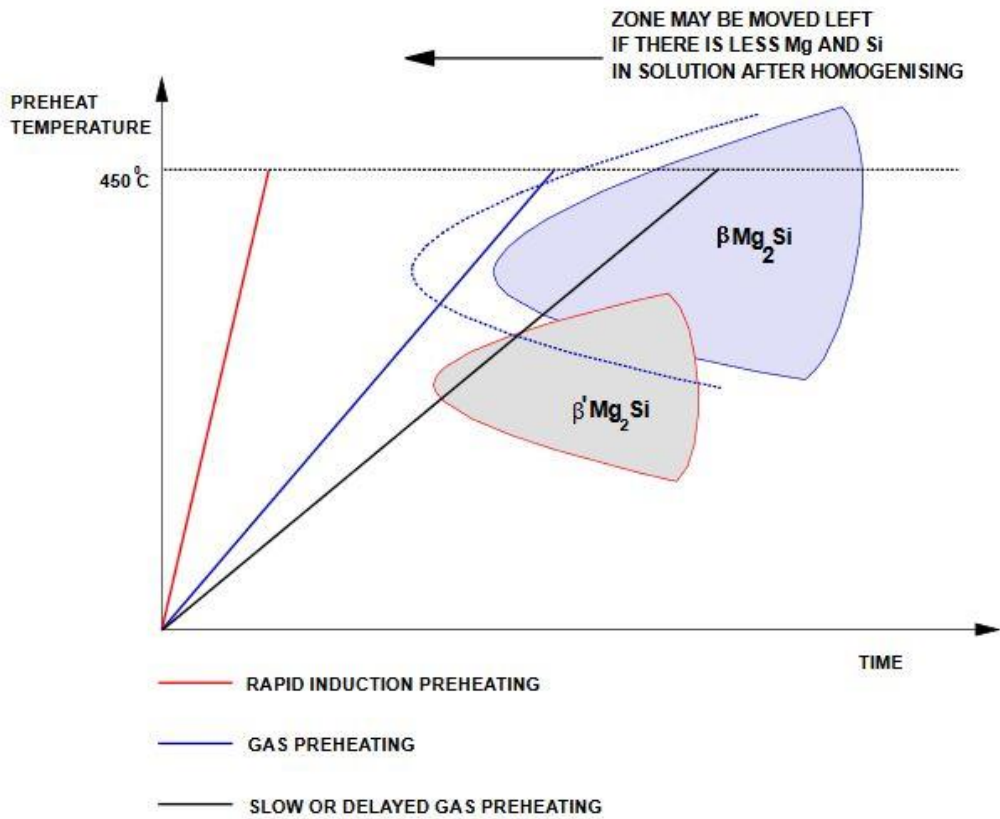


Figure 2.6: Graph of preheat rates and the zones of β and β' formation [6]

2.6 Cooling after extrusion

The objective of cooling after extrusion is to preserve the solid solution formed at high temperatures by rapidly cooling it to a lower temperature (near room temperature). Typically, the cooling rates used in industries are between 5 °C/s and 100 °C/s. To achieve optimal properties, precipitation during quenching must be suppressed. But using high quench rates in industry can

induce distortion in the extrudate, which is not desirable. Hence, there is typically a tradeoff between the final strength and distortion of the product.

2.7 Ageing

Rapid cooling after extrusion results in a non-equilibrium concentration of vacancies (as much as 10^4 times greater than at the equilibrium), that promotes cluster formation and precipitation during the subsequent ageing process. During artificial ageing, the supersaturation of solute atoms decreases, and the strength increases due to the formation of various metastable precipitates. The precipitation sequence of AA6xxx alloys has been extensively investigated [19-22]. The precipitation sequence and the quantity of the precipitates depend on the thermal history, pre-deformation rate, composition of the alloy and quench rate. Nevertheless, the generally accepted precipitation sequence for a Cu free AA6xxx alloy is:



where SSSS is the supersaturated solid solution, and the other metastable and stable precipitates are summarized in Table 2.1 [19]. The addition of copper significantly changes the precipitation sequence [23], i.e.,



The shapes and stoichiometry of important precipitates with the addition of Cu are shown in Table 2.2.

Table 2.1: Precipitate phases in a Al-Mg-Si system [19]

Phase	Stoichiometry	Shape	Crystal structure (Space group)	Orientation relationships (OR) [24]
G.P. Zone	AlMg_4Si_6	Needle		
β''	$\text{Mg}_5\text{Si}_6/$ $\text{Mg}_5\text{Al}_2\text{Si}_4$ [25]	Needle	Monoclinic (C2/m)	$(001)_{\beta''}/(001)_{\text{Al}}$ $[100]_{\beta''}/[310]_{\text{Al}}$
β'	Mg_9Si_5 [26]	Rod [37]	Hexagonal (P6 ₃ /M)	$[001]_{\beta'}/[001]_{\text{Al}}$ $[2\bar{1}\bar{1}0]_{\beta'}/[\bar{3}10]_{\text{Al}}$ + multiple ORs
U1	MgAl_2Si_2	Needle	Trigonal (P3ml)	$[100]_{\text{U1}}/[001]_{\text{Al}}$ $[001]_{\text{U1}}/[310]_{\text{Al}}$ $[120]_{\text{U1}}/[130]_{\text{Al}}$
U2	MgAlSi	Needle	Orthorhombic (Pnma)	$(010)_{\text{U2}}/(001)_{\text{Al}}$ $[100]_{\text{U2}}/[310]_{\text{Al}}$ $[001]_{\text{U2}}/[130]_{\text{Al}}$
B'	$\text{Mg/Si} \sim 1$	Lath	Hexagonal (P6)	
β	Mg_2Si	Plate	Cubic (Fm3m)	

Table 2.2: Precipitate phases in a Al-Mg-Si-Cu system [23]

Phase	Stoichiometry	Shape	Crystal structure (Space group)	Orientation relationship (OR) [24]
QP	Unknown	Needle	Hexagonal	
QC	Cu/Si ~ 0.36 Mg/Si ~ 1.36	Needle	Hexagonal	
C	Mg ₄ AlSi _{3+x} Cu _{1-x} , x, x~0.3	Plate	Monoclinic	(001) _C //(001) _{Al} [100] _C //[100] _{Al}
Q'	Al ₃ Cu ₂ Mg ₉ Si ₇ / Al ₄ Cu ₂ Mg ₈ Si ₇	Lath	Hexagonal (P6)	[0001] _{Q'} //[001] _{Al} [1 $\bar{2}$ 10] _{Q1} //[130] _{Al} + multiple ORs
Q	Al ₃ Cu ₂ Mg ₉ Si ₇ / Al ₄ Cu ₂ Mg ₈ Si ₇ / Al ₅ Cu ₂ Mg ₈ Si ₆ [25]	Lath	Hexagonal (P6)	[0001] _Q //[001] _{Al} [1 $\bar{1}$ 20] _Q //[510] _{Al} + six different ORs

Strengthening by ageing can be achieved either at room temperature (natural ageing) or at higher temperatures (artificial ageing).

2.7.1 Natural ageing

Strengthening by ageing at room temperature (i.e., natural ageing) is achieved by cluster formation [27-33]. Vacancies play an important role in the formation of clusters during natural ageing (NA). In AA6xxx alloys, the increase in strength during natural ageing is attributed to the increase in the number density of Mg-Si clusters which act as obstacles to mobile dislocations [31]. It has been found that the hardness initially increases at a higher rate for the first few hours at room temperature and slows down with increasing time.

Song et. al. [32] studied the effect of Cu additions on the formation of clusters. They found that with the addition of Cu, in addition to Mg-Si clusters, ternary clusters Mg-Si-Cu, and binary clusters Cu-Mg, Cu-Si and Cu-Cu were formed. They also found that Cu was incorporated in the cluster after the formation of Mg-Si cluster. With increasing Cu content, the formation of nanoclusters was found to be suppressed in the initial stages of NA. This was attributed to the formation of Cu-vacancy pairs during quenching, which traps the vacancies making them unavailable to form clusters. However, Kim et. al. [34] found that the presence of Cu accelerated the cluster formation in the later stages of natural ageing. They speculated that Cu could have strong attractive interactions with Mg that are then incorporated into the Si-rich clusters. In summary, the role of Cu on cluster formation is complex and not clearly understood at this time.

2.7.2 Artificial ageing

AA6xxx alloys typically obtain their strength during artificial ageing due to the formation of β'' in Cu free alloys and, β'' and Q/Q' phase in alloys with Cu [35]. More details on the recent studies on precipitation sequences in a Al-Mg-Si-Cu alloy can be found in references [23,36-38].

In many heat-treated alloys that undergo artificial ageing, natural ageing occurs prior to artificial ageing. Depending on the duration of natural ageing and Mg/Si ratio, it can have a negative [39-41] or a positive effect [39,41,42] on the subsequent artificial ageing. Liu et. al. [27] showed that the temperature of the subsequent artificial ageing also plays a role in deciding if the prior natural ageing has a positive or a negative effect.

2.8 Quench sensitivity

Quench sensitivity is used to analyze the loss of properties for different quench rates after extrusion. The loss of strength at lower quench rates is a particular challenge for higher strength aluminum alloys. A detailed review of quench sensitivity was recently conducted by Milkereit et. al. [43]. The reduction in strength and hardness occurs due to the loss of solute atoms which precipitate as coarse precipitates on heterogeneous nucleation sites (typically grain boundaries [44], dispersoids [17,39,45] or dislocations [45]), during slow cooling [46].

A good example of quench sensitivity is the study done by Strobel et. al. [47] as shown in Figure 2.7. The hardness of four AA6xxx alloys (AA6060, AA6005A, AA6061 and AA6082) was plotted as a function of cooling rate. Note, the alloys were aged for 24 hours at room temperature and 8 hours at 190 °C. From Figure 2.7, it was observed that low strength alloy, AA6060 was almost independent of the quench rate, while high strength alloy, AA6082 was strongly dependent on the quench rates.

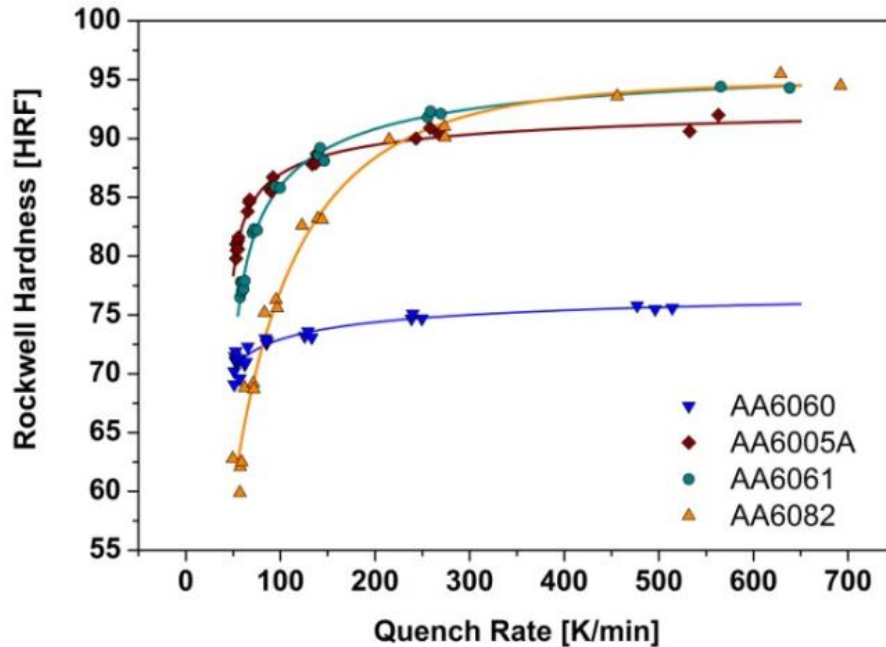


Figure 2.7: Variation of hardness with quench rates for four AA6xxx alloys, with AA6060 (Al 0.43-Si 0.45-Mg 0.18-Fe), AA6005A (Al 0.73-Si 0.53-Mg 0.12-Cu 0.18-Fe 0.1-Mn), AA6061 (Al 0.62-Si 0.87-Mg 0.25-Cu 0.21-Fe 0.13-Mn 0.1-Cr) and AA6082 (Al 1.05-Si 0.75-Mg 0.05-Cu 0.15-Fe 0.6-Mn) (Note: compositions are in wt.%)

[47]

2.8.1 Factors affecting quench sensitivity

2.8.1.1 Cooling rate

As shown in the previous section, the cooling rate has different effects for different alloys. It is therefore important to find a critical cooling rate at which precipitation is suppressed. Milkereit et. al. [48,49] used differential scanning calorimetry (DSC) to identify the critical cooling rates for certain alloys. An example of the DSC study conducted [48] is shown in Figure 2.8 for an aluminum wrought alloy (AA6005A, 0.7 wt.% Si, 0.6 wt.% Mg).

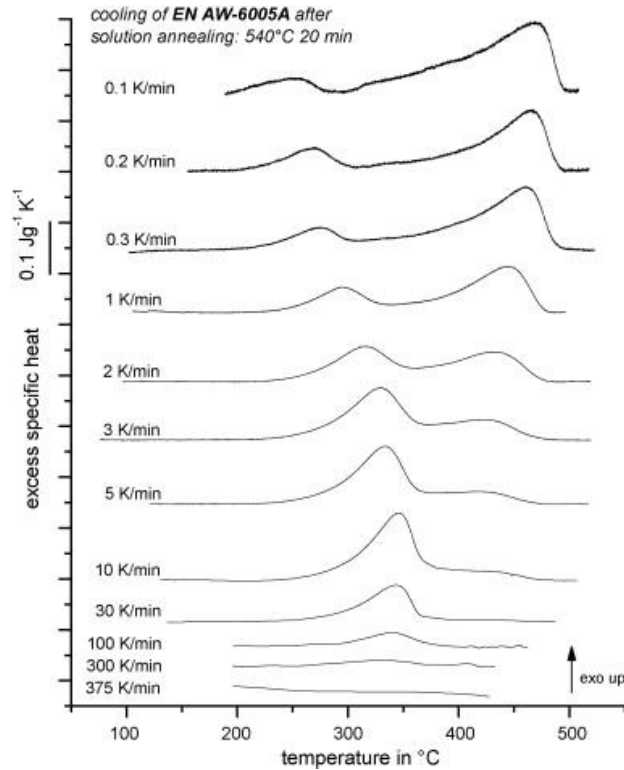


Figure 2.8: DSC curves for cooling rates between 0.1 K/min to 375 K/min for the alloy EN AW-6005A [48]

From this study, the critical cooling rate for the alloy 6005A was identified to be 375 K/min. From Figure 2.8, for a cooling rate of 0.1 K/min, two peaks were identified at ~470 °C and ~250 °C. The difference in the peak temperature was ~220 °C. This difference was observed to decrease with increasing cooling rate. At cooling rates ≥ 375 K/min, the precipitation was completely suppressed. In summary, during cooling, an alloy can achieve its maximum strength only if the cooling rate is greater than the critical cooling rate.

During slow cooling, β/β' or Q/Q' form on heterogeneous nucleation sites such as grain boundaries or dispersoids depending on the Cu content. An example of grain boundary precipitation [50,51] for a Cu containing AA6xxx alloy is shown in Figure 2.9 [52]. These grain

boundary particles were identified to be the Q or Q' phase precipitates. An example of precipitation of the β/β' phase on dispersoids is shown in Figure 2.10 [35].

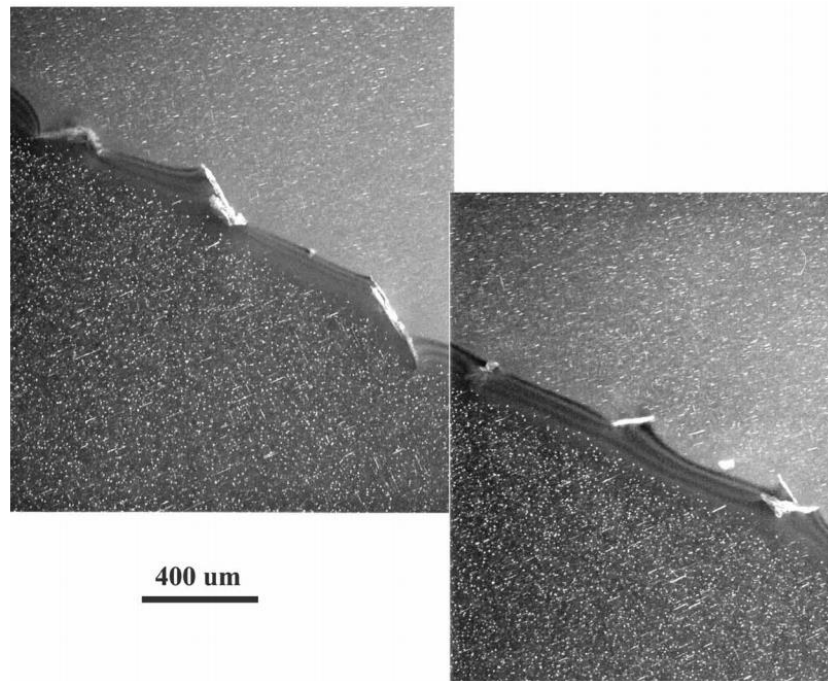


Figure 2.9: Grain boundary precipitation of Q phase in a AA6xxx alloy with Cu [52]

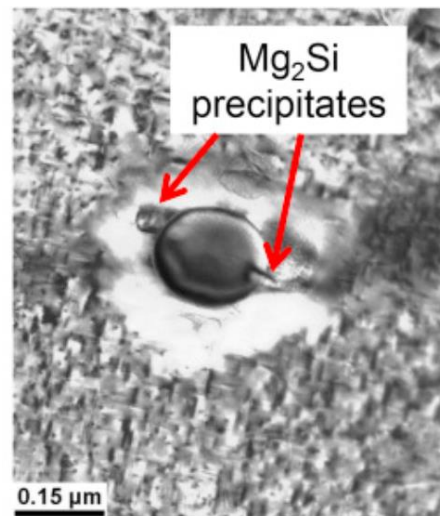


Figure 2.10: Precipitation of β phase on a dispersoid particle in a AA6xxx alloy [35]

2.8.1.1.1 Modelling of precipitation during cooling

Bratland et. al. [53] developed a model based on the classical theory of diffusion-controlled growth. The shape and position of the C curve were determined from the nucleation and growth rate, the density and distribution of nucleation sites, and the fraction transformed. The fraction transformed was described using a Johnson-Mehl-Avrami-Kolmogorov (JMAK) equation.

Figure 2.11 shows an example of an isothermal transformation diagram calculated from the model, for four different AA6xxx alloys.

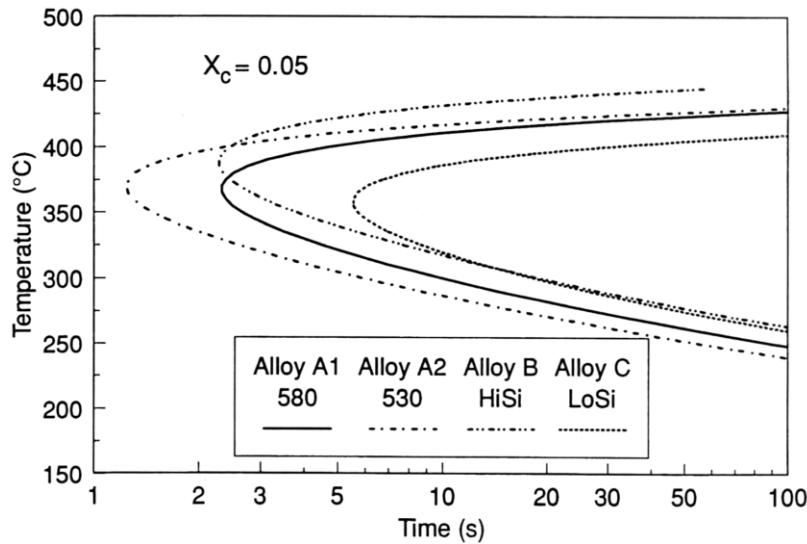


Figure 2.11: Computed isothermal transformation diagrams for four AA6xxx alloys, A1 and A2 (Al 0.98-Si 0.64-Mg 0.52-Mn 0.19-Fe), B (Al 1.32-Si 0.62-Mg 0.5-Mn 0.24-Fe), C (Al 0.69-Si 0.63-Mg 0.49-Mn 0.21-Fe) [53]

Figure 2.11 shows that significant precipitation occurs in the temperature range of 300 - 400 °C, regardless of the alloying content. Among the alloys, A2 was found to be the most quench sensitive attributed to a lower homogenization temperature that resulted in a higher density of dispersoids. Alloy C is the least quench sensitive due to its lower Si content and relatively higher homogenization temperature.

2.8.1.1.2 Formation of precipitate free zones at grain boundaries

It is common to observe precipitate free zones (PFZ) around the grain boundaries, an example of which can be seen in Figure 2.9. The formation of PFZs at grain boundaries has historically been attributed to one of the following: [54,55]

1. Grain boundaries act as a sink for vacancies. Since the concentration of vacancies adjacent to the grain boundaries is lower, the nucleation of precipitates in those regions, which involves vacancies, is suppressed. The effect of quench rates and critical vacancy concentration on the width of PFZs is shown schematically in Figure 2.12 [55]. This mechanism would suggest that no precipitates would form on the grain boundary and the Mg and Si solute levels in the PFZ would be unchanged

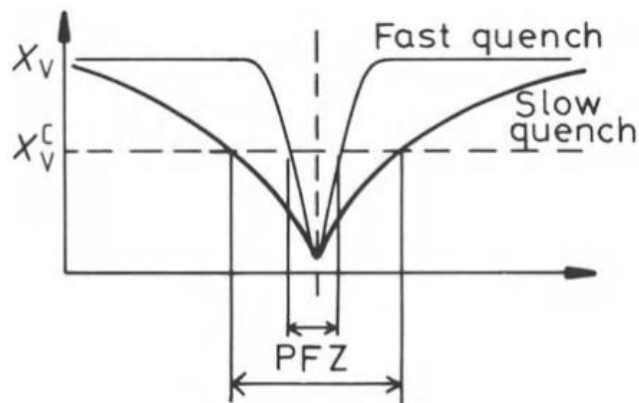


Figure 2.12: Dependence of PFZ width on the critical vacancy concentration X_V^c and quench rate [55]

2. Precipitation occurs at grain boundaries due to solutes being transported to the boundaries (possibly, with the assistance of non-equilibrium vacancies). This suggests a formation of a solute depleted zone adjacent to the grain boundary

In terms on the role of Cu additions, there is relatively little literature. However, Saito et. al. [21] showed that the addition of Cu leads to a narrower PFZ. In this study, samples were slowly cooled until 200 °C, and then were water quenched. After 4h of natural ageing and 2h of artificial ageing at 185 °C, the PFZ widths were measured to be $\approx 600\text{nm}$ in the Cu free alloys and $\approx 400\text{nm}$ in Cu containing alloys.

Modeling of precipitate free zones [56]

Using mean-field and boundary integral models, Yang et. al. developed a model to simulate the formation of PFZs [56]. The system included 10,000 particles initially with two parallel grain boundaries located at the ends as shown in Figure 2.13a. With increasing normalized times (τ), an increase in the width of the formed PFZs was observed (Figure 2.13b-d).

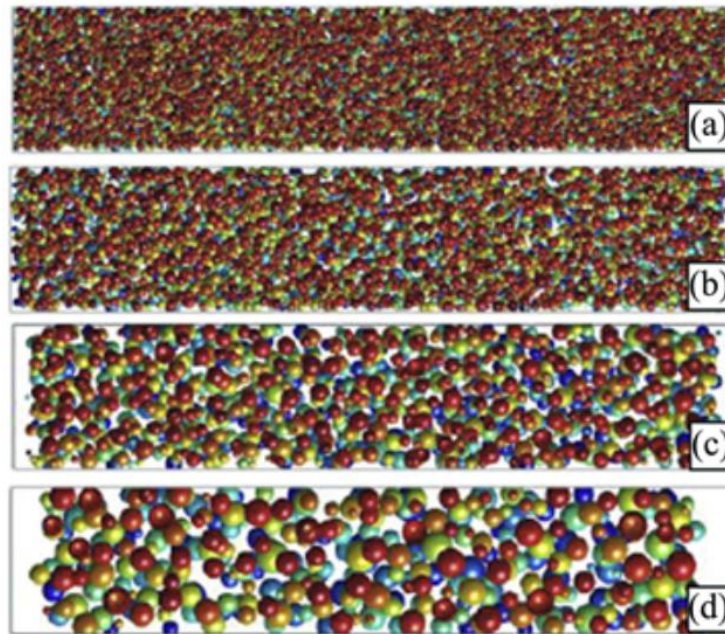


Figure 2.13: Simulation of the distribution and coarsening of particles, and the formation of precipitate free zones adjacent to the grain boundaries, at a normalized time of (a) 1 (b) 5000 (c) 8000 and (d) 9000 [56]

Along with the increase in the width of the PFZs, the number of particles in the system decreased from 10,000 at $\tau = 1$ to 1256 at $\tau = 9000$, indicating particle coarsening. This model predicted that the increase in the width of the PFZs is proportional to the square root of simulation time.

2.8.1.2 Effect of alloying elements

Influence of Mg and Si

The maximum attainable strength of a AA6xxx alloy depends on the level of Mg and Si which form β'' precipitates. The quench sensitivity of these alloys increases with increasing Mg and Si content [18]. A minimum amount of Mg and Si is required to achieve significant precipitation hardening in the final product; however, in extrusion alloys, this may need to be balanced by the effect of solute on the high temperature flow stress (which determines the extrusion force). For example, magnesium additions have been found to increase the extrusion force by at least twice as much as silicon [18].

Effects of Cu

The maximum solubility of Mg and Si in aluminum limits the strength of AA6xxx alloys. Thus, there has been a considerable interest to add Cu to Al-Mg-Si alloys, to increase strength without increasing the quench sensitivity. Addition of Cu increases the number density of precipitates that are formed during ageing, which increases the overall strength of the alloy [57]. In Cu containing AA6xxx alloys, Strobel [58] showed that after slow cooling, the Cu content (relative to the content of Mg and Si) was higher in solid solution than in non-hardening precipitates. This suggested that less Cu was lost during slow cooling, potentially improving the age hardening response, decreasing the quench sensitivity.

2.8.1.3 Effects of natural ageing after extrusion

During natural ageing, both vacancy annihilation and cluster formation occur simultaneously.

Using positron annihilation lifetime spectroscopy (PALS), Strobel [58] and Yang et. al. [59]

showed the effect of quench rates on the kinetics of natural ageing:

- a) During the initial stages of natural ageing (<100 min), a faster increase in hardness was observed in the water quenched/oil quenched samples when compared with the air cooled samples
- b) In the later stages of natural ageing, the hardening rate was found to be independent of the cooling rates

2.8.1.4 Effects of dispersoids

Dispersoids increase the quench sensitivity as non-hardening precipitates nucleate on them during cooling. With increasing Cr and Mn content, the density of dispersoids increase, which further increases the quench sensitivity. Figure 2.14 shows the influence of Cr, Mn and Zr on quench sensitivity [18] (Mn level was raised to take into account its lower efficiency in inhibiting recrystallization). The advantage of Cr addition can be observed from Figure 2.14. Mn was found to increase the quench sensitivity significantly, even at the same alloying levels as Cr.

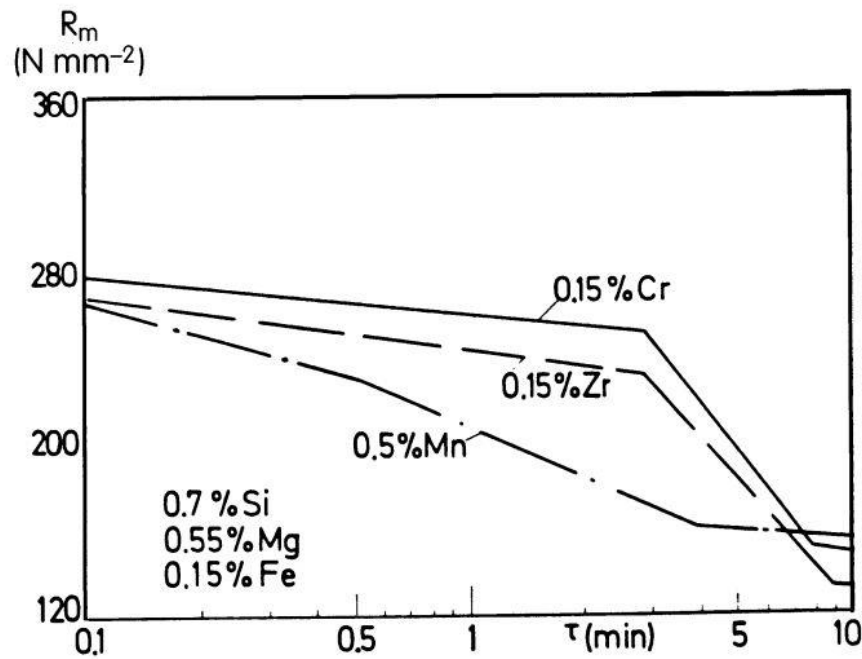


Figure 2.14: Tensile strength as a function of median cooling time (τ), showing the effect of Mn, Cr and Zr on quench sensitivity [18]

2.8.1.5 Role of deformed structure

Generally, unrecrystallized alloys have elongated grains (with sub-grains) and exhibit a crystallographic texture that is related to the deformation path during extrusion. The presence of sub-grains and highly elongated high angle grain boundaries in the unrecrystallized microstructure potentially can play a role in the nucleation and growth of precipitates, thereby increasing quench sensitivity [60]. However, there is little information in the literature on the role of deformed structure and is one of the motivations for the current study.

2.9 Fracture

AA6xxx alloys undergo ductile fracture, which is characterized by extensive plastic deformation prior to failure [61]. Ductile fracture occurs due to the nucleation, growth, and coalescence of micro-voids. When void coalescence occurs shortly after void nucleation with a limited amount of growth, the failure is said to be ‘nucleation controlled’. On the other hand, if coalescence occurs after significant void growth, the fracture mechanism is said to be ‘void controlled’ [62]. These micro-voids either pre-exist or nucleate at the sites of inclusions or second-phase particles [63]. Among these second-phase particles, equiaxed particles generally suffer interfacial decohesion (separation of the particle-matrix interface) after a certain plastic strain is reached, while particles with a high aspect ratio fail by internal fracture (breakage of the second phase particle) [64]. For the nucleation of voids, there exists a critical nucleation strain below which there is [64];

- (i) Insufficient stress to break the interface or
- (ii) Insufficient elastic strain energy to create internal interfaces

As the particle size decreases, void nucleation becomes increasingly difficult [65], i.e., as the particle size decreases, the nucleation strain increases. Once nucleated, with continuing plastic flow, the voids undergo shape change and volumetric growth [61]. Rice and Tracey [66] developed a void growth model, in which volume change was considered to be a function of hydrostatic stress only, while shape change was dictated by the deviatoric component. The void growth was also found to be dependent on the initial orientation of the crystal [67]. The voids continue to grow until the lengths of the two adjacent voids equals the distance between them [68], i.e., void spacing acts as the dominant parameter controlling the transition from growth to

coalescence. After the coalescence of two voids (forming a larger void), damage may then proceed by [62]:

- I. Further coalescence of voids
- II. Coalescence of larger voids with isolated voids or
- III. Coalescence of two or more larger voids

With further increasing plastic flow, the voids link over a macroscopic scale leading to final failure. Another possible mechanism of grain boundary failure is the debonding of grain boundaries under stress, due to weak cohesion of grains. An example of grain boundary decohesion was shown by Davidkov et. al. for a 6016 alloy in the T4 temper [69].

In many AA6xxx alloys, a precipitate free zone (PFZ) forms around the grain boundaries. The absence of strengthening precipitates in these zones suggests that they may have a lower yield strength than the grain interior. However, the elastic grain interior then imposes a constraint on the PFZ [70]. This potentially leads to a situation where nucleation, growth and coalescence of voids occur predominantly on the boundaries, resulting in an intergranular ductile failure [71]. However, under certain conditions, void nucleation may proceed more quickly in the grain interior, resulting in a transgranular mode of fracture. As such, there can be considered to be a competition between the transgranular and intergranular ductile fractures as shown schematically in Figure 2.15 [63].

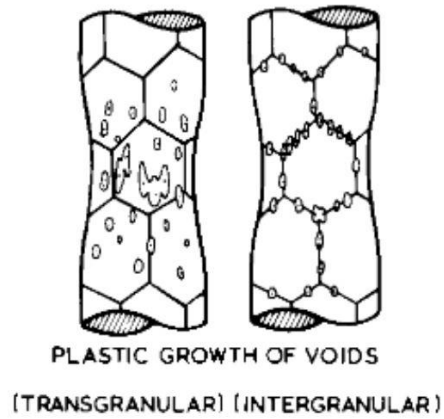


Figure 2.15: Transgranular and intergranular type of fracture under tensile stress [63]

Adding to the complexity of this competition is (i) the distribution of slip within the grain and how this interacts with the grain boundary [72], and (ii) the thickness of the PFZ, and the presence of grain boundary precipitates as shown schematically in Figure 2.16.

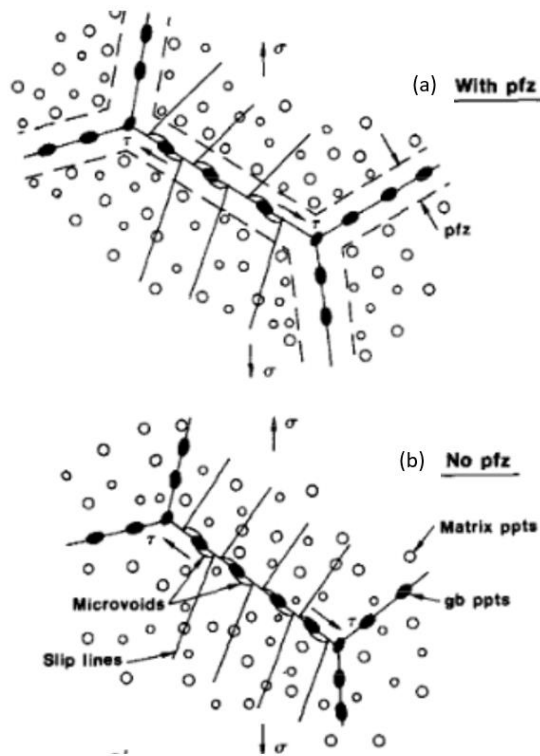


Figure 2.16: Schematic of the deformation processes (a) with PFZ and (b) without PFZ [73]

From 2.16a it can be observed that in the presence of PFZs, the strain localizes on the boundaries, strongly promoting the formation of micro-voids adjacent to the grain boundary precipitates. On the other hand, in the absence of PFZs, voids would still nucleate at the particle, but the void nucleation strain would be much higher [73].

Using finite element simulations, Pardo et. al. [71] suggested that the following conditions would favor intergranular fracture for a grain boundary oriented perpendicular to the applied stress:

- i. The state of triaxiality in the PFZ
- ii. A small value of void spacing/void diameter
- iii. A high value of PFZ thickness/void spacing

Intergranular mode of fracture is almost always associated with a lower ductility than the transgranular mode. Poole et. al. [35] showed the effect of cooling rates and level of Mn on ductility. For both higher and lower cooling conditions, alloys with higher Mn was observed to have twice the amount of true strain to fracture as the alloys with lower Mn. Also, a decrease in true fracture strain was observed with decreasing cooling rates, which was attributed to the increase in the fraction of intergranular fracture with decreasing quench rates. Morgeneyer et. al. [89] showed the effect of quench rates on toughness in an Al-Mg-Si-Cu sheet alloy. Thomesen et. al. [74] showed the decrease in failure strain with increasing yield stress for AA6xxx alloys. Castany et. al. [75] showed that in Si-rich alloys, Si particles with a high aspect ratio form on the grain boundary. These particles were found to be detrimental to the ductility of the alloy as they promote intergranular fracture.

2.9.1 Localization at the PFZ

Drucker [70] developed a 2D plane strain model of hexagonal particles separated by a layer of uniform thickness. A synopsis of Drucker's model was described by Bao et. al. [76], and the basic feature of the model is shown in Figure 2.17. For a low h/H ratio, the hexagon and the layer can be considered to represent grains and precipitate free zones, respectively. It was shown that under tension, the high magnitude of stress that develops in the boundaries was inversely proportional to the layer thickness. This simple model shows how constraint and the development of a triaxial stress state in the PFZ can make the predictions of local fracture behavior challenging.

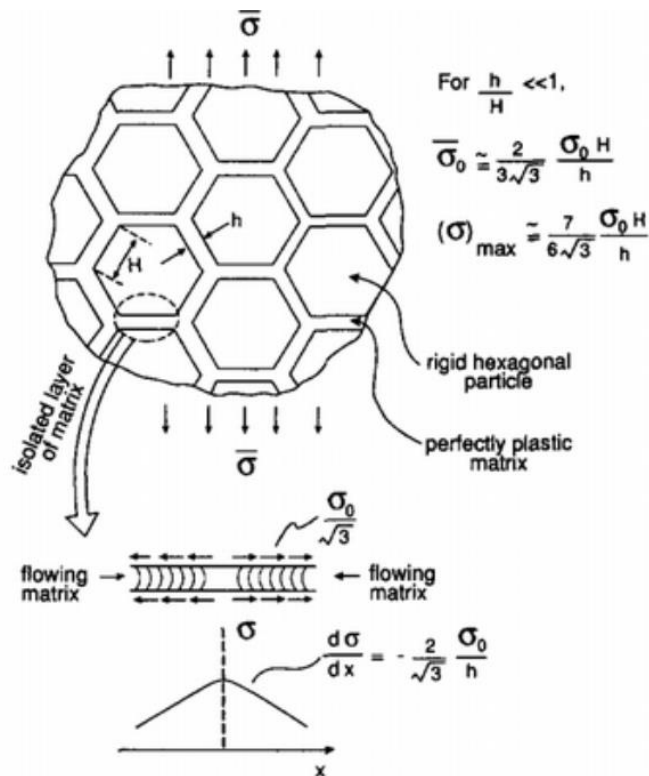


Figure 2.17: Summary of Drucker's 2D model [70] of uniform hexagonal particles separated by a perfectly-plastic matrix [76]

Apart from complex stress state, strain localization in the PFZ may also play an important role in determining the mode of fracture. Using Digital Image Correlation (DIC), Mansouri et. al. [77] quantified the effect of quench rate on strain localization in the grain boundaries. Figure 2.18 shows the normalized strain (i.e., the ratio of local von Mises Strain to the far field strain) across a grain boundary for a water quenched and a slow cooled (3 °C/s) samples.

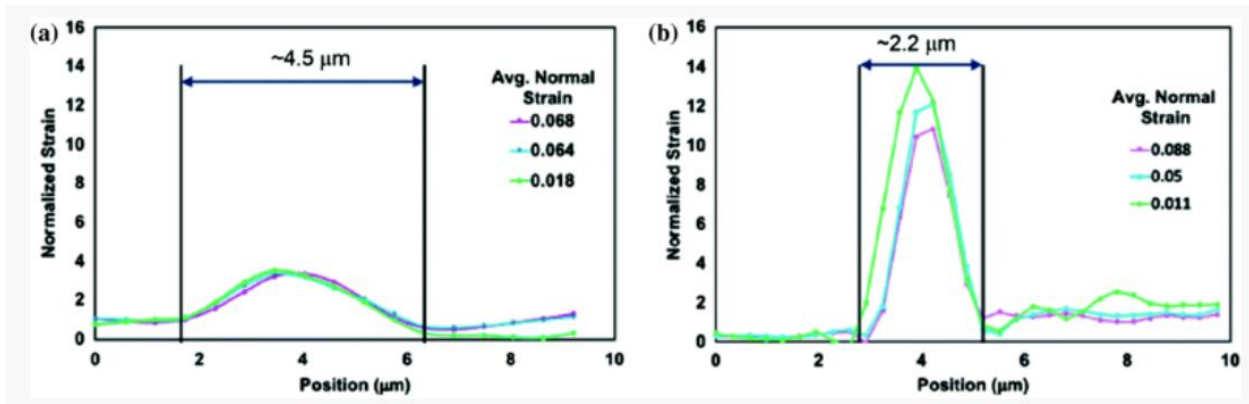


Figure 2.18: Strain localization on a grain boundary for (a) water quenched condition and (b) slow cooled (3 °C/s) sample [77]

The grain boundary in the water quenched sample was observed to experience a strain ≈ 4 times that of the far-field strain. In the slow cooled sample, however, the strain concentration at the boundaries was ≈ 10 -14 times. Further, using TEM and finite element based crystal plasticity simulations, Khadyko et. al. [78] showed that the large plastic strains in the PFZs can lead to a large rotation of the lattice within the PFZs. In some PFZs, the rotation was found to be high enough for the PFZ to form a sub-grain like structure. These simulations also showed that the highest magnitude of hydrostatic stress was accumulated near the triple junctions.

Frodal et. al. [79] showed the effect of presence of PFZs in unrecrystallized materials. In general, PFZs form not only adjacent to sub-grains/grains, but also around dispersoids. In some cases, they observed an overlap between the PFZs around sub-grains and dispersoids which produced an entire sub-grain free of precipitates.

2.10 Crystal plasticity simulations

Crystal plasticity (CP) method is based on the behavior of single crystals. A polycrystalline material can be modeled either in a full-field simulation (provides spatial distribution of field values) or in a homogenized way (used in macroscopic loading situations). The most common methods used in the field of CP are the Finite Element Method and the Fast Fourier Transforms (FFT) based spectral method. Khadhyko et. al. [78] used FEM to study the deformation behavior of a crystalline composite system. However, Eisenlohr et. al. [80] showed that the spectral methods are computationally much quicker than the conventional FEM. Spectral methods were also shown to reach spatial resolutions that are otherwise quite expensive, in terms of memory requirements, to reach with FEM. On the other hand, unlike conventional FEM, standard FFT solvers can only be used to solve problems with periodic boundary conditions. Düsseldorf Advanced Material Simulation Kit (DAMASK) [81] is a flexible open source crystal plasticity software developed in Max-Planck Institut für Eisenforschung (MPIE). DAMASK has both FEM and spectral methods based solvers. The field equations in the spectral method using FFTs are solved using fully implicit time stepping. The elastic behavior of a material is modeled in DAMASK using a generalized Hooke's law. For the plastic behavior, it provides various modules including isotropic plasticity, phenomenological crystal plasticity and dislocation density based crystal plasticity [81,82].

Chapter 3: Scopes and objectives

Quenching after extrusion plays an important role in determining the final performance of AA6xxx alloys. Lower cooling rates result in decreased strengths, while higher quench rates may lead to distortion of the extrudate. It is therefore important to quantify the effect of cooling rate so that the processing conditions can be tailored to the specific application.

3.1 Scope

Automotive grade AA6xxx alloy, Al – 0.7 wt.% Mg – 0.9 wt.% Si with additions of 0.6 wt.% Cu was cast, homogenized, and extruded by Rio Tinto Aluminium, Canada. Two initial grain structures were produced: unrecrystallized and recrystallized, using a solution heat treatment of 5 min at 550 °C, and cold rolling. These alloys were then cooled at 4-5, 10, 25, 80 and >2000 °C/s, followed by ageing, either at room temperature for a week (natural ageing), or at 180 °C for 4 hours (artificial ageing). The mechanical properties were then characterized using the modified Jominy tests and tensile tests.

3.2 Objectives

The main objectives of this work are:

- (i) To produce, and characterize the two initial microstructures, predominantly unrecrystallized and recrystallized alloys, using electron back-scattered diffraction (EBSD).
- (ii) To study the effect of quench rates on hardness using the modified Jominy test.
- (iii) To qualitatively and semi-quantitatively study grain boundary precipitation during cooling, using FEGSEM and TEM.

- (iv) To characterize mechanical properties including the yield stress, ultimate tensile stress, and ductility after different cooling rates.
- (v) To simulate the local stress and strain response of an aluminum alloy with precipitate free zones (PFZs) using a polycrystal plasticity model.
- (vi) To compare the results with recent work by Sarmady [60] on a Cu free version of the alloy.

Chapter 4: Methodology

4.1 Introduction

The experimental and simulation methods used will be described in this chapter. Section 4.2 introduces the initial material provided for the study. The experimental methods used will be described in Sections 4.3 – 4.9 and the details of simulations will be discussed in Section 4.10.

4.2 Initial Material

The initial extruded material was provided by Rio Tinto Aluminium, Quebec. The samples were prepared from cylindrical billets (101mm in diameter) that were homogenized and then extruded. Homogenization heat treatment consisted of heating the billets to 550 °C. Up until 500 °C, a heating rate of 250 °C/h was used, and then a heating rate of 50 °C/h was used from 500-550 °C. The billets were then held at 550 °C for 2 h before the subsequent water quench. The billets were extruded with an extrusion ratio of 70 with an initial billet temperature of 500 °C and a ram speed of 5 mm/s. Figure 4.1 shows a schematic of the extrusion press, the feeder plate and the die used in the extrusion [83]. The dimension of the extruded sample was 42mm × 3.1mm. The chemical composition of this alloy is shown in Table 4.1.

Table 4.1: Chemical composition of the initial alloy in wt.% (as measured by optical emission spectroscopy)

Alloy	Si	Mg	Cu	Mn	Fe	Cr
A612	1.02	0.69	0.59	0.51	0.20	0.15

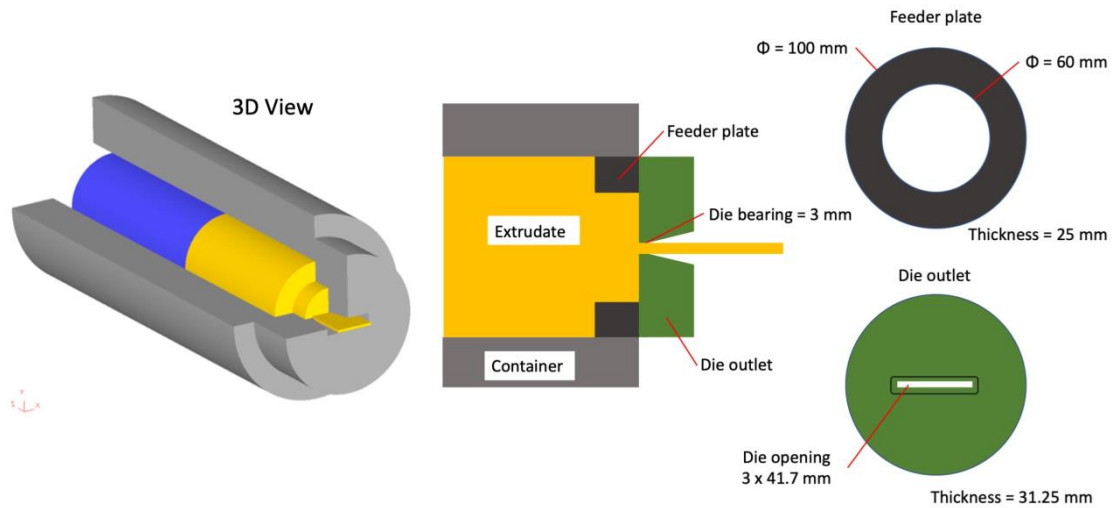


Figure 4.1: Schematic of the extrusion press, the feeder plate and the die used in the extrusion [83]

Figure 4.2a and 4.2b show the size distribution of the constituent particles in the as-cast condition and after homogenization at 550 °C for 2 hours, respectively.

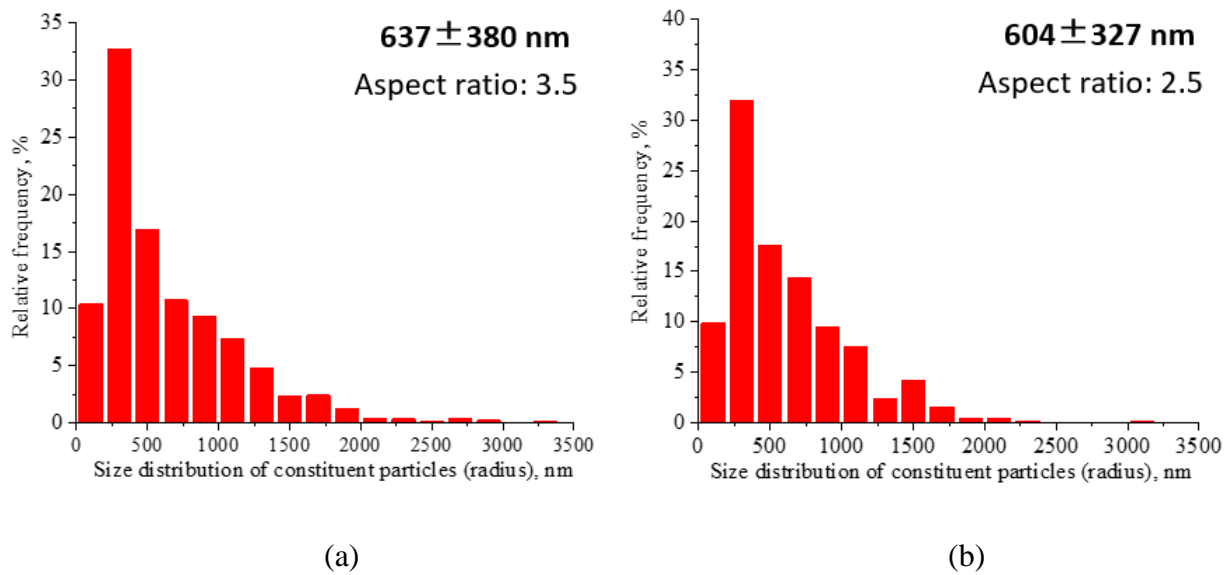


Figure 4.2: Size distribution of the constituent particles present in the (a) as-cast condition and (b) as homogenized at 550 °C for 2 hours

The average size of the constituent particle does not change significantly after homogenization.

Figure 4.3 shows the size distribution of the dispersoids present in alloy A612.

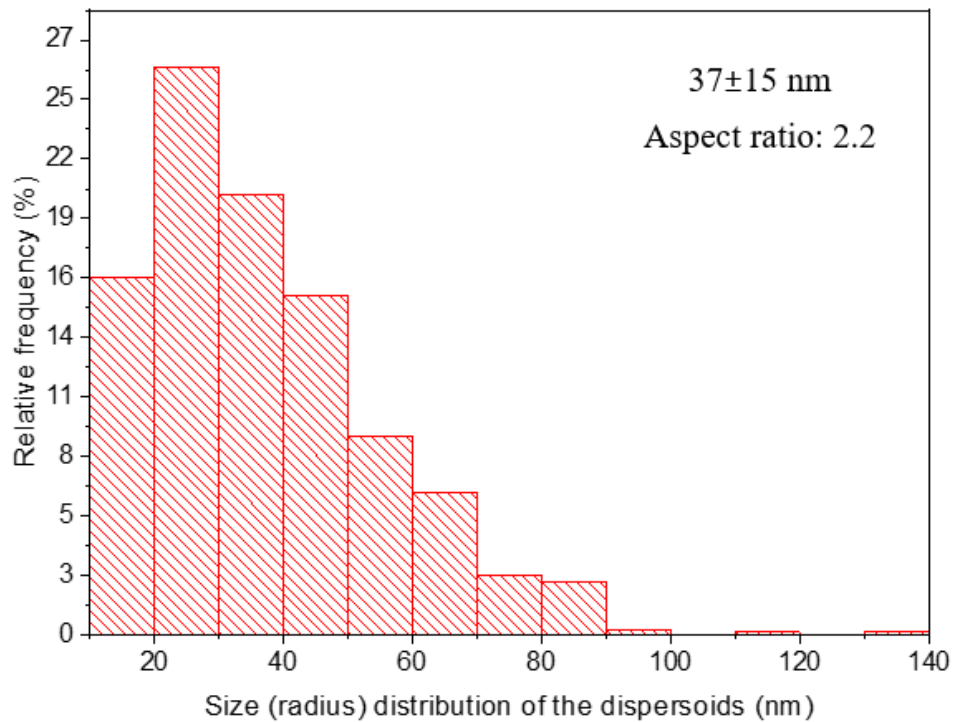


Figure 4.3: Size distribution of the dispersoids present in alloy A612

The optical microscope image of the as-extruded microstructure etched with Baker's reagent is shown in Figure 4.4. The presence of peripheral coarse grains (PCG) can be observed from the Figure 4.4 ($\approx 300 \mu\text{m}$ in thickness on the top and bottom surface of the extrudate). To simplify the analysis of the results, these surface layers were removed from the starting material as described in the next section.

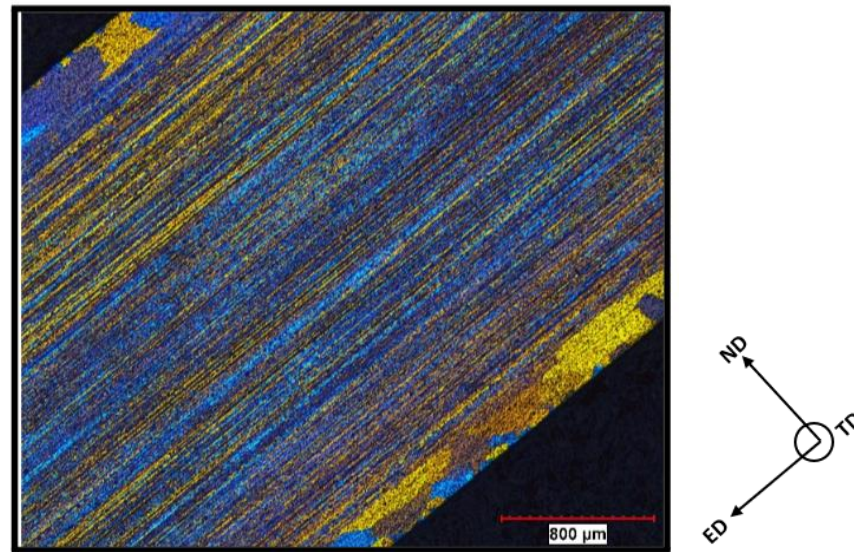


Figure 4.4: Optical microscope image of the as-extruded microstructure, etched with Baker's reagent and viewed under polarized light (from Rio Tinto Aluminium)

4.3 Removal of PCG layer

The PCG layer was dissolved by chemical etching with 100 g/L NaOH solution at a temperature of 50 – 60 °C. The thickness of the extruded strip as a function of etching time is shown in Figure 4.5. The average removal rate for the material was calculated to be 13.2 μm/min. A duration of ≈ 50 minutes was chosen to remove ≈ 350 μm from each surface of the extrudate (i.e., removing the PCG layer on both surfaces) for all the extruded strip samples used in the experiments.

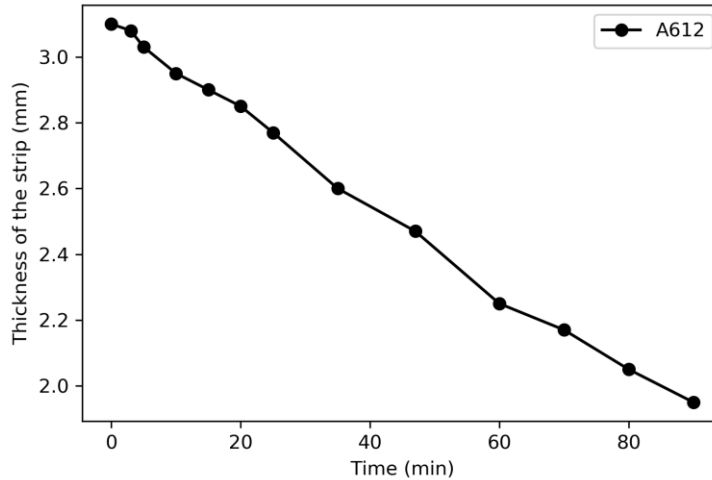


Figure 4.5: Variation of sample thickness with etching time for the initial material

4.4 Solution heat treatment and cold rolling

The Mg_2Si solvus temperature and the solidus temperatures were predicted to be 538.9 °C and 578.9 °C respectively, using the Thermocalc software (TTAL6 database). Based on this, a solution temperature of 550 °C with a holding time of 5 minutes was selected (the effect of dissolution time was studied by Sarmady [60]). The heat treatment was conducted in a salt bath which had a composition of 60 wt.% KNO_3 and 40 wt.% $NaNO_2$. Unrecrystallized microstructures were obtained by solution treatment of the as-extruded strip samples (see section 5.3.1). As it was desired to also have fully recrystallized material, some samples were rolled at room temperature prior to solution treatment. The aim was to achieve an average grain size of $\approx 40 \mu m$. After trial and error, it was found that a grain size of $\approx 40 \mu m$ can be obtained using a reduction of 19% cold rolling and a subsequent solution treatment of 5 minutes at 550 °C. The cold rolling percentage (% CR) was defined by:

$$\% CR = \frac{(t_i - t_f)}{t_i} \times 100 \quad (4-1)$$

where, t_i and t_f are the initial and final thickness of the sample respectively. Cold rolling was performed in multiple steps of small increments (reducing 0.1 mm in each increment) to ensure uniform thickness reduction in the sample.

4.5 Modified Jominy test and hardness testing

To determine the effect of cooling rate after the solution treatment on precipitation and hardness, modified Jominy tests (as described by Steele et. al. [84]) were conducted. The samples for the tests are shown in Figure 4.6. Unlike conventional Jominy tests where cylindrical samples are used, a strip sample was used in the current study. Type K thermocouples (≈ 0.18 mm in diameter) were spot welded using Unitek Dual Pulse 125 spot welder, on the surface to measure the temperature at different locations during cooling.

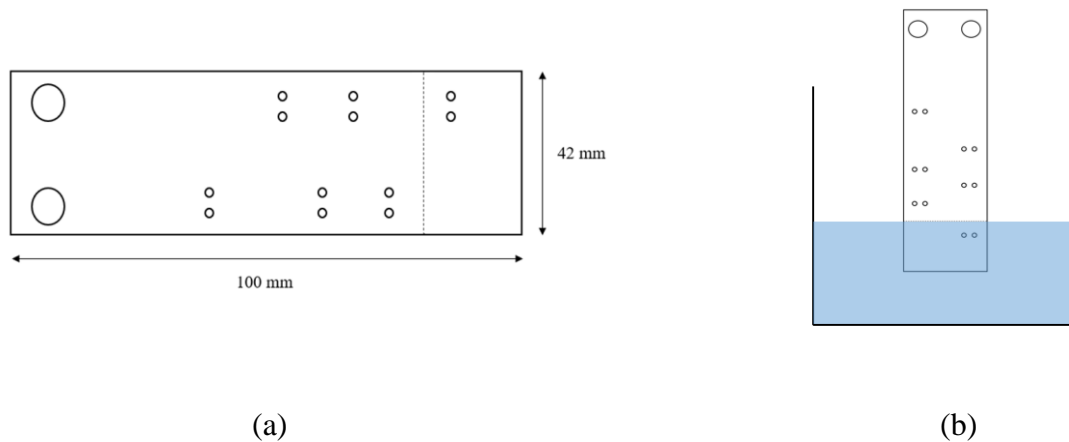


Figure 4.6: Sample used in the modified Jominy tests

Six pairs of holes were drilled in the sample to provide stability for the thermocouples at higher temperatures. The signal from the thermocouple was acquired using a thermocouple data logger

(Omega – OMB-DAQ-3000 16-bit/1-MHz USB Data Acquisition System). Cold junction compensation and the conversion of the thermocouple voltage to temperature (in °C) was done using the DASyLab 8.0 software. The samples were heat treated for 5 minutes at 550 °C in a salt bath and were then partially immersed in water (as shown in Figure 4.6b) to achieve a range of cooling rates going from 7 °C/s (near the top) to >2000 °C/s (water quenched, under the water line). In a conventional Jominy test, samples are partially quenched by spraying a controlled flow of water under the water line, however, in the current modified Jominy test, a stagnant pool of water was used. The samples were then ground with a 2400 grit paper for \approx 3 minutes, before the hardness measurements were taken. Grinding provides a smoother surface, ensuring easier and accurate measurements. Micromet3 micro Vickers hardness machine was used for hardness testing with a 1 kg load and a dwell time of 10s were used. These measurements were taken within 10 min after the Jominy test to avoid significant natural ageing. A set of eight measurements were taken for each location.

4.6 Heat treatment of tensile samples

4.6.1 Water quenched and air cooled conditions

After the samples were solution treated in the salt bath (5 min at 550 °C), they were either immediately immersed in a beaker of water at room temperature (water quenched) or left sitting on the bench at room temperature where it took \approx 2 minutes to cool to room temperature (air cooled). The cooling rates for air cooled recrystallized and unrecrystallized alloys were found to be 5 °C/s and 4 °C/s, respectively. These cooling rates were measured from the data obtained from spot-welded thermocouples, over a temperature range of 400 – 300 °C.

4.6.2 Intermediate cooling rates – Gleeble

Intermediate cooling rates of 10, 25 and 80 °C/s were obtained using the Gleeble 3500 thermal simulator. The setup for Gleeble testing is shown in Figure 4.7. The quench head used is shown in Figure 4.8. The low force jaws setup was used for these tests with stainless steel inserts clamping the strip sample (see Figure 4.7). The stroke of the hydraulic piston was adjusted to ensure minimal compressive force on the sample during heating and holding. This was done to prevent the sample from failing during the tests i.e., the sample is very soft at 550 °C.

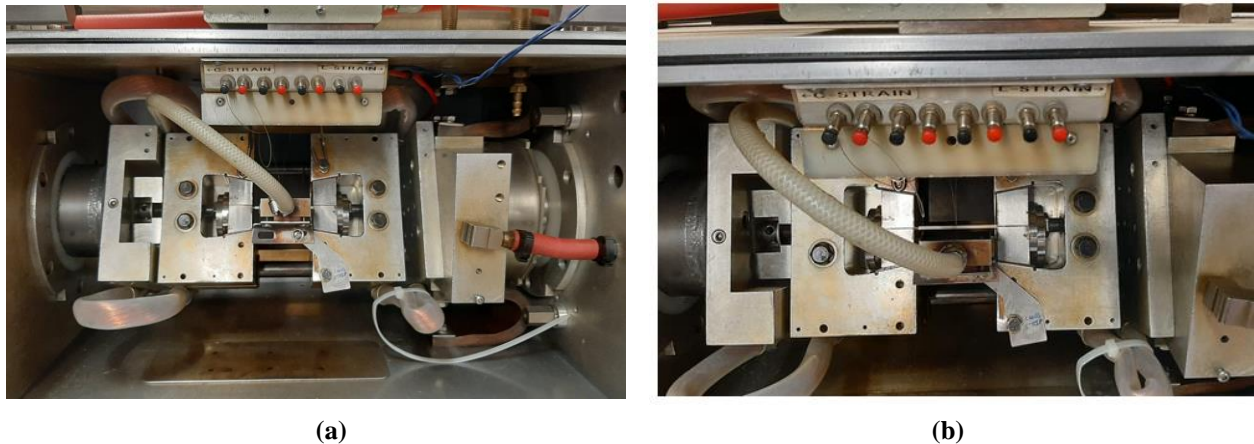


Figure 4.7: (a) Gleeble testing setup (b) Gleeble sample held by steel grips



Figure 4.8: Quench head used in the Gleeble heat treatment

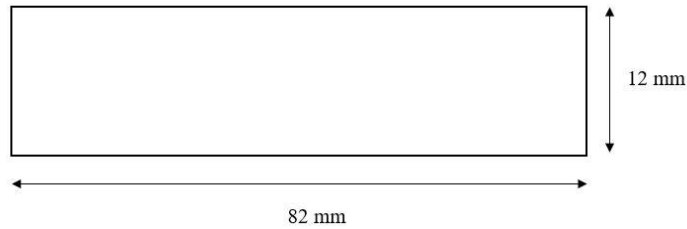


Figure 4.9 Samples used for Gleeble tests

To control the temperature, a K type thermocouple was spot welded to the center of the sample. For both unrecrystallized samples and the recrystallized samples, the heating chamber was pumped down to a vacuum of 3×10^{-1} Torr. Once this vacuum was achieved, the tank was back filled with Argon gas until a pressure of 10psi was displayed on the meter. To minimize the failure of the spot-welded thermocouples, a two-step heating stage was programmed. Up until 530 °C a heating rate of 5 °C/s was used and then a heating rate of 0.5 °C/s was used from 530 °C to 550 °C. The heating parameters TC1.kp and TC1.ki were set to 0.008 and 0.2 respectively. Helium gas was then purged through a quench head, on one side of the sample, at different pressures to obtain different cooling rates. The initial He gas pressure used for different cooling rates are summarized in the Table 4.2.

Table 4.2: Initial He pressure used for different quench rates

Quench Rate	10 °C/s	25 °C/s	80 °C/s
Initial pressure	2 Psi	6 Psi	40 Psi

The He pressure was manually adjusted during the quench to maintain a uniform heat power from the Gleeble.

tests were converted to engineering stress (s) and engineering strain (e) using the measured initial area of the sample. Equations 4-2 and 4-3 were used to convert engineering stress-strain to true stress (σ) and true strain (ε).

$$\sigma = s(1 + e) \quad (4-2)$$

$$\varepsilon = \ln(1 + e) \quad (4-3)$$

Further, true fracture stress (σ_f) and true fracture strain (ε_f) were calculated using equations 4-4 and 4-5.

$$\sigma_f = \frac{F_{fracture}}{A_{projected}} \quad (4-4)$$

$$\varepsilon_f = \frac{A_{initial}}{A_{projected}} \quad (4-5)$$

where $A_{projected}$, the projected fracture area, was calculated using the ImageJ software with the fracture images taken from the SEM. An example of an image taken from SEM is shown in Figure 4.11a.

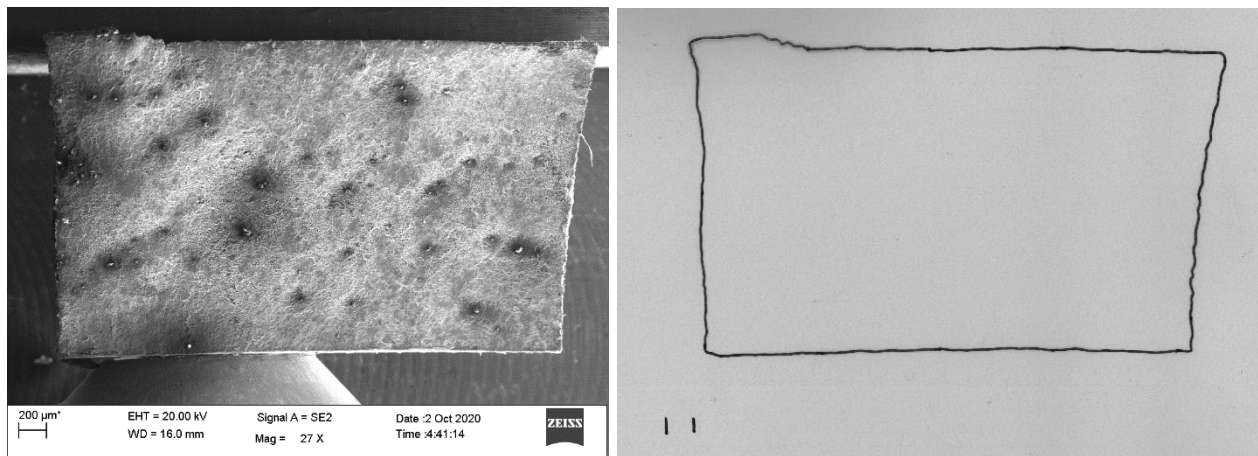


Figure 4.11: (a) An example of a fracture surface image taken using SEM and (b) traced edges of the fracture surface image shown in (a)

Using Figure 4.11a, the sample edges were traced (as shown in Figure 4.11b) and was used in ImageJ to calculate the area. For both yield stress and fracture properties measurements, three samples were tested in each condition.

4.9 Microstructure characterization

4.9.1 Metallography

In order to measure the grain size and to observe the grain boundary precipitates, samples were first ground and polished as follows:

- 400 grit SiC paper for ≈ 1 minute with water as the lubricant
- 800 grit SiC paper for ≈ 2 minutes with water as the lubricant
- 1200 grit SiC paper for ≈ 5 minutes with water as the lubricant
- 2400 grit SiC paper until all visible scratches were removed
- 1 μm Texmet cloth for ≈ 15 minutes with 1 μm diamond suspension as the polishing solution and RedLube as the lubricant
- 0.05 μm Chemomet cloth with colloidal silica as the polishing solution until a smooth and reflective surface was obtained

4.9.2 Scanning Electron Microscope (SEM)

SEM was used to observe the precipitates formed at the grain boundaries. The polished samples were electro-etched with a solution of 150 mL nitric acid and 350 mL methanol. The setup used for electro-etching is shown in Figure 4.12. The etchant was put in a metallic beaker, that was placed in another beaker containing liquid nitrogen. Both the metal beaker and the sample were connected to a power source with a voltage of 9 V, with the positive terminal connected to the

sample and the negative terminal to the beaker. Once the etchant reached a steady temperature of $-20\text{ }^{\circ}\text{C}$, the polished surface was held in the solution for 15 seconds. The samples were then observed on the Zeiss FEG-SEM under secondary electron (SE) and back scattered electron (BSE) mode. A magnification of 4000 x was used for the characterization.



Figure 4.12: Setup used for electro-etching

These SEM micrographs were then used to measure the size of precipitates. ImageJ was used to measure the average major and minor axis lengths of the grain boundary precipitates. Figure 4.13 shows an example of a SEM image used in the measurement.

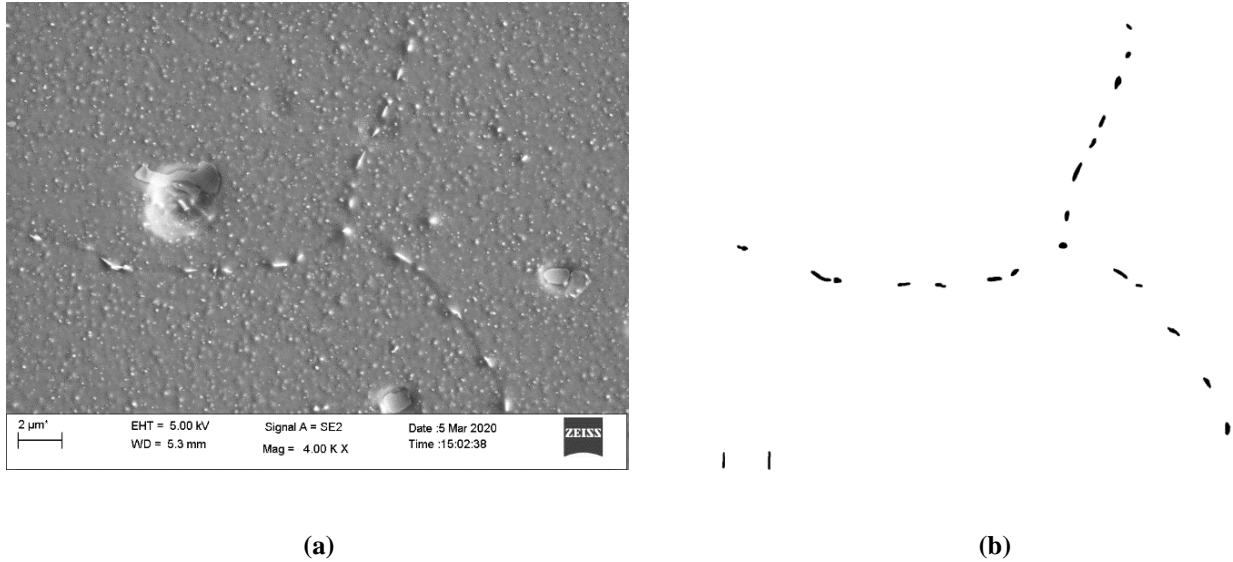


Figure 4.13: (a) An example of a grain boundary precipitate image taken using SEM and (b) traced precipitate particles from (a)

Using Figure 4.13a, grain boundary precipitates were traced (Figure 4.13b) and was used in ImageJ to calculate the average major and minor axis precipitate sizes.

4.9.3 Fracture surfaces

To investigate the effect of cooling rates on the mode of fracture, fracture surfaces from tensile samples were observed in the Zeiss FEG-SEM under the secondary electron mode. These images were used to differentiate the transgranular mode of fracture from the intergranular mode. Figure 4.14 shows an example of an image used for the classification. An example of an area identified as intergranular fracture is indicated by the blue circle. The dimples on the other hand (indicated by the white circle), were classified into transgranular fracture.

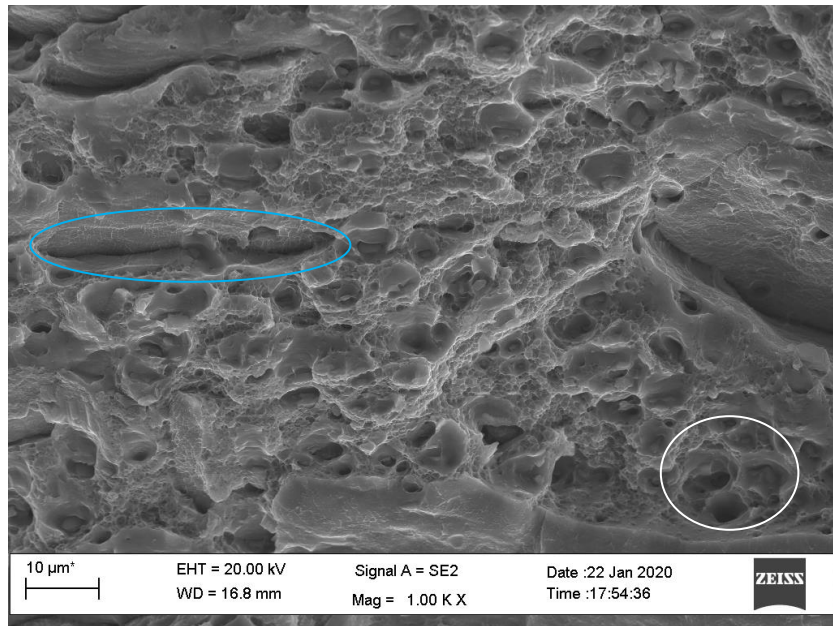


Figure 4.14: (a) An example of a fracture surface image used to identify the mode of fracture

4.9.4 Electron Backscattered Diffraction (EBSD)

EBSD was used to measure the average grain size and to analyze the texture of the material.

EDAX TSL Orientation Imaging Microscopy (OIM 6th edition) software was used to obtain the data for EBSD. The different parameters used to obtain EBSD maps are summarized in Table

4.3.

Table 4.3: Various parameters used in the EBSD

Acceleration Voltage	20 kV
Aperture size	120 μm
Working distance	13 mm
Capture speed	≈42 fps
Grids	Hexagonal

TSL OIM analysis software was used for post processing the EBSD data. The following cleanup procedure was used before the analysis:

- Confidence Index (CI) standardization with a grain tolerance angle of 10 and a minimum grain size of 4 μm
- Grain dilation and filtering out the pixels with a CI lower than 0.1

For the as-extruded and unrecrystallized conditions, a step size of 0.25 microns was used. For the recrystallized microstructure, a step size of 10 microns was used. A minimum of 3000 grains were used for texture analysis. The Bunge Euler angles used for different components is shown in Table 4.4.

Table 4.4: Bunge Euler angles for different texture components

Texture components	Bunge Euler Angles		
	Ψ_1	Φ	Ψ_2
Cube	0	0	0
Goss	0	45	0
Brass	35	45	0
S	59	37	63
Copper	90	35	45
Rotated Cube	45	0	0

4.10 Polycrystal Plasticity model

A full field polycrystal plasticity model was developed using the Linux based open source software, Düsseldorf Advanced Material Simulation Kit (DAMASK). A description of DAMASK was discussed in Section 2.10. This model was used to simulate the local stress and strain response of an Al alloy with precipitate free zones (PFZs).

4.10.1 Microstructure of the model material

The microstructure used in the model consisted of 2D hexagonal grains as shown in Figure 4.15. The microstructure was generated using Voronoi Tessellation. Two zones were defined (as indicated by the color in the Figure 4.15) within the crystals in the microstructure, a) blue representing the grain interior and b) yellow representing the PFZs adjacent to the grain boundaries.

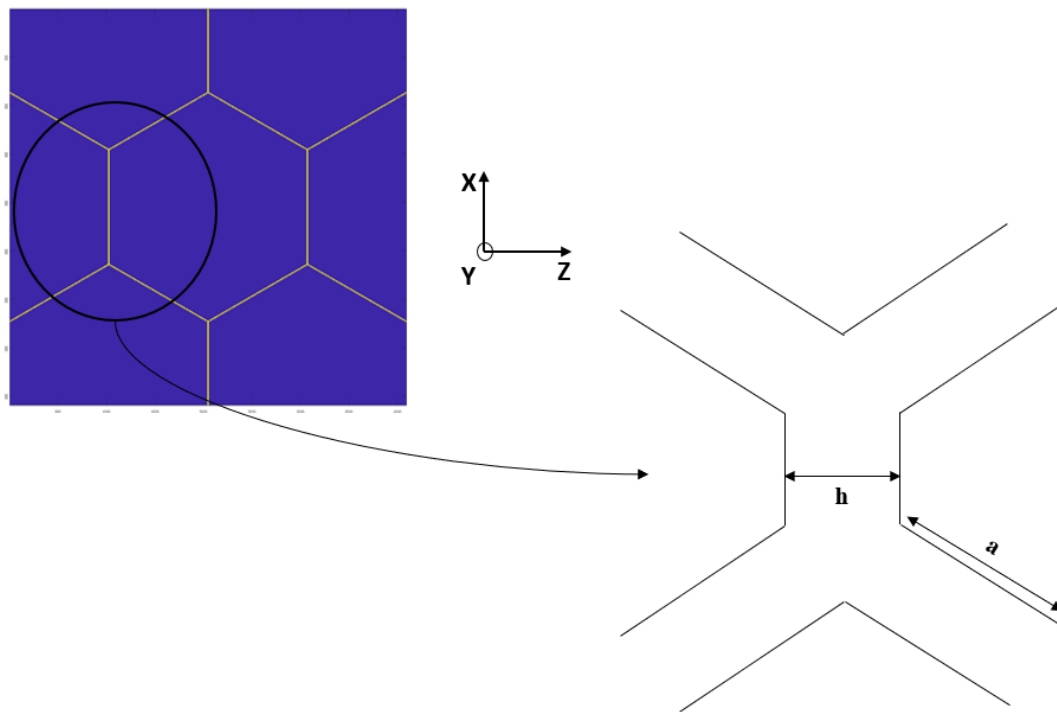


Figure 4.15: Microstructure used in the plastic deformation model

An overall resolution of 4096×4096 grids, with 14 grids on the PFZs, were used in this Fast Fourier Transformation (FFT) based solver. This resulted in a ratio of the sizes (side of the hexagon to the thickness of PFZ) to be ≈ 85 . This corresponds to a PFZ thickness (h) of 350nm and a side of the hexagon (a) of 29.6 μ m. Henceforth, this microstructure will be referred to by its a/h ratio of 85. Further, Bunge Euler angles of $\Psi_1 = 0$, $\Phi = 0$, $\Psi_2 = 0$ were used for the simulation. A periodic boundary condition was used for the cell geometry.

4.10.2 Constitutive laws

4.10.2.1 Elasticity

Generalized Hooke's law for anisotropic elasticity was employed,

$$S = C E \quad (4-6)$$

where E represents the Green Lagrange strain, S, the second Piola Kirchhoff stress and C, the elastic stiffness tensor, with $C_{11} = 106.75$ GPa, $C_{12} = 60.41$ GPa and $C_{44} = 28.34$ GPa.

4.10.2.2 Plasticity

Phenomenological crystal plasticity was used in the plastic regime [81,85]. This material model is based on Schmid's Law. According to this model, the shear stress on each slip system, $\alpha = 1, \dots, 12$, evolves asymptotically towards the saturation stress as shown in Equation 4-7.

$$\dot{\tau}_c = h_{\alpha\alpha'} h_o \left(1 - \frac{\tau_c}{\tau_s}\right)^a |\dot{\gamma}| \quad (4-7)$$

where, τ_c , τ_s and $\dot{\gamma}$ are the critical resolved shear stress, saturation shear stress and shear rate respectively, h_o is the initial hardening rate, $h^{\alpha\alpha'}$ is the latent hardening parameter (details in [86]) represented in terms of an interaction matrix (a set of 6 parameters), and 'a' is a fitting parameter. The shear strain then evolves on slip systems as shown in Equation 4-8.

$$\dot{\gamma} = \dot{\gamma}_o \left| \frac{\tau_s}{\tau_c} \right| \text{sgn}(\tau_c) \quad (4-8)$$

The magnitudes of the parameters used in the simulations are shown in Table 4.5 [82]. Default values as recommended in the manual were used.

Table 4.5: Parameters used in the phenomenological model [82]

Parameter	Value
$\dot{\gamma}_o$	10^{-3} s^{-1}
a	20
$h^{\alpha\alpha'}$	1, 1, 1.4, 1.4, 1.4, 1.4

4.10.3 Parameter fit

Three parameters for the constitutive laws, 1) shear stress at yield point (τ_c), 2) saturation shear stress (τ_s) and 3) hardening (h_o), were fit using the data obtained from tensile tests. The parameter fit is shown in Figure 4.16. The simulation was run without the presence of PFZ and the parameters were then fit using the experimental data. The grain interior was fit with the

artificially aged (T6) water quenched condition and the PFZ was fit with the ‘as solution treated’ condition.

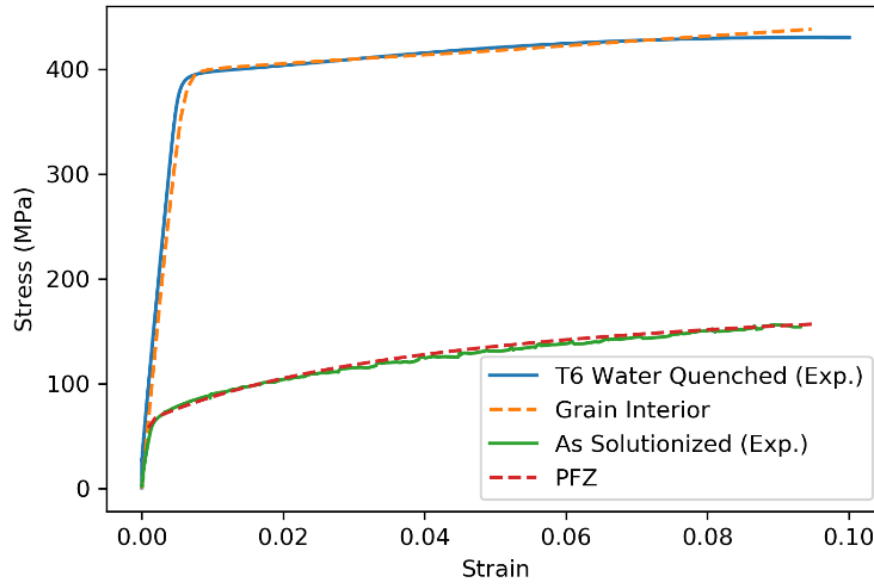


Figure 4.16: Parameter fitting from the stress strain data

Table 4.6 shows the parameters that were used for the grain interior and the PFZ.

Table 4.6: Parameters for the constitutive law for grain interior and PFZ

Parameter	Grain interior	PFZ
τ_c	171 MPa	28 MPa
τ_s	512 MPa	91 MPa
h_o	150 MPa	1000 MPa

4.10.4 Boundary condition

The material was subjected to uniaxial tensile test with the following boundary condition,

$$\sigma = \begin{bmatrix} * & * & * \\ * & 0 & * \\ * & * & 0 \end{bmatrix} \quad \dot{F} = \begin{bmatrix} 2.5 \times 10^{-4} & 0 & 0 \\ 0 & * & 0 \\ 0 & 0 & * \end{bmatrix}$$

where \dot{F} represents the deformation gradient rate tensor and asterisk (*) indicates the unknown quantities. A total of 400 increments of \dot{F} was used in the simulation to obtain a total deformation of ≈ 0.1 .

4.10.5 Coordinate transformation

The resultant strains will be shown in Section 6.2 of Chapter 6 such that the loading direction is aligned parallel to the boundary. To rotate the axis, following equations were used:

$$\varepsilon'_{xx} = \frac{\varepsilon_{xx} + \varepsilon_{zz}}{2} + \left(\frac{\varepsilon_{xx} - \varepsilon_{zz}}{2} \right) \cos(2\theta) - \varepsilon_{xz} \sin(2\theta)$$

$$\varepsilon'_{yy} = \varepsilon_{yy}$$

$$\varepsilon'_{zz} = \frac{\varepsilon_{xx} + \varepsilon_{zz}}{2} + \left(\frac{\varepsilon_{zz} - \varepsilon_{xx}}{2} \right) \cos(2\theta) + \varepsilon_{xz} \sin(2\theta)$$

$$\varepsilon'_{xz} = \varepsilon_{xz} \cos(2\theta) - \left(\frac{\varepsilon_{xx} - \varepsilon_{zz}}{2} \right) \sin(2\theta)$$

where, ε' represents the strain in the transformed coordinate.

Chapter 5: Results

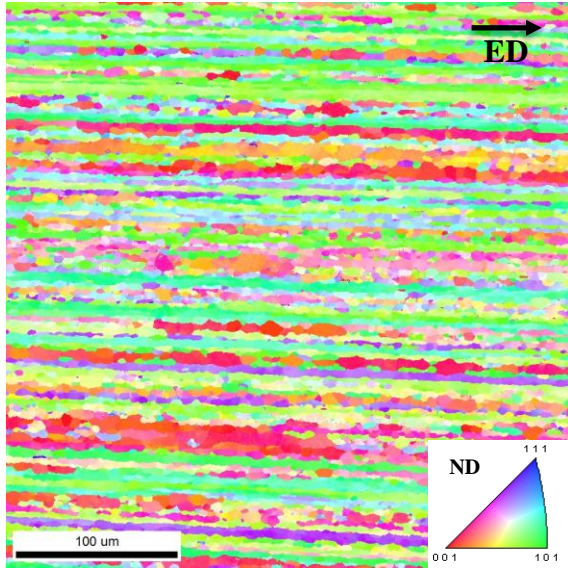
5.1 Introduction

This chapter provides a summary of the experimental work conducted in this study. This includes observations on the initial microstructure and quench sensitivity measurements using the modified Jominy test, tensile tests, and fracture properties.

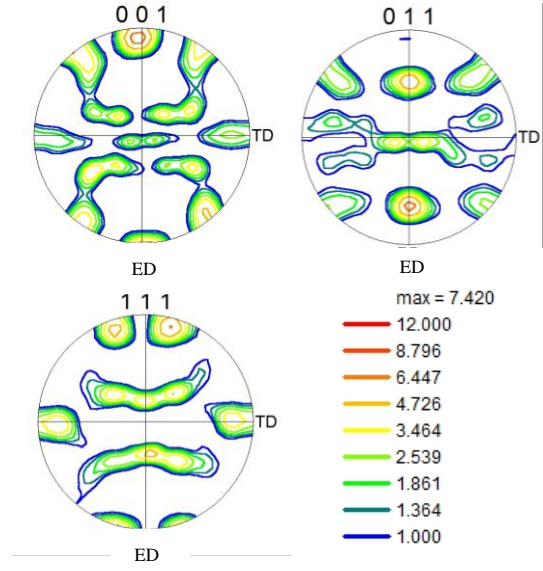
5.2 Initial microstructure and texture

Figures 5.1a, 5.1b and 5.1c illustrate the EBSD inverse pole figure (IPF) map, the 001, 011 and 111 pole figures, and sub-grain size distribution of the as-received alloy, respectively. The extrusion direction (ED) in Figures 5.1a and 5.1b is aligned with the horizontal direction. The microstructure consists of highly elongated grains which have equiaxed sub-grains within them.

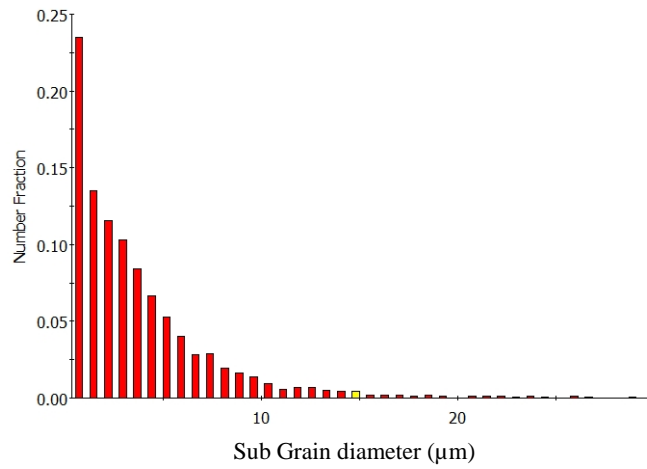
The crystallographic texture is comprised of ideal texture components consistent with the Brass, Copper and S plane strain textures and a lesser amount of Cube and Goss recrystallized components (see Table 5.1). The combination of the grain shape and crystallographic texture suggests that the as-extruded microstructure is primarily unrecrystallized with a minor amount of recrystallized grains. The average sub-grain diameter as calculated using the EDAX/TSL OIM Analysis software (6th edition) was measured to be 3.9 μm .



(a)



(b)



(c)

Figure 5.1: Characterization of the as-received alloy (a) Inverse pole Figure map (b) 001, 011 and 111 pole figures and (c) histogram of the sub-grain size distribution

5.3 Thermomechanical processing

The as-received alloy was subjected to two different thermomechanical processing routes;

- i. A solution treatment of 5 minutes at 550 °C
- ii. Rolled at room temperature to a reduction of 19%, and then a solution treatment of 5 minutes at 550 °C

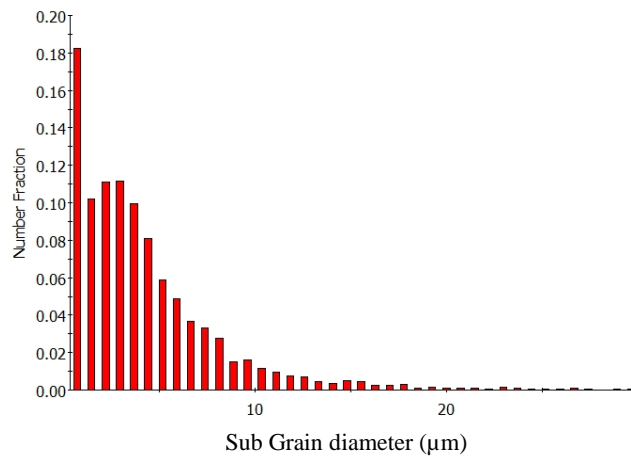
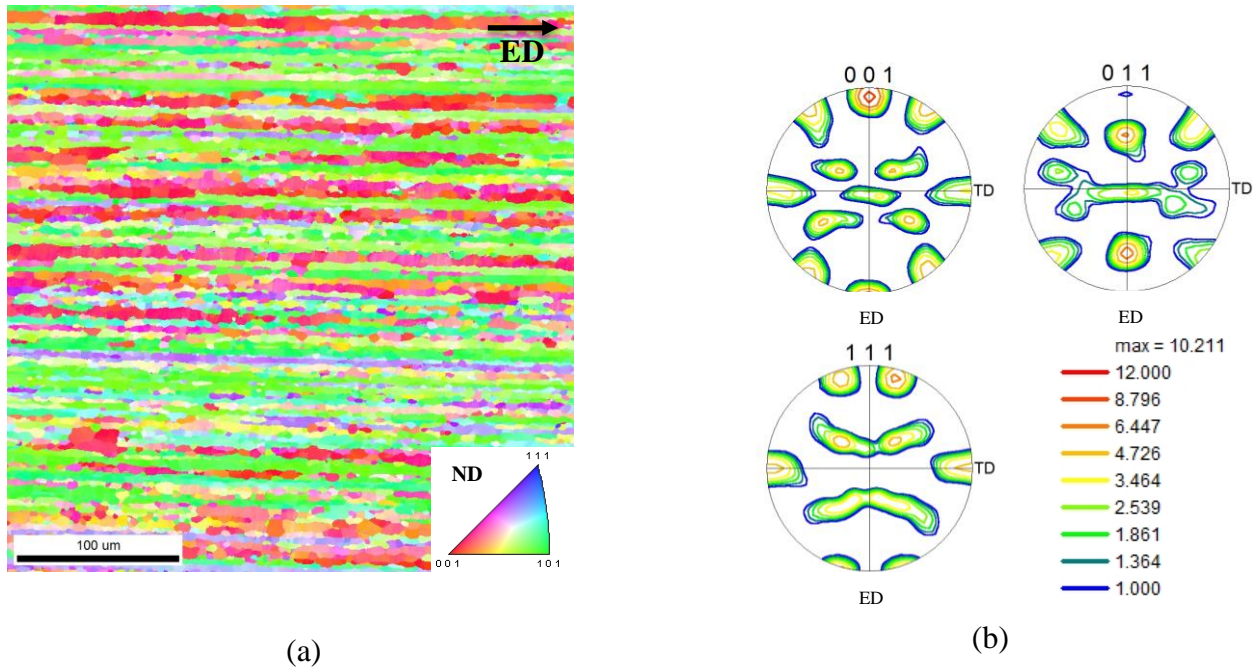
5.3.1 As extruded and solution treatment

Figure 5.2a, 5.2b and 5.2c show the EBSD inverse pole figure (IPF) map, 001, 011 and 111 pole figures, and sub-grain size distribution of the as-received alloy after a solution treatment of 5 minutes at 550 °C. The average sub-grain diameter after the solution treatment was 4.4 μm .

Table 5.1 compares the volume fractions of the major texture components found in the as-received and solution treated conditions. Crystal orientation maps, with ideal texture components (as shown in section 4.9.4 of methodology) and a tolerance angle of 15°, were used to obtain the volume fractions of these textures.

Table 5.1: Comparison of main texture components and sub-grain size for the as-received and solution treated samples, note: texture components are given in volume fraction (%)

Texture	Cube	S	Brass	Goss	Copper	Sub-grain size (μm)
As-received	11.5	14.8	16.6	2.6	6.4	3.9
Solution treated	16.8	11.1	18.5	1.1	3.8	4.4



(c)

Figure 5.2: Characterization of the as-received alloy after a solution treatment of 5 min at 550 °C (a) Inverse pole Figure map (b) 001, 011 and 111 pole figures and (c) histogram of the sub-grain size distribution

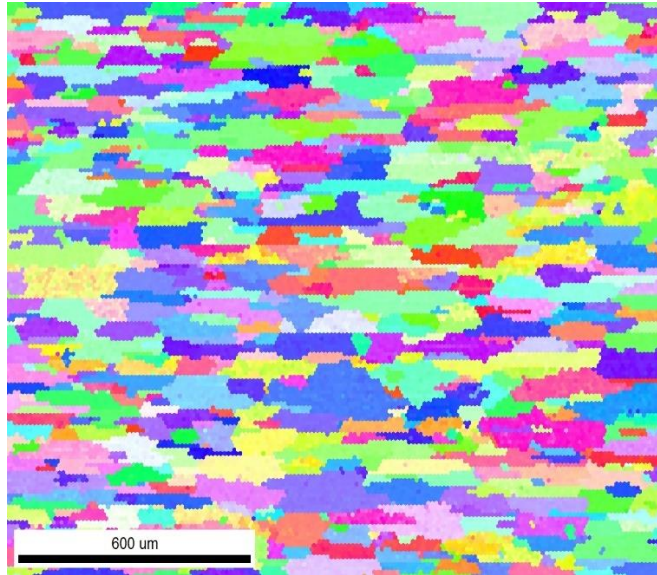
After the solution treatment, the deformed texture (S + Brass + Copper) decreased from 37.8% to 33.4%, and the recrystallized texture (Cube + Goss) increased from 14.1% to 17.9%.

The reduction in the deformed texture components and increase in the recrystallized components suggests that some recrystallization occurs during the solution heat treatment. But the overall texture is still predominantly a plane strain deformation texture. It can also be observed that increase in the average sub-grain size is modest. For simplicity, this condition will subsequently be referred to as the ‘unrecrystallized’ condition.

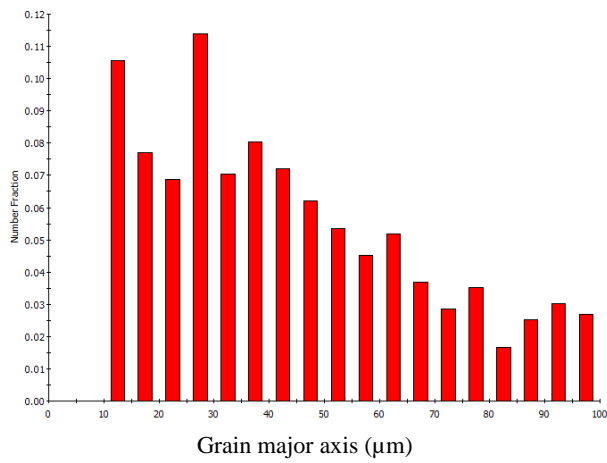
5.3.2 Cold rolled and solution treatment

Recrystallization was observed in samples that were cold rolled and solution treated for 5 minutes at 550 °C. Figure 5.3a, 5.3b and 5.3c show the EBSD inverse pole figure (IPF) map, and histograms for the major and minor axis of the grains. The average major axis grain size was 42.8 μm and the average minor axis grain size was 14.1 μm , i.e., an aspect ratio of 3 aligned with the extrusion direction. For quantification of crystallographic texture, a set of 5 IPF maps were stitched together to obtain a total of > 3000 grains, as shown in Figure 5.4a. The 001, 011 and 111 pole figures are shown in Figure 5.5b.

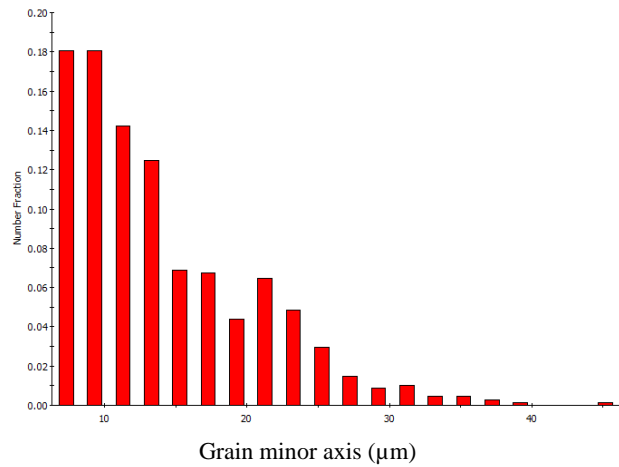
Table 5.2 summarizes the volume fraction of the major texture components for the recrystallized condition.



(a)



(b)

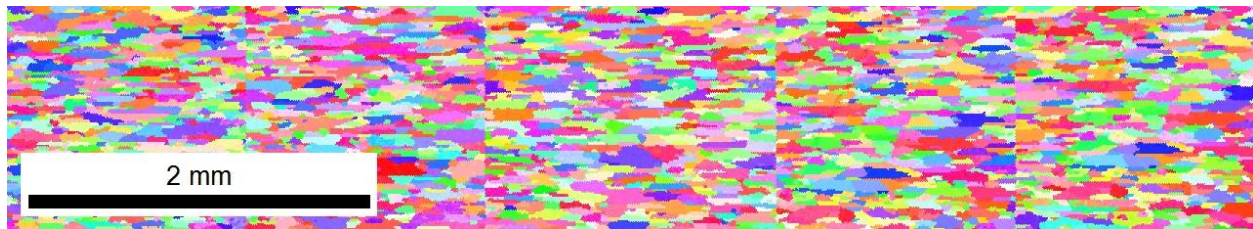


(c)

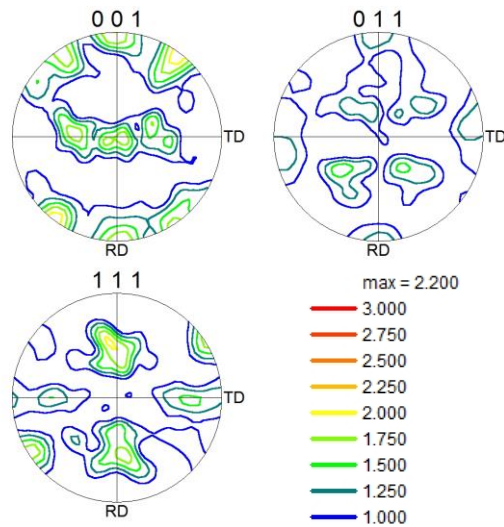
Figure 5.3: Characterization of the as-received alloy (a) Inverse pole Figure map (b) histogram for the major axis of the grains and (c) histogram for the minor axis of the grains

Table 5.2: Summary of the major texture components for the recrystallized microstructure, note: texture components are given in volume fraction (%)

Texture	Cube	R-Cube	S	Goss	Copper	Brass	Others
VF (%)	2.8	6.8	1.3	5.7	0.6	2.8	86.8



(a)



(b)

Figure 5.4: (a) Large area EBSD IPF map of a recrystallized microstructure (b) 001, 011 and 111 pole figures

5.4 Modified Jominy test

Figure 5.5a and 5.5b show the results for temperature versus time from the modified Jominy test (described in Section 4.5) for recrystallized and unrecrystallized microstructures respectively.

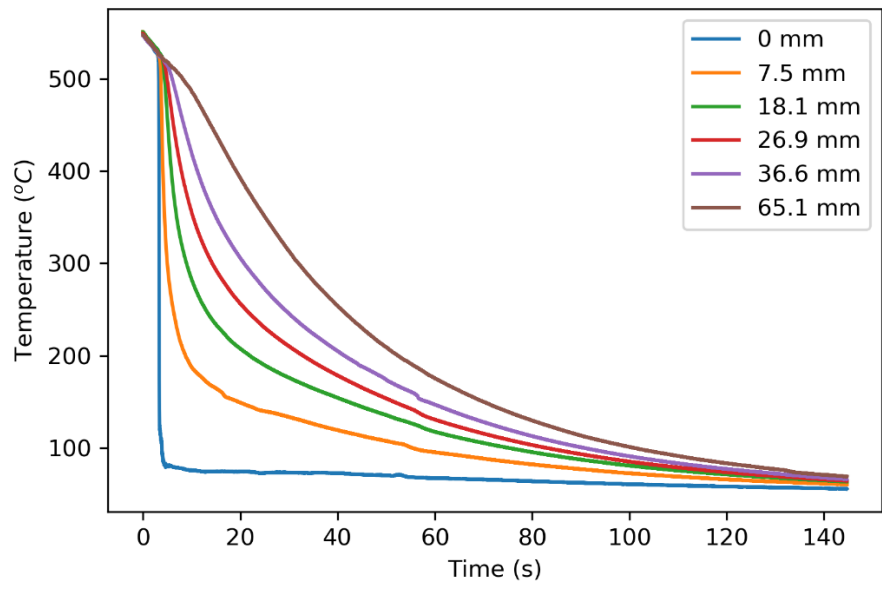
The values given in the legend for Figures 5.5a and 5.5b indicate the distance from the water line. The cooling rates were calculated from Figures 5.5a and 5.5b between 400 and 300 °C as indicated in Table 5.3 for a recrystallized microstructure and Table 5.4 for an unrecrystallized microstructure. Temperature range of 400-300 °C was chosen to calculate the cooling rate based on the literature, which suggests this is the temperature range where precipitation occurs most readily, see Section 2.8.1.1.

Table 5.3: Cooling rates calculated as a function of distance measured from the water line for the recrystallized sample

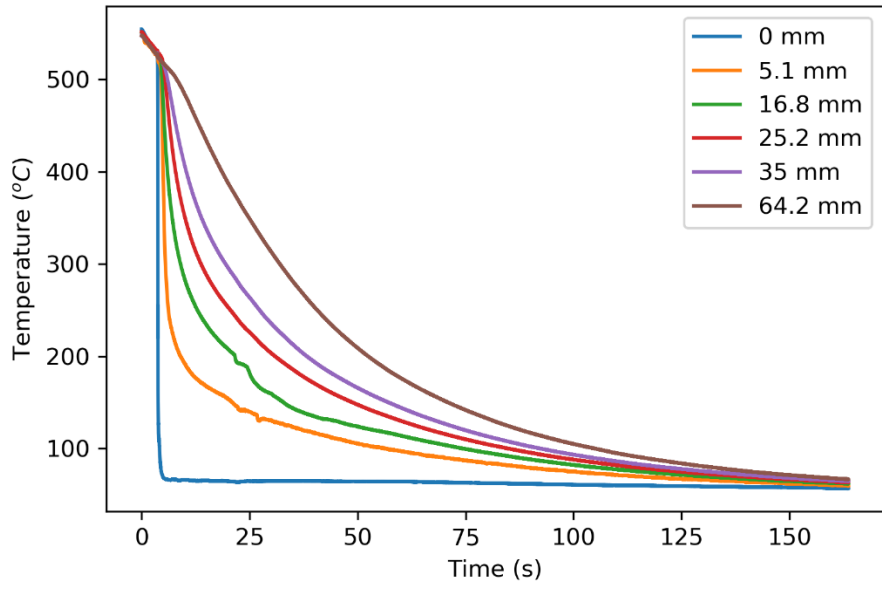
Distance from the water line (mm)	0	7.5	18.1	26.9	36.6	65.1
Cooling rates (°C/s)	>2000	112	32	16	10	7.8

Table 5.4: Cooling rates calculated as a function of distance measured from the water line for the unrecrystallized sample

Distance from the water line (mm)	0	5.1	16.8	25.2	35	64.2
Cooling rates (°C/s)	>2000	198	33	17	11	7.5



(a)



(b)

Figure 5.5: Cooling curves measured from the modified Jominy quench test for (a) recrystallized and (b) unrecrystallized microstructure

Figure 5.6 shows the variation of hardness with cooling rates for recrystallized and unrecrystallized microstructures. For both the cases, it can be observed that the magnitude of hardness increases with increasing cooling rate.

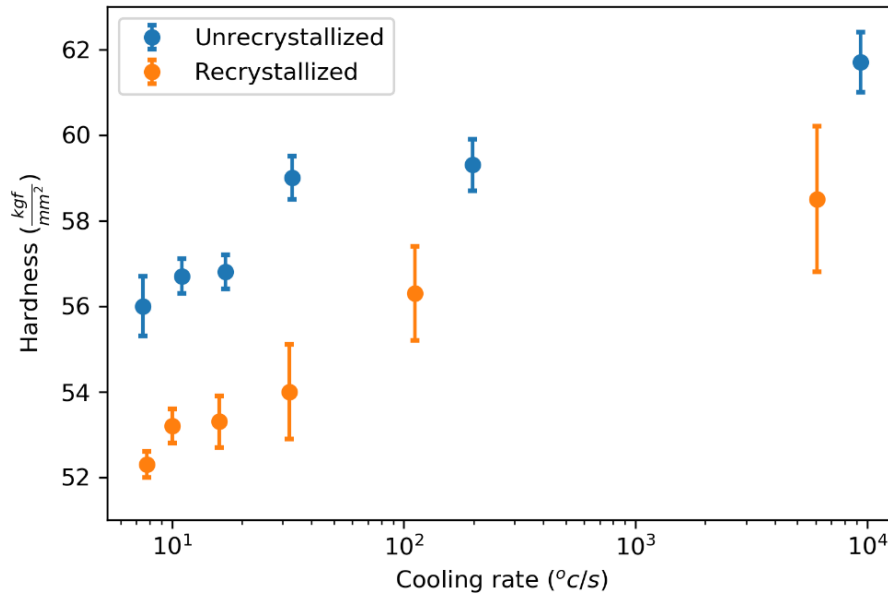


Figure 5.6: Comparison of Vickers hardness with cooling rate for recrystallized and unrecrystallized microstructures (measured within 10 minutes of the quench)

Further, Figure 5.6 also shows that the magnitude of hardness for a fixed cooling rate is higher for the unrecrystallized microstructure than the recrystallized condition by $\approx 4 \text{ kgf/mm}^2$, presumably due to the hardness contribution from the deformed grains in the unrecrystallized sample.

5.5 Observations on grain boundary precipitation

Scanning electron microscope (SEM) samples were taken from four locations of the modified Jominy test sample, with the following cooling rates:

- (a) Recrystallized: Water quenched (>2000 °C/s), 112 °C/s, 32 °C/s and air cooled (≈ 7 °C/s)
- (b) Unrecrystallized: Water quenched (>2000 °C/s), 198 °C/s, 33 °C/s and air cooled (≈ 7 °C/s)

5.5.1 Recrystallized alloys

Figure 5.7 shows the secondary electron (SE) FEGSEM images of an etched recrystallized microstructure at different cooling rates. It should be noted that the large round objects in the micrographs, as indicated by the blue arrow, are associated with the constituent particles. It can be qualitatively observed that as the cooling rate decreases (i.e., going from Figure 5.9a to 5.9d), both the size and number density of grain boundary precipitates increases. For instance, in the water quenched condition (Figure 5.9a), the grain boundary is free of precipitates (this is consistent with the TEM observations on a similar non-copper containing alloys [87]).

On the other hand, coarse precipitate particles can be observed in the grain boundaries of the sample cooled at ≈ 7 °C/s (Figure 5.9d). Also, a well-defined grain boundary can be seen in the case of the sample cooled at ≈ 7 °C/s compared to water quenched. This is due to the presence of wider precipitate free zones (PFZs) at lower cooling rates. Figures 5.9b-5.9d also show the presence of precipitates in the grain interior. These precipitates probably nucleate on the Mn, Fe containing dispersoids as suggested in the literature [35,39,45].

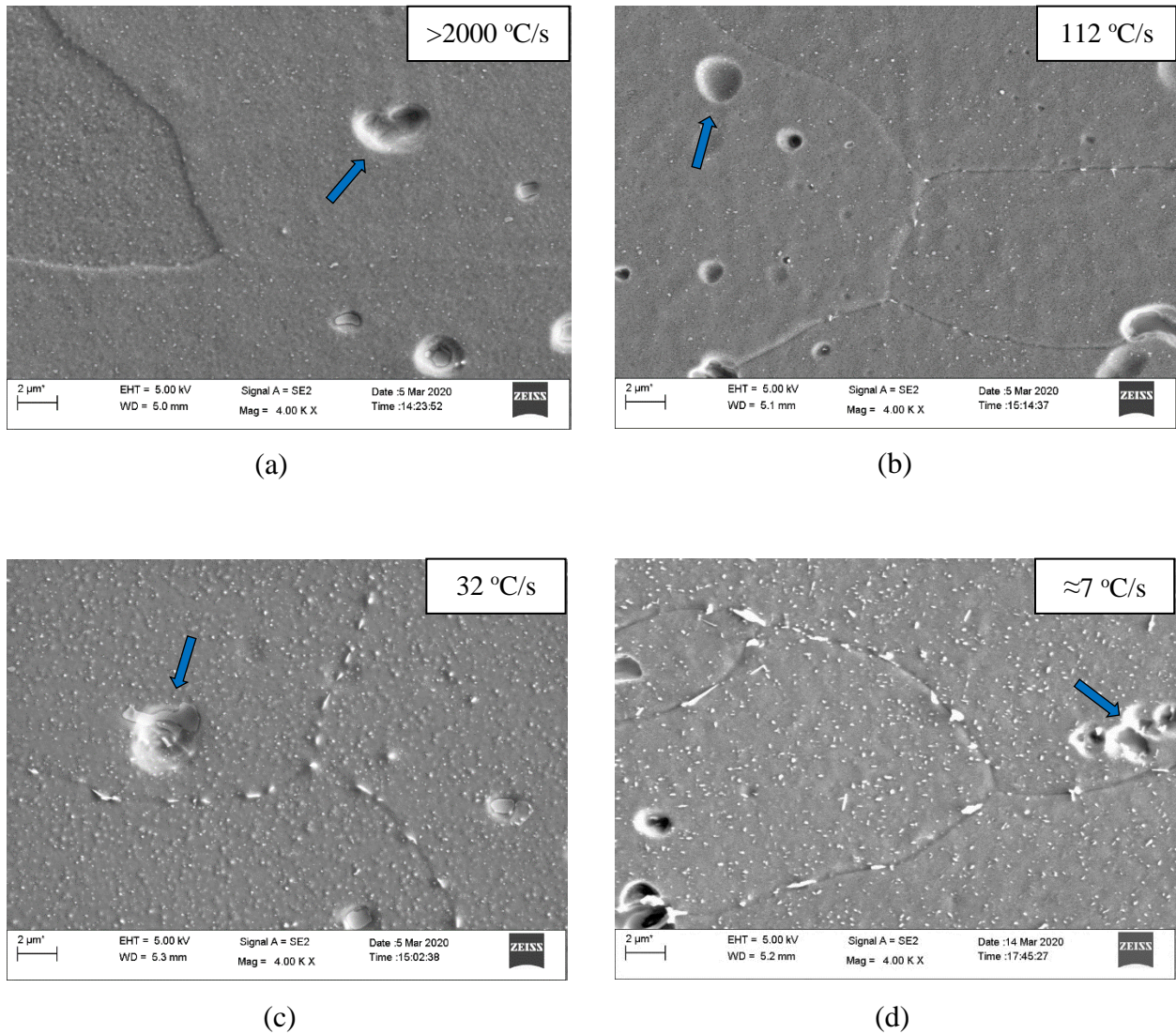
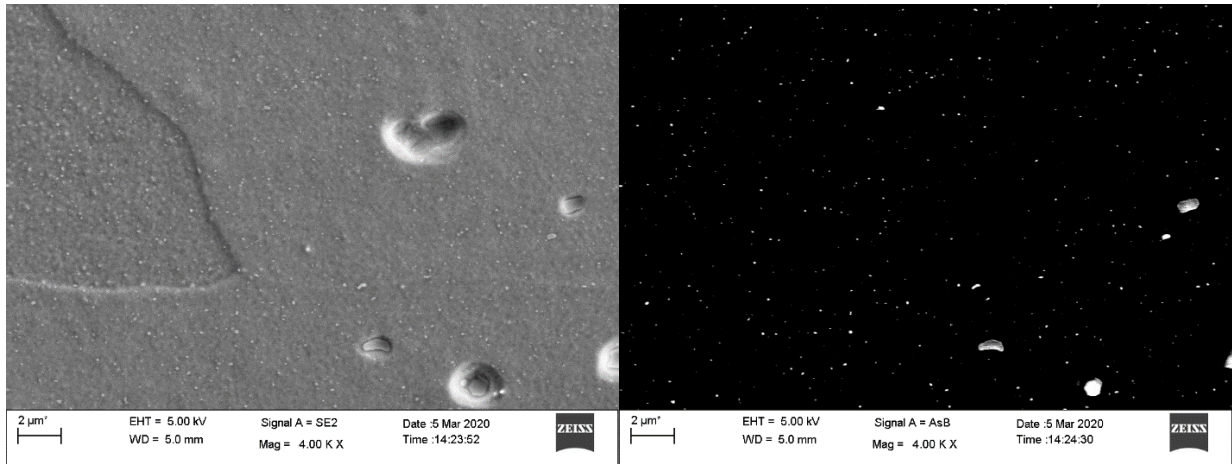


Figure 5.7: Secondary electron SEM micrographs of recrystallized microstructure at different cooling rates (a) water quenched (WQ) (b) 112 °C/s (c) 32 °C/s (d) ≈7 °C/s (AC) (T4)

The measured major and minor axis grain boundary precipitate sizes for a recrystallized alloy, are provided in Table 5.5. Figures 5.8 and 5.9 show the secondary electron and back scattered electron (BSE) images of a recrystallized sample quenched in water and cooled at ≈7 °C/, respectively.

Table 5.5: Size of grain boundary precipitates as a function of cooling rates for a recrystallized alloy

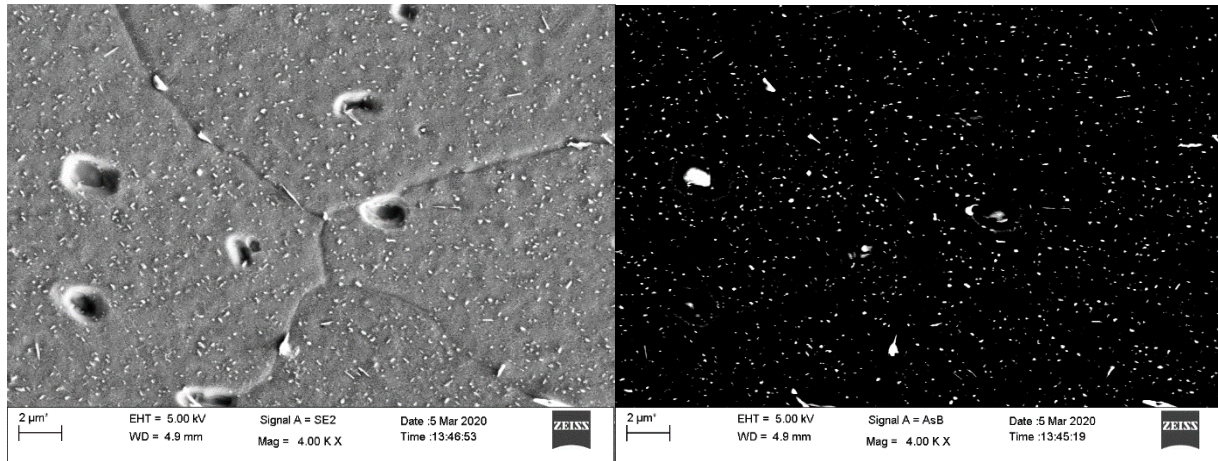
Cooling Rate	Number of particles	Precipitate major axis size (2a) (nm)	Precipitate major axis size (2b) (nm)	Aspect Ratio
>2000 °C/s	None	-	-	-
112 °C/s	13	300 ± 60	130 ± 30	2.3
32 °C/s	20	575 ± 190	200 ± 40	2.9
≈7 °C/s	17	950 ± 420	340 ± 100	2.8



(a)

(b)

Figure 5.8: FEGSEM micrographs of a water quenched recrystallized microstructure (a) secondary electron image (b) back scattered electron image (T4)



(a)

(b)

Figure 5.9: FEGSEM micrographs of a recrystallized microstructure cooled at ≈ 7 °C/s (a) secondary electron image (b) back scattered electron image (T4)

From Figure 5.8 it can be observed that the grain boundaries are free of precipitates, i.e., in the water quenched condition (Figure 5.8b), brighter particles (Fe, Mn bearing constituents and dispersoids) can be observed only in the grain interior. On the other hand, for a recrystallized microstructure cooled at ≈ 7 °C/s (Figure 5.9), particles with a higher contrast can be observed both on the grain boundaries and in the grain interior. Typically, larger atoms scatter more electrons when compared with lighter atoms. The number of back scattered electrons reaching the detector is proportional to the atomic number (Z). Hence, particles with a higher Z would have a higher contrast in a back-scattered image. Thus, for the given alloy (A612), there are two possible secondary particles that can be seen in a BSE image; Mn-Fe containing dispersoids and/or Cu containing precipitates (Q phase).

Figure 5.10 shows a high-angle annular dark-field (HAADF) TEM image of a T4 recrystallized A612 alloy cooled at 10 °C/s [87].

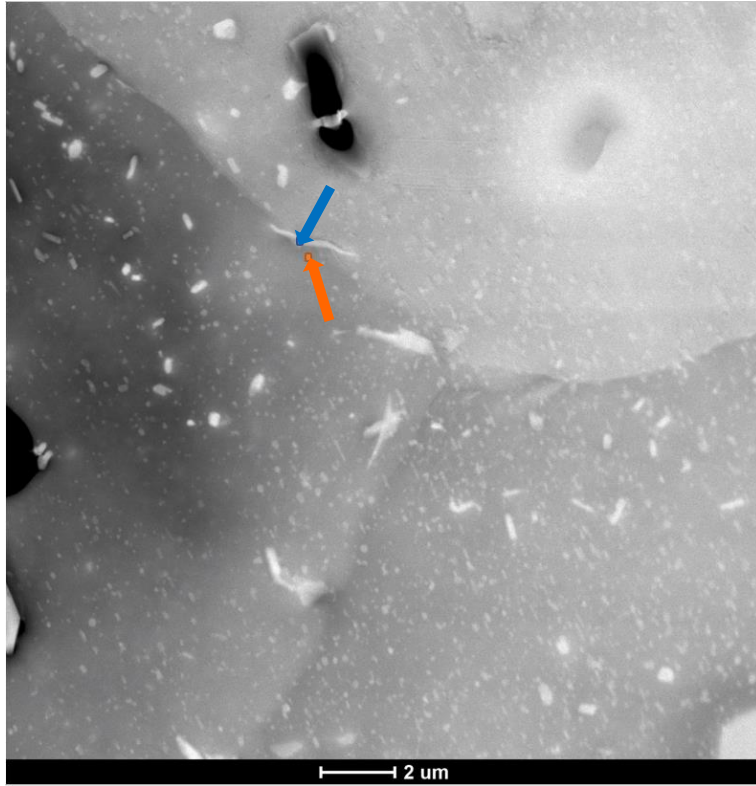
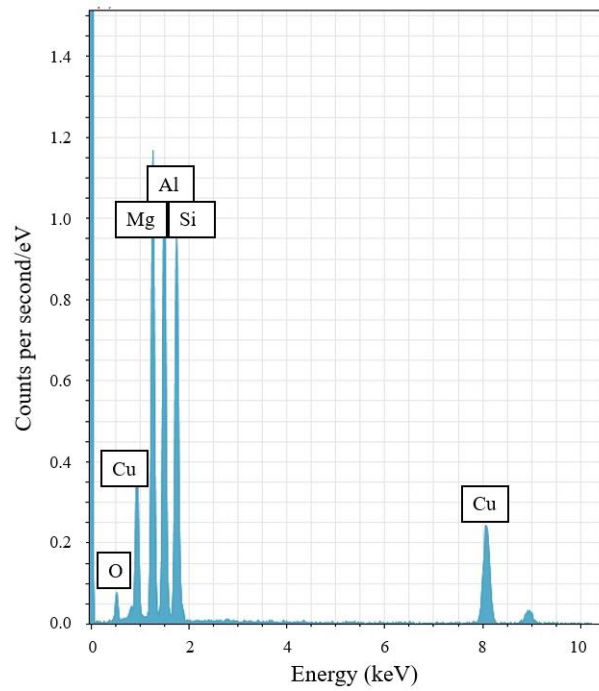


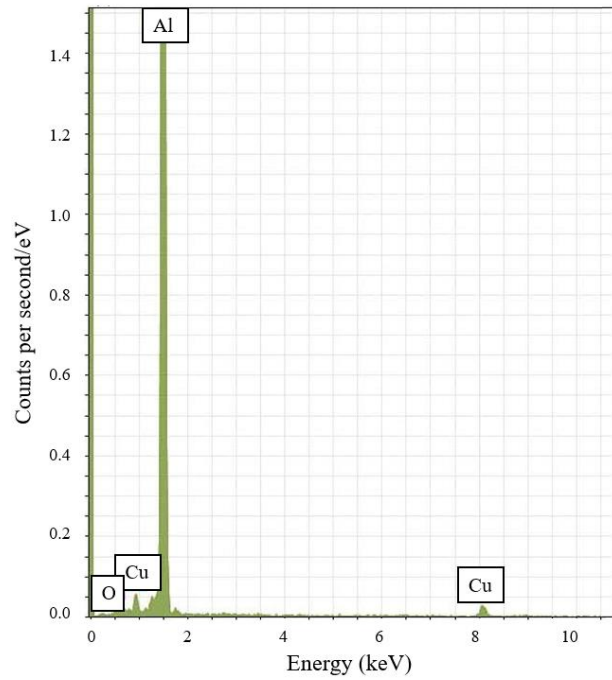
Figure 5.10: High-angle annular dark-field (HAADF) image of a T4 recrystallized sample cooled at 10 °C/s

[87]

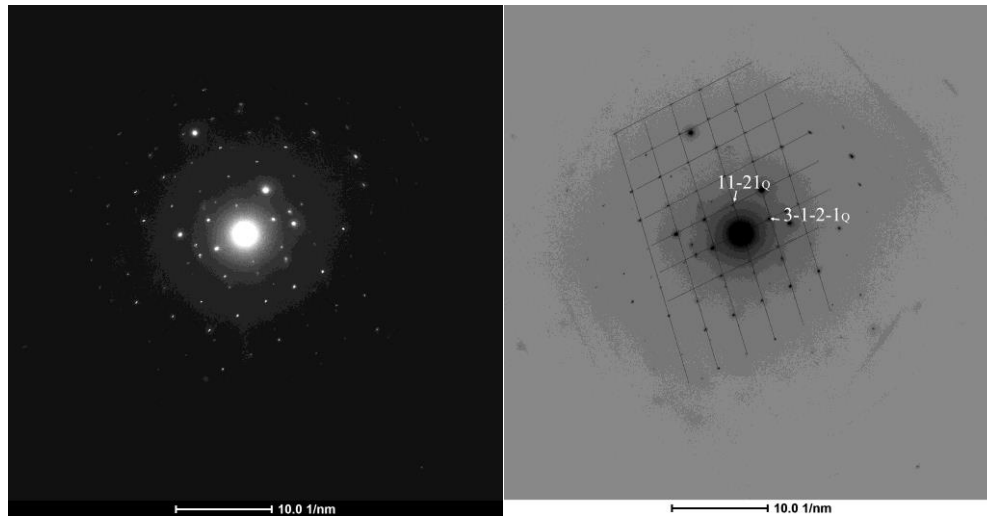
Energy dispersive spectroscopy (EDS) data and selected area diffraction (SAD) pattern for a grain boundary precipitate, indicated by the blue arrow, are shown in Figures 5.11a and 5.11c, respectively. EDS data for a point in the grain interior (orange arrow) is shown in Figure 5.11b. Presence of Cu, Mg and Si in the precipitate observed from Figure 5.11a suggest that the particle is the Q or Q' phase. The analysis of the SAD pattern (Figure 5.11b) further indicated that the lattice parameters of the measured particle were in agreement with that of the Q/Q' phase. Thus, EDS and SAD results, along with the brighter contrast in the back-scattered electron images suggest that the secondary particles precipitating at the grain boundaries in A612 alloys, during slow cooling, are Q/Q' phase. The type of precipitates nucleating in the grain interior, on the dispersoids, would require further investigation.



(a)



(b)



(c)

Figure 5.11: (a) Energy dispersive spectroscopy (EDS) data for the grain boundary particle (blue arrow) (b) EDS data for a point in the grain interior (orange arrow) (c) Selected areas diffraction (SAD) pattern for the grain boundary precipitate, indicated by a blue arrow, observed in a T4 tempered A612 recrystallized sample, cooled at 10 °C/s [87]

5.5.2 Unrecrystallized alloys

Figure 5.12 shows the SE images of an unrecrystallized microstructure at different cooling rates.

An unrecrystallized sample cooled at ≈ 7 °C/s (Figure 5.12d) shows a higher density of precipitates, both in the grain and on the boundaries, when compared with the recrystallized sample cooled at ≈ 7 °C/s (Figure 5.7d).

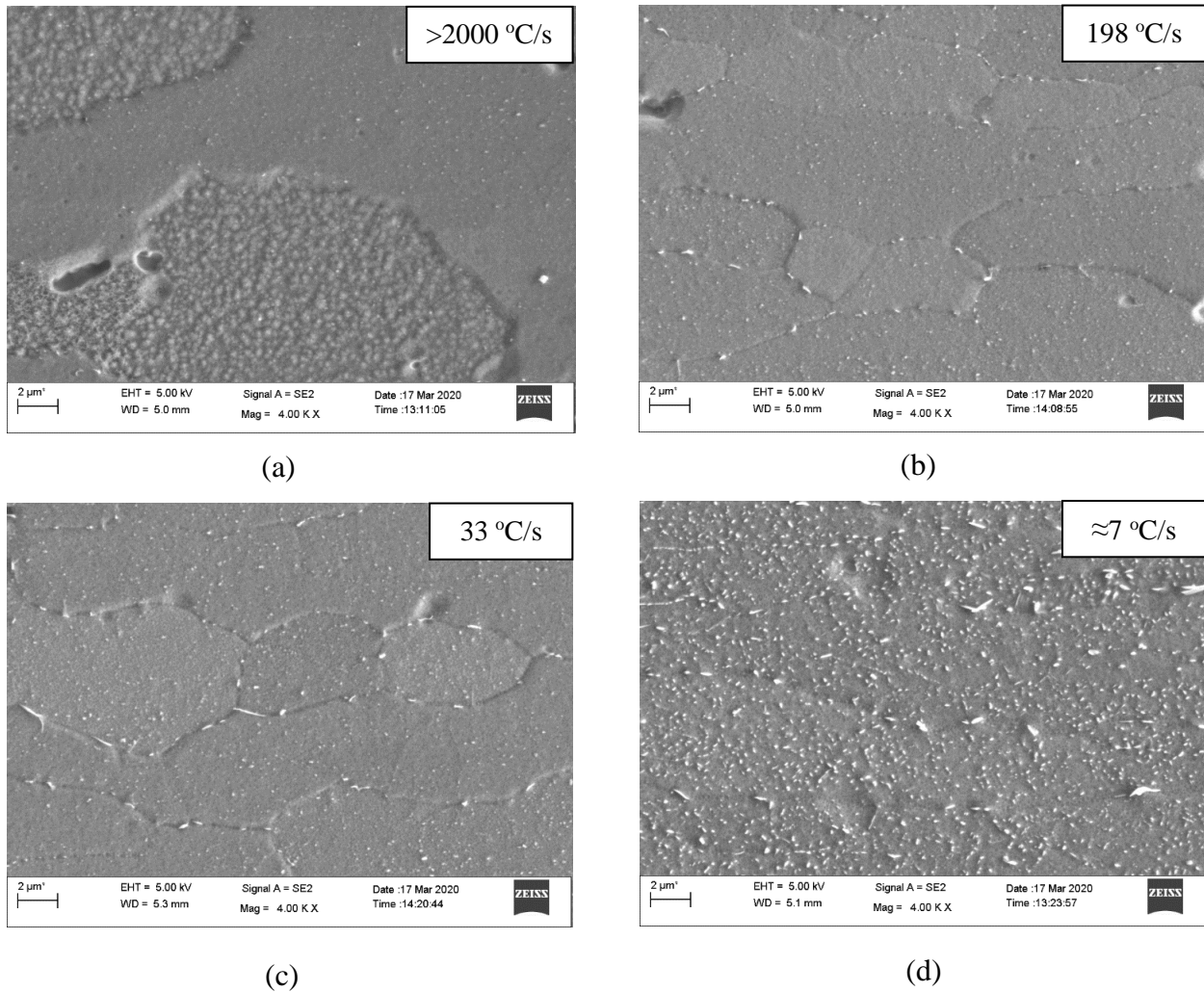


Figure 5.12: Secondary electron SEM micrographs of unrecrystallized microstructure at different cooling rates (a) water quenched (WQ) (b) 198 °C/s (c) 33 °C/s (d) ≈ 7 °C/s (T4)

Table 5.6 provides the measured size of the grain boundary precipitates for an unrecrystallized alloy. Figures 5.13 and 5.14 show the variation of major axis size and number density of grain boundary precipitates with cooling rates.

Table 5.6: Size of grain boundary precipitates as a function of cooling rates for an unrecrystallized alloy

Cooling Rate	Number of particles	Precipitate major axis size (2a) (nm)	Precipitate major axis size (2b) (nm)	Aspect Ratio
>2000 °C/s	None	-	-	-
198 °C/s	26	425 ± 130	140 ± 25	3
33 °C/s	20	540 ± 300	150 ± 30	3.6
≈7 °C/s	17	675 ± 200	220 ± 60	3.1

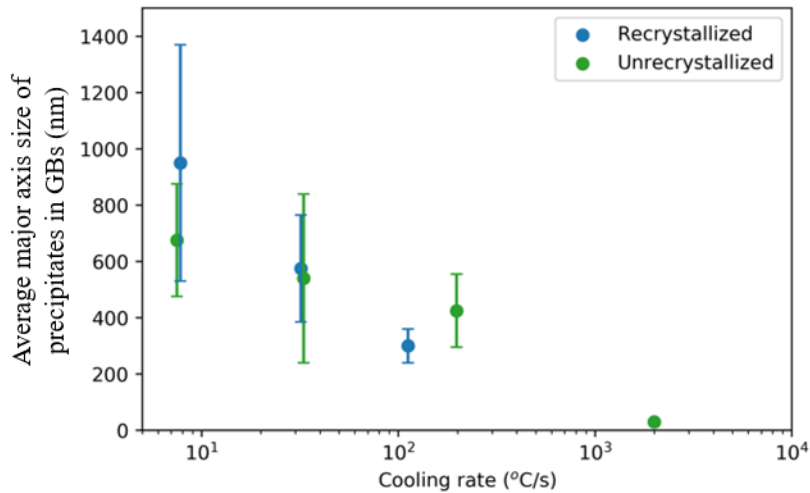


Figure 5.13: Variation of average major axis size of grain boundary precipitates for recrystallized and unrecrystallized microstructures, note: for the cooling rate of 2000 °C/s, the data points have been slightly offset so they can more easily be seen in the graph. For both cases no GB precipitation were observed, i.e., the major axis size = 0

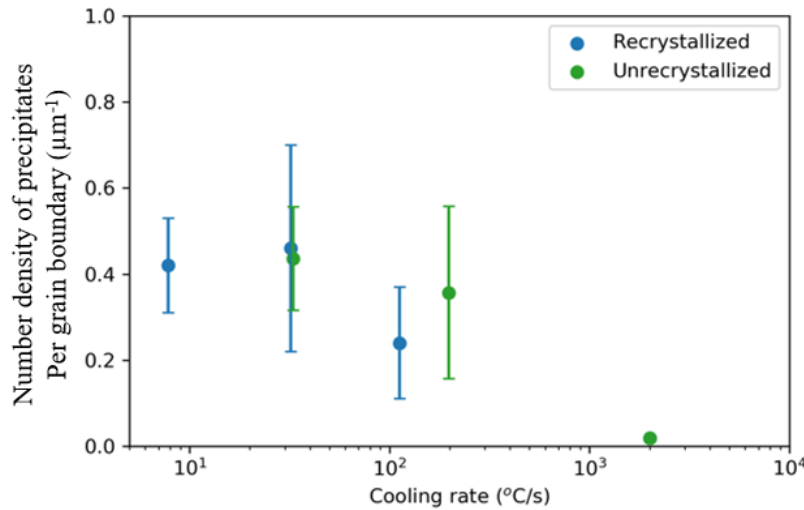
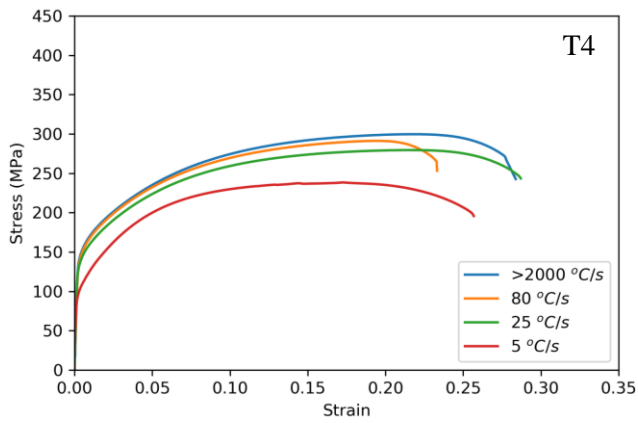


Figure 5.14: Variation of number density of precipitates per grain boundary, for recrystallized and unrecrystallized microstructures, note: for the cooling rate of 2000 °C/s, the data points have been slightly offset so they can more easily be seen in the graph. For both cases no GB precipitation were observed, i.e., the number density = 0

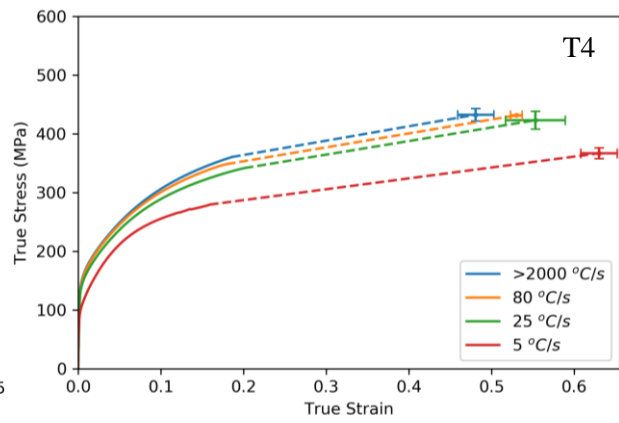
From Figure 5.13, it can be observed that the average size of the precipitates for samples cooled at ≈ 32 °C/s and ≈ 7 °C/s, is slightly higher for the recrystallized alloys than in the unrecrystallized alloys. This may be due to an inadequate number of particles measured or the different density of nucleation sites. A detailed study of the precipitates' size is suggested for future work.

5.6 Stress-Strain response

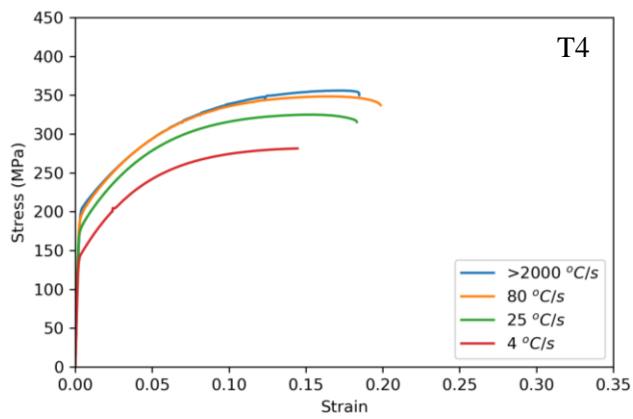
In this section, the tensile stress – strain response will be considered from samples either water quenched/air cooled or from Gleeble heat treatments, where the cooling rates were controlled. Figures 5.15 and 5.16 show the engineering stress – engineering strain and true stress – true strain curves for the T4 (1 week at room temperature) and T6 (4 hours at 180 °C) tempers, respectively. The true fracture stresses and strains were measured from the fracture area as described in Section 4.8.



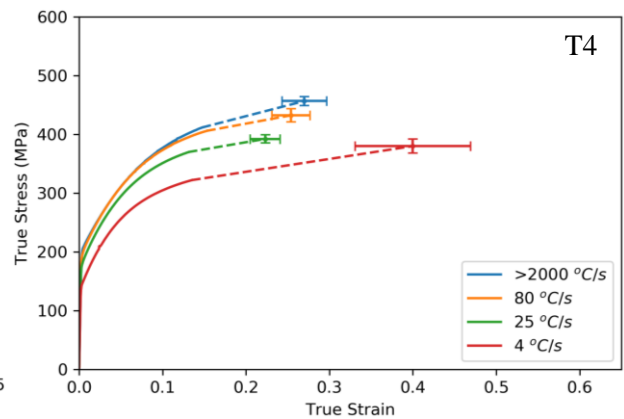
(a)



(b)



(c)



(d)

Figure 5.15: T4 tensile testing results; engineering stress- engineering strain for (a) recrystallized and (c) unrecrystallized; true stress – true strain for (b) recrystallized and (d) unrecrystallized

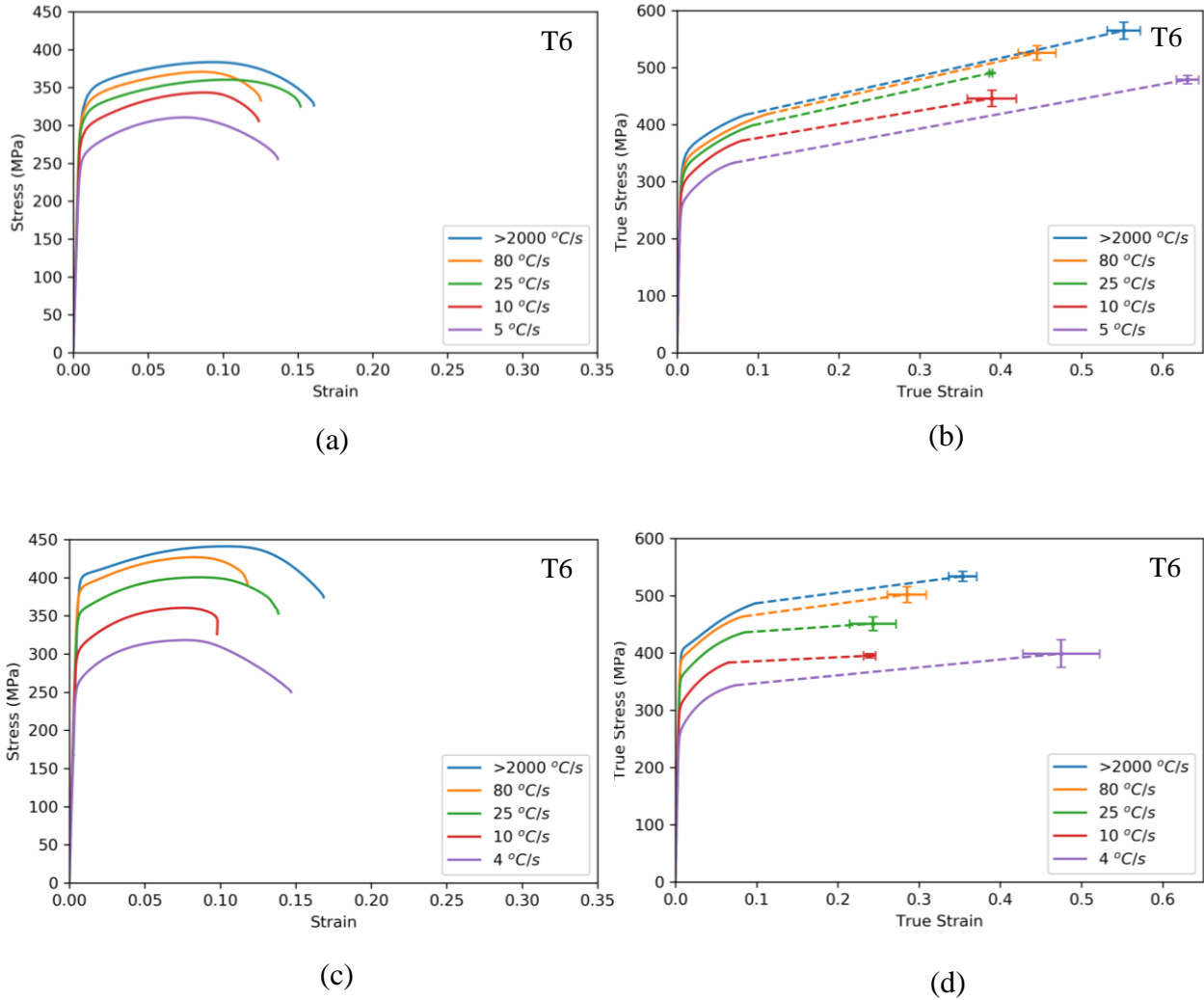
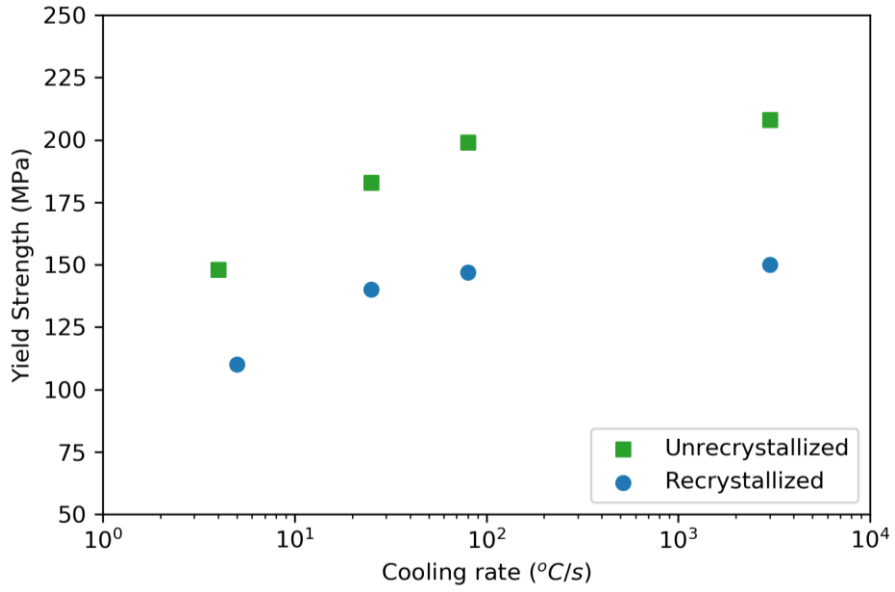
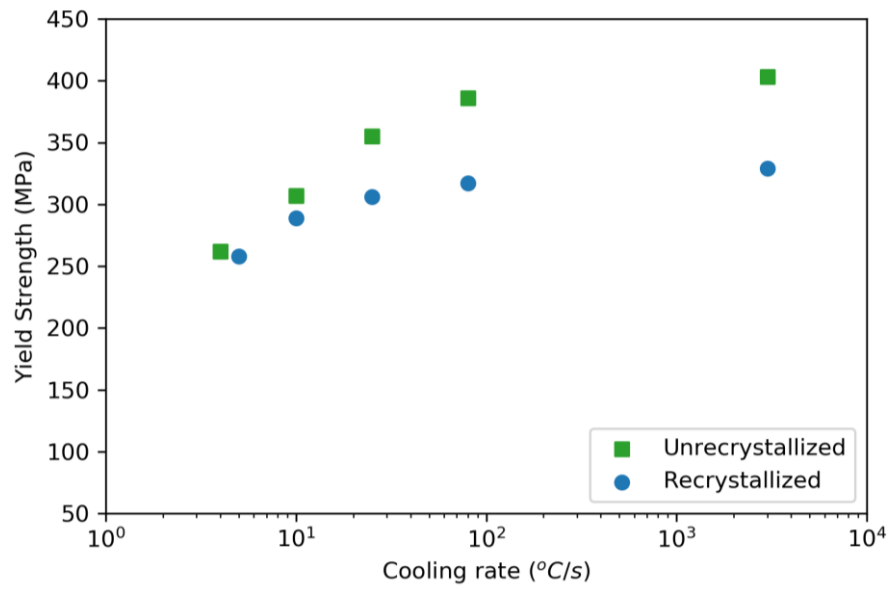


Figure 5.16: T6 tensile testing results; engineering stress- engineering strain for (a) recrystallized and (c) unrecrystallized; true stress – true strain for (b) recrystallized and (d) unrecrystallized

From Figures 5.15 and 5.16, it can be observed that both the 0.2% offset yield strength and the ultimate tensile strength (UTS) decrease with decreasing cooling rate. The variation of yield strength with cooling rate is shown in Figure 5.17a for T4 temper and Figure 5.17b for T6 temper. The variation of true fracture stress and true fracture strain with cooling rate, however, is more complicated.



(a)



(b)

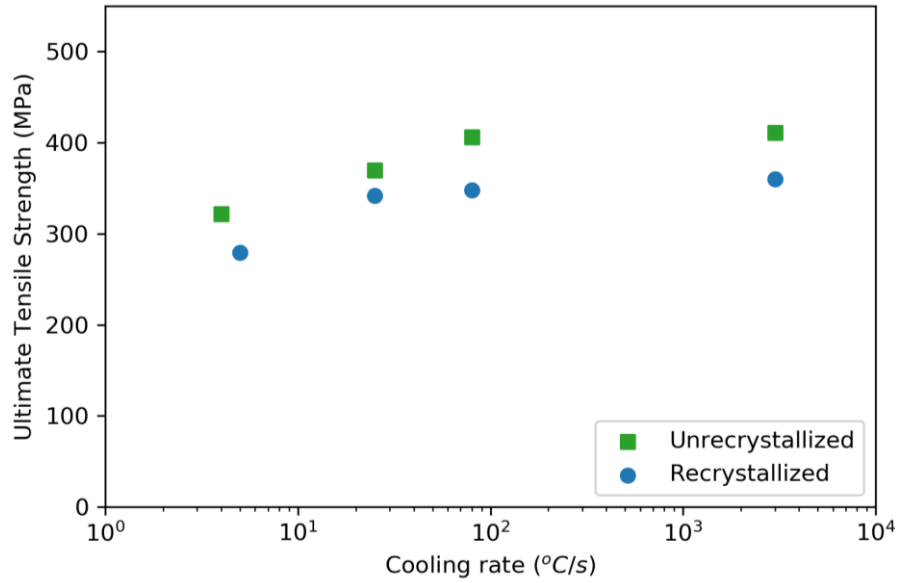
Figure 5.17: Variation of yield strength with cooling rate for both unrecrystallized and recrystallized microstructure for (a) T4 temper and (b) T6 temper

The yield stress of the as-solution treated recrystallized and unrecrystallized alloys were also measured and found to be 75 MPa and 108 MPa, respectively. Thus, it can be seen that, after one week of ageing at room temperature, the yield stress for water quenched recrystallized alloys increases by 75 MPa and the yield stress of an unrecrystallized alloy increases by 100 MPa.

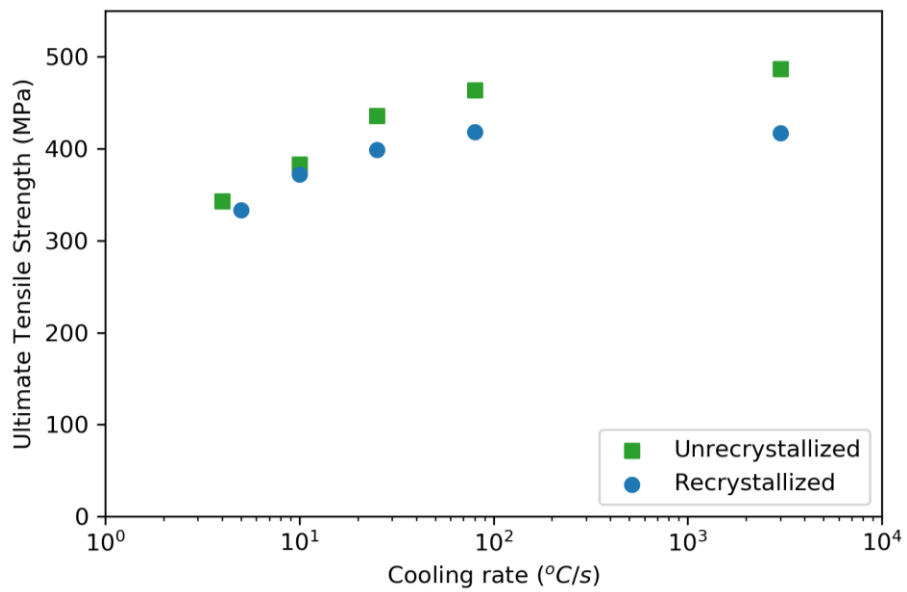
For both microstructures, the yield stress decreases with decreasing cooling rates. For the T4 tempered recrystallized sample (Figure 5.17a), the yield strength decreases from 150 MPa to 110 MPa (a difference of 40 MPa) as the cooling rate decreases from >2000 °C/s (water quenched) to 5 °C/s. For the unrecrystallized sample, the yield stress drops from 208 MPa to 148 MPa (a difference of 60 MPa).

In T6 temper (Figure 5.17b), the yield strength decreases from 329 MPa to 258 MPa (a difference of 71 MPa) for the recrystallized microstructure and from 403 MPa to 262 MPa (a difference of 141 MPa) for the unrecrystallized microstructure, as the cooling rate decreases from >2000 °C/s to 5 °C/s. Further, with increasing cooling rates, the difference in the yield strengths between the unrecrystallized and recrystallized grain structure gradually increases.

The magnitude of the drop in yield strength for the T6 condition between the unrecrystallized and recrystallized samples suggests that the unrecrystallized grain structure is more quench sensitive than the recrystallized. Figures 5.18a and 5.18b show the variation of ultimate tensile strength (UTS) with cooling rate for T4 and T6 tempers respectively. Similar to the yield stress, the ultimate tensile stress also decreases with decreasing cooling rate. The largest drop in UTS is observed for the T6 unrecrystallized microstructure, a drop of ≈ 144 MPa.



(a)



(b)

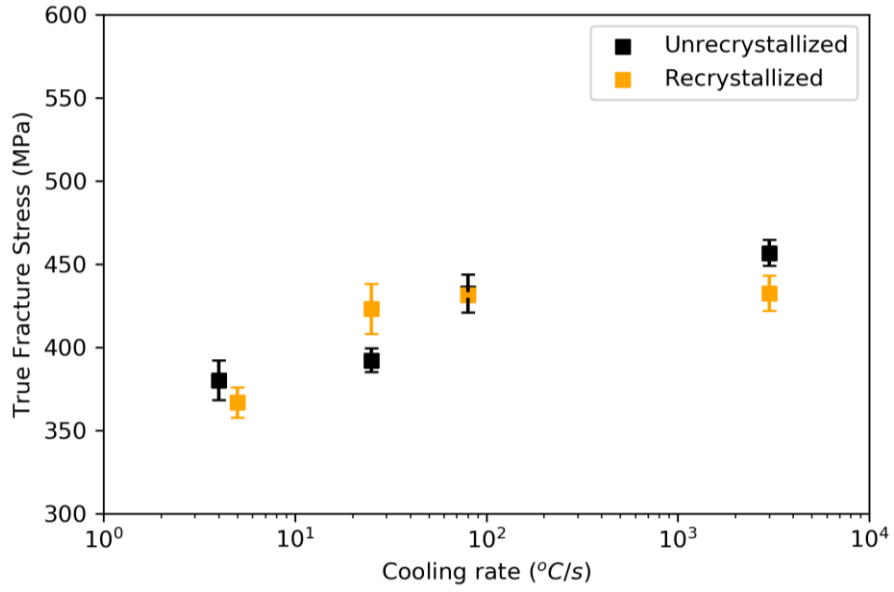
Figure 5.18: Variation of ultimate tensile strength with cooling rate for both unrecrystallized and recrystallized microstructure for (a) T4 temper and (b) T6 temper

Table 5.7 Summarizes the change in yield strength and ultimate tensile strength (difference between water quenched (>2000 °C/s) and air cooled (4-5 °C/s) conditions) for different microstructures. From Table 5.7, it can be concluded that among all the initial microstructures, T6 unrecrystallized condition is the most quench sensitive.

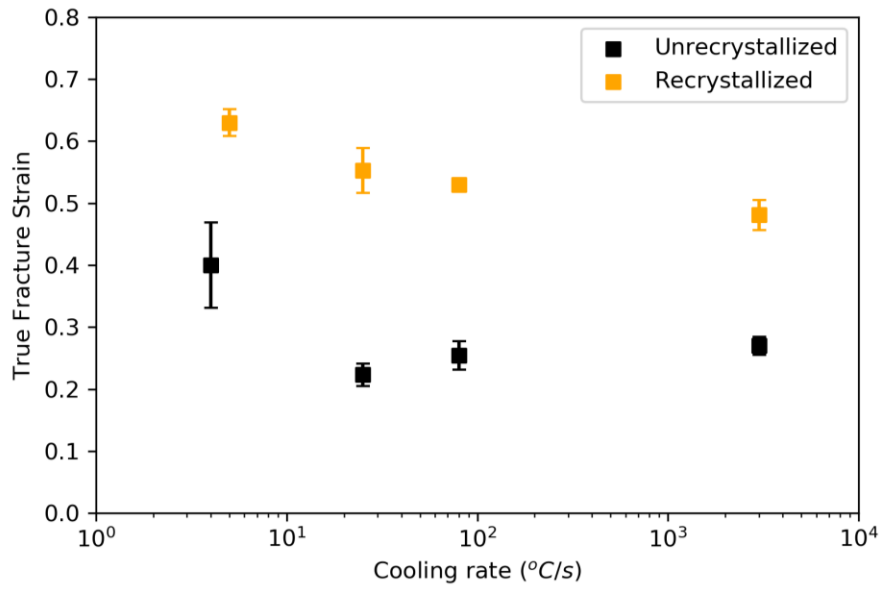
Table 5.7: Summary of change in mechanical properties from >2000 °C/s to 4-5 °C/s

Microstructure	Change in Yield Stress	Change in UTS
T4 Recrystallized	40 MPa	81 MPa
T4 Unrecrystallized	60 MPa	89 MPa
T6 Recrystallized	71 MPa	84 MPa
T6 Unrecrystallized	141 MPa	144 MPa

Turning to the fracture properties measured from the tensile tests, Figure 5.19 shows the variation of true fracture stress and true fracture strain with quench rate for T4 temper. It can be observed from Figure 5.19a that the true fracture stress is similar in magnitude for both the microstructures. However, Figure 5.19b shows that the true fracture strain shows a significant difference, with the recrystallized samples having true strain to fracture ≈ 2 times that of the unrecrystallized samples. With decreasing cooling rates, for the recrystallized microstructure, the true fracture strain increases from at ≈ 0.48 to ≈ 0.63 while the true fracture stress decreases from ≈ 433 MPa to ≈ 367 MPa. Figure 5.20 shows the variation of true fracture stress and true fracture strain with cooling rate for T6 temper. A more detailed discussion on the variation of true fracture strain with cooling rate will be provided in section 5.7 (fracture surfaces). In the T6 temper, for both the microstructures, the true fracture stress at 10 °C/s is observed to be the lowest among all cooling rates.

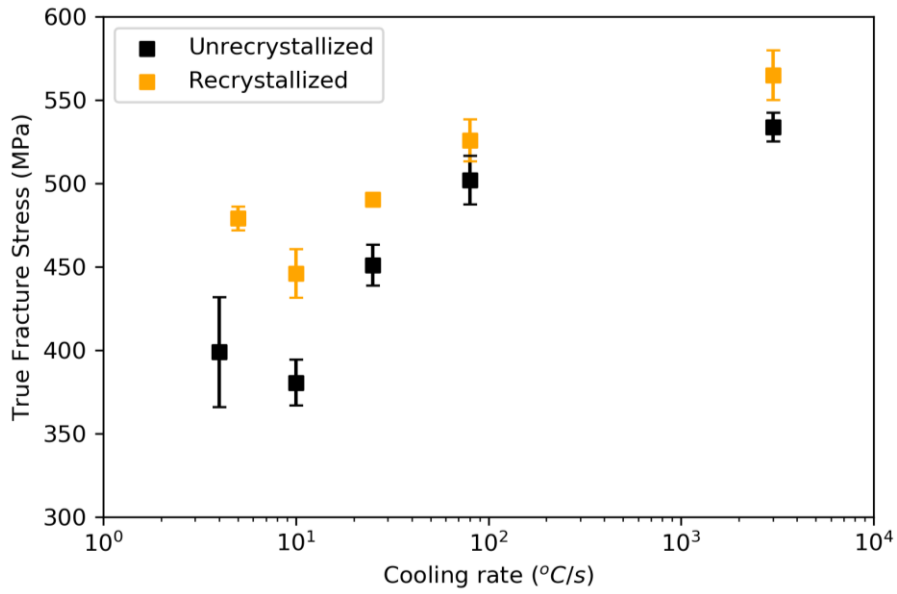


(a)

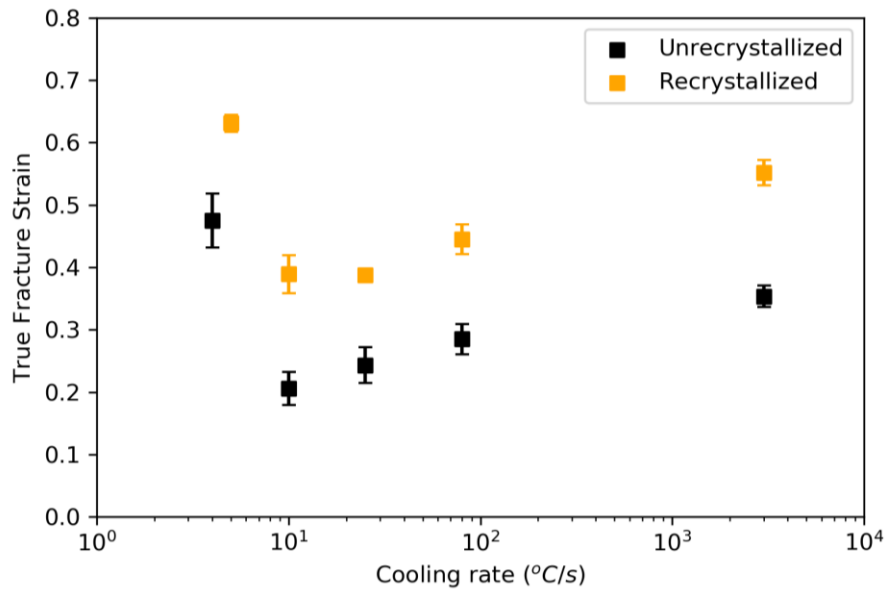


(b)

Figure 5.19: T4 temper (a) Variation of true fracture stress with cooling rate (b) Variation of true fracture strain with cooling rate



(a)



(b)

Figure 5.20: T6 temper (a) Variation of true fracture stress with cooling rate (b) Variation of true fracture strain with cooling rate

5.7 Fracture surfaces

5.7.1 Recrystallized alloys

SEM images of T4 and T6 fracture surfaces are shown in Appendices A and B, respectively. These fracture surfaces were used to characterize the material based on the mode of fracture, i.e., between transgranular and intergranular, as described in Section 4.9.4 of the methodology. For T4 tempered recrystallized alloys, no evidence for intergranular fracture was found, i.e., the fracture surfaces predominantly consisted of dimples under all cooling rates. However, for T6 tempered recrystallized alloys, the percentage of intergranular fracture varied with cooling rates, as shown in Table 5.8.

Table 5.8: Percentage of intergranular fracture, yield strengths and true fracture strains at different cooling rates for a T6 recrystallized microstructure

Cooling Rate	Yield Stress (MPa)	True fracture strain	% Intergranular
>2000 °C/s	329	0.55	0
80 °C/s	317	0.45	45
25 °C/s	306	0.39	90
10 °C/s	289	0.39	55
≈5 °C/s	258	0.63	0

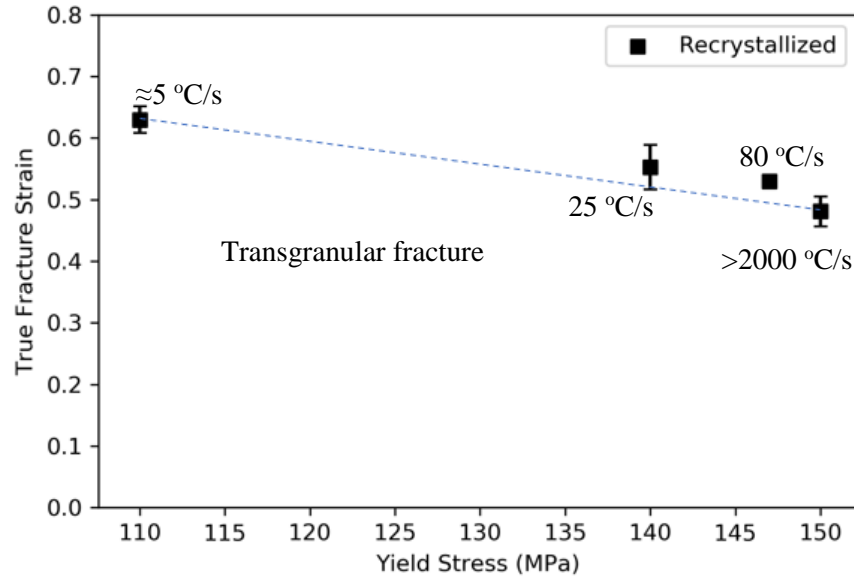


Figure 5.21: Variation of true fracture strain with yield stress for a T4 tempered recrystallized material

Figure 5.21 shows the variation of true fracture strain with cooling rates for a T4 recrystallized material. From Figure 5.21 it can be observed that the true fracture strain moderately increases with decreasing yield strength. Presence of dimples on the fracture surfaces suggests that the mode of fracture is predominantly transgranular.

Figure 5.22 shows the variation of true fracture strain with yield stress for the T6 material. From Table 5.8 it can be observed that as the cooling rate decreases from >2000 °C/s to 80 °C/s, the mode of fracture shifts from transgranular to a mixed mode (45% intergranular). With a further decrease in cooling rate (until 25 °C/s), the mode of fracture is predominantly intergranular (90% intergranular) and then the fraction intergranular decreases to 55% at 10 °C/s and goes to zero for a cooling rate of 5 °C/s.

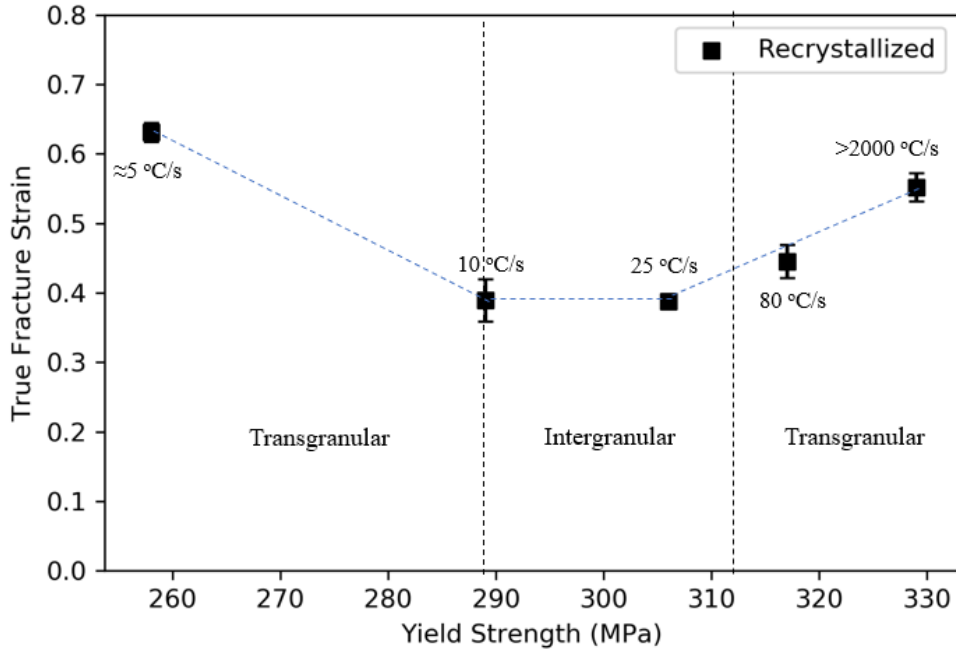
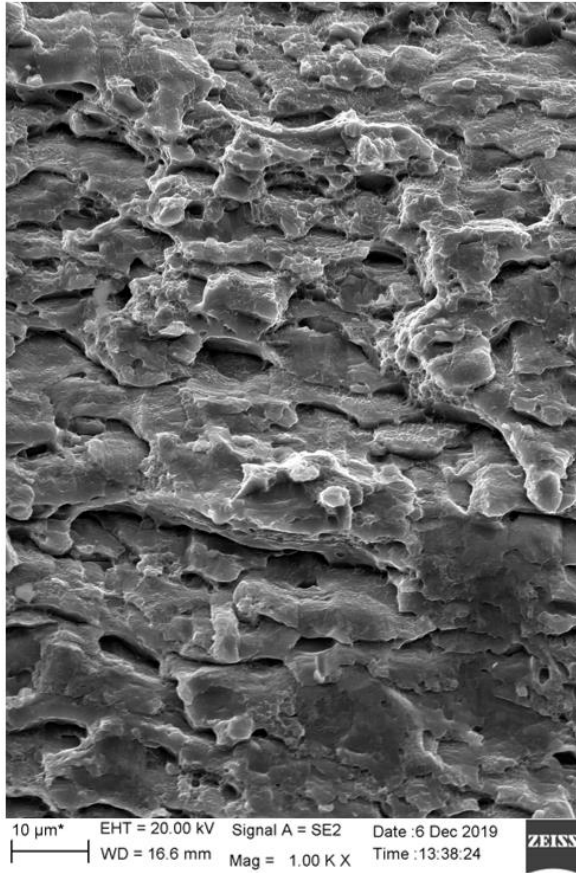


Figure 5.22: Variation of true fracture strain with yields stress for a T6 tempered recrystallized material

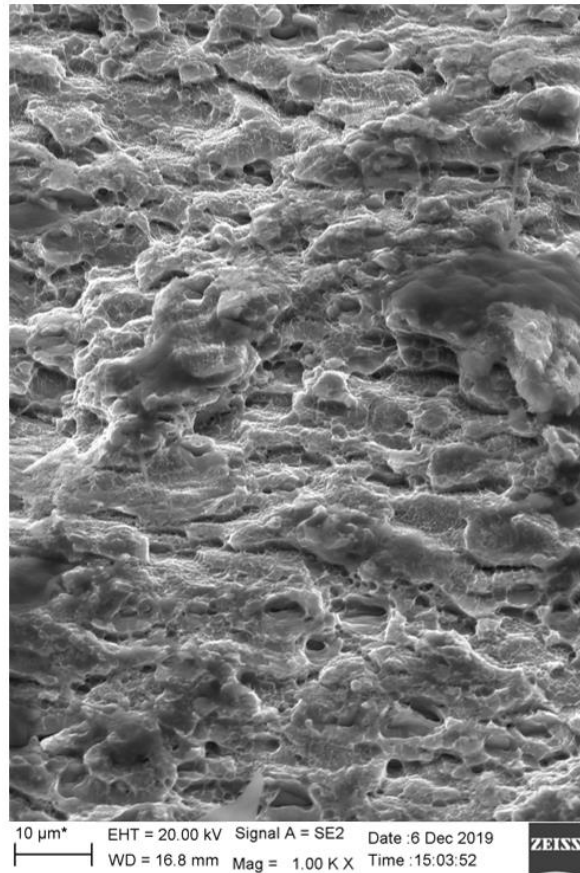
This suggests that the critical cooling rate (transition between the fracture modes) exists between 80 and 25 °C/s. As the cooling rate decreases from 10 to 5 °C/s, the true fracture strain increases, presumably due to the significant decrease in the yield strength.

5.7.2 Unrecrystallized alloys

The presence of sub-grains in the unrecrystallized microstructures make it difficult to characterize the fracture images as transgranular or intergranular. Figure 5.23a and 5.23b show high magnification fracture surface images of T6 tempered unrecrystallized microstructure cooled at >2000 °C/s and 10 °C/s, respectively. Evidence for splits in the grains can be observed, but it is difficult to characterize the overall fracture surface.



(a)



(b)

Figure 5.23: High magnification fracture surface images of unrecrystallized microstructure cooled at (a) >2000 °C/s and (b) 10 °C/s

Further investigation is required to examine the nature of fracture in unrecrystallized materials. Figure 5.24 and 5.25 show the variation of true fracture strain with yield stress at different cooling rates, for T4 and T6 tempered unrecrystallized microstructures. In the T4 condition, with decreasing cooling rates the true fracture strain remains constant until 25 °C/s, and then increases with further decrease in the cooling rate. On the other hand, in the T6 condition, the true strain to fracture decreases from 0.35 to 0.21 as the cooling rate decreases from >2000 to 10 °C/s. With a further decrease in the cooling rate to 4 °C/s, the true fracture strain increases to 0.48 .

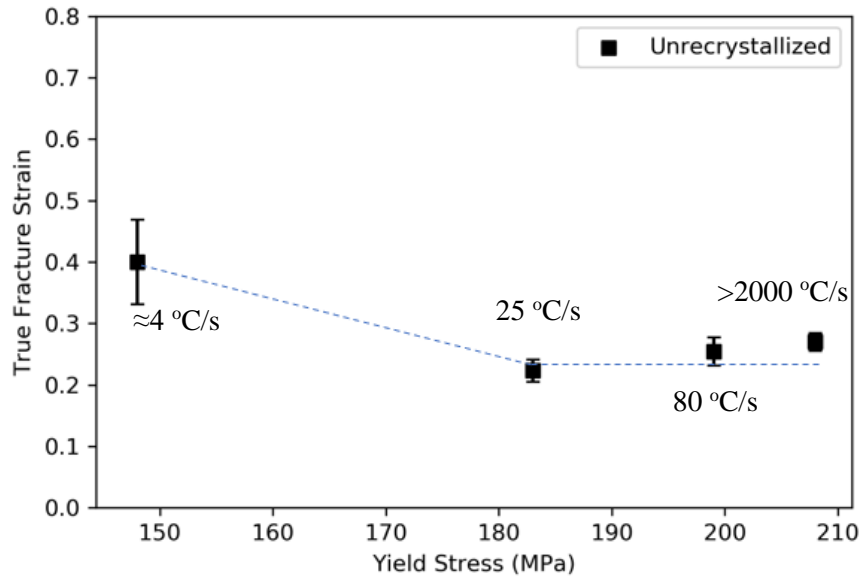


Figure 5.24: Variation of true fracture strain with yield stress for a T4 tempered unrecrystallized material

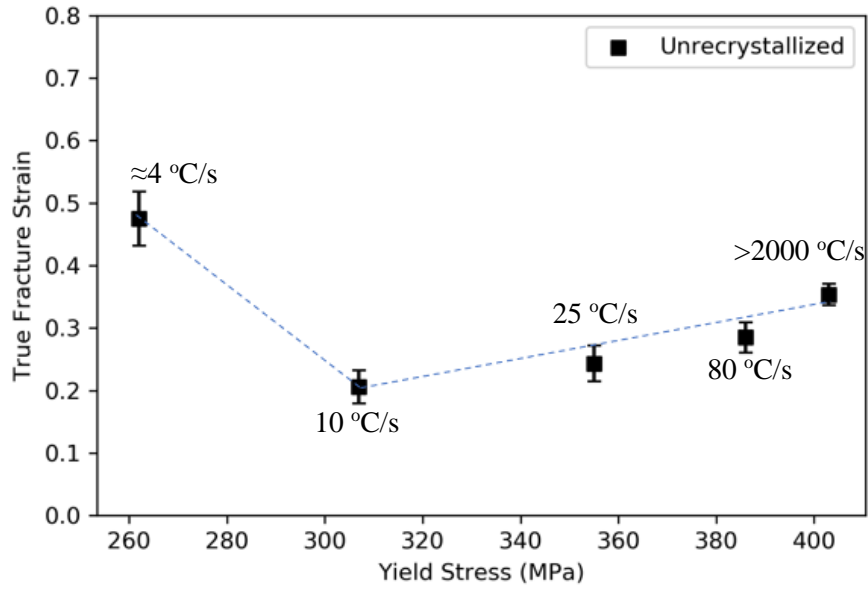


Figure 5.25: Variation of true fracture strain with yield stress for a T6 tempered unrecrystallized material

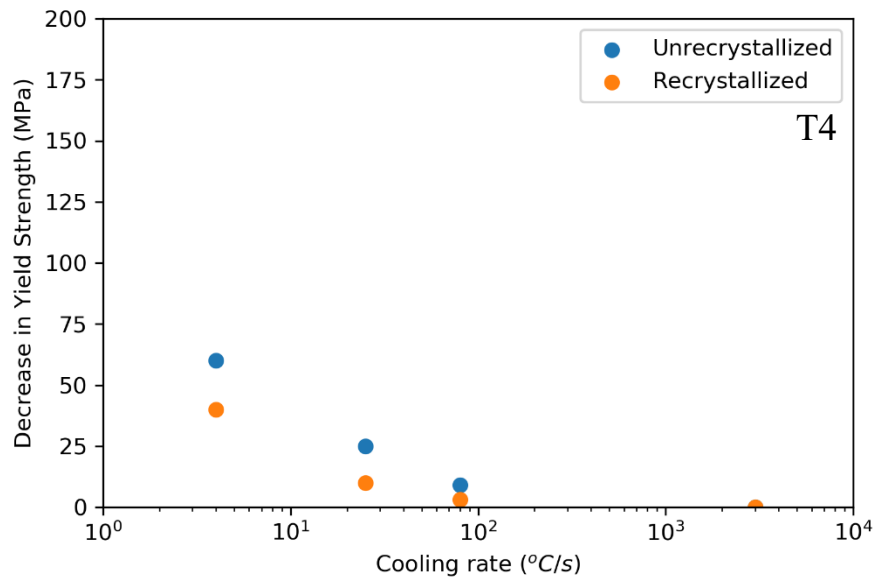
Chapter 6: Discussion

6.1 Mechanical properties

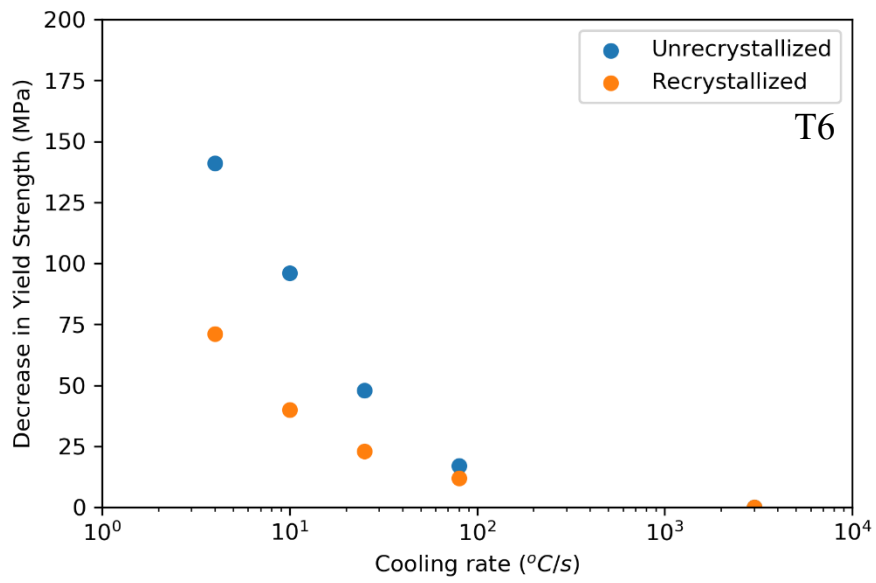
Based on the results from the modified Jominy end-quench tests and tensile tests, it was found that the mechanical properties such as hardness, yield stress and ultimate tensile stress increased with increasing cooling rates. Similar observations on the variation of hardness with cooling rates were reported by Chaudhury et. al. [88] for a Cu free AA6xxx cast alloy.

From the Jominy end-quench tests it was also observed that the magnitude of hardness for a fixed cooling rate is higher for the unrecrystallized microstructure than the recrystallized microstructure by $\approx 4 \text{ Kgf/mm}^2$. The difference in the magnitude of hardness is small due to the absence of ageing (hardness values were measured within 10 minutes after quenching) and should reflect the contribution from the residual deformed microstructure.

The decrease in yield strength with respect to water quenched condition is shown in Figure 6.1a for T4 temper and Figure 6.1b for T6 temper. Similar to hardness, the yield strength was also found to decrease with decreasing cooling rates. In T4 temper the drop in yield strength is presumed to be associated with the loss of solute atoms (Mg, Si and Cu) and vacancies during cooling. These solute atoms lost during the quench are then not available to form hardening clusters during natural ageing. Since more solutes and vacancies are lost at lower cooling rates, the yield strength is correspondingly lower at these cooling rates. This would be consistent with the SEM micrographs (Figures 5.9 and 5.11) shown in Chapter 5 that showed a higher size and number density of grain boundary precipitates at lower cooling rates.



(a)



(b)

Figure 6.1: Decrease in yield strength with respect to the water quenched condition, versus cooling rates for a recrystallized and unrecrystallized microstructure; (a) T4 and (b) T6 tempered

Figure 6.1a also shows that the magnitude of drop in yield strength for the T4 temper is higher for the unrecrystallized alloy than in the recrystallized alloy. This suggests that the unrecrystallized grain structure is more quench sensitive than the recrystallized microstructure. This may be due to the presence of higher density of heterogeneous nucleation sites (low and high angle grain boundaries) for the nucleation of precipitates in the unrecrystallized microstructure.

In T6 temper, formation of β'' and Q/Q' phase acts as the main strengthening mechanism [52]. Loss of solutes at lower quench rates during cooling reduces the availability of solutes to form these phases during ageing. This results in a lower yield strength at reduced cooling rates as shown in Figure 6.1b. Further, with increasing cooling rates, the difference in the yield strengths between the unrecrystallized and the recrystallized grain structure gradually increases. This is also consistent with the presence of higher density of heterogeneous nucleation sites in the unrecrystallized microstructure.

6.1.1 Fracture

Figure 6.2 summarizes the relationship between true fracture strain and yield stress for recrystallized and unrecrystallized microstructures at various cooling rates. For all the conditions apart from T4 recrystallized, it can be observed that the true fracture strain initially decreases with decrease in yield strength, and significantly increases with further decrease in yield strength. The initial decrease in the true fracture strain can be attributed to the increased propensity for damage (void nucleation, growth, and coalescence) on grain boundaries due to the formation of grain boundary precipitates. This favors intergranular fracture.

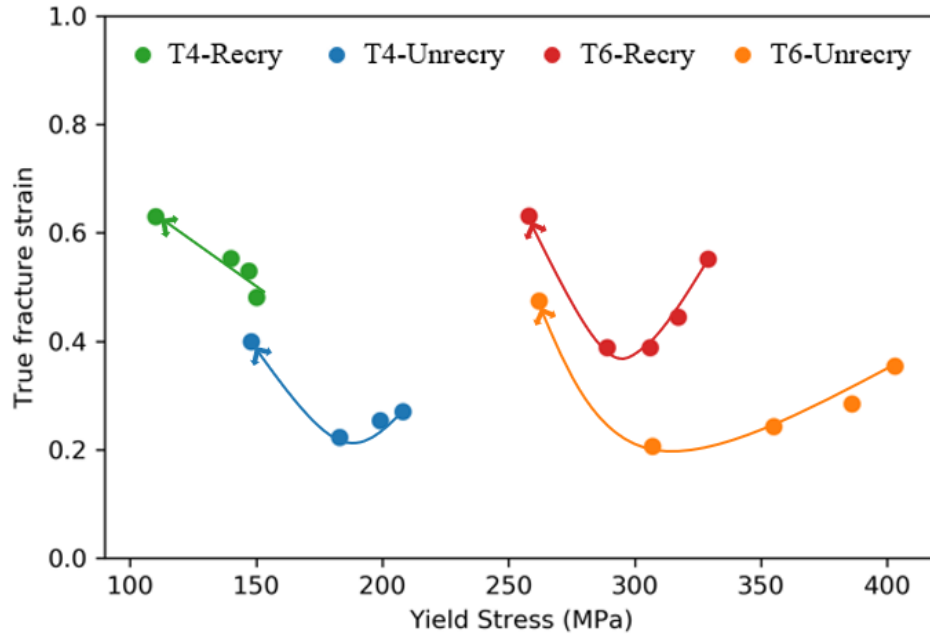
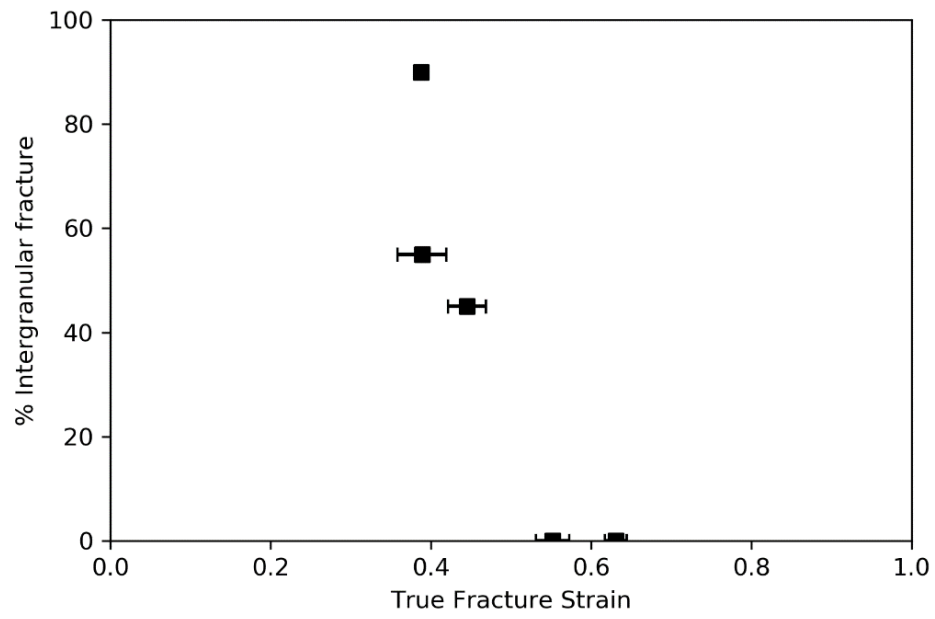
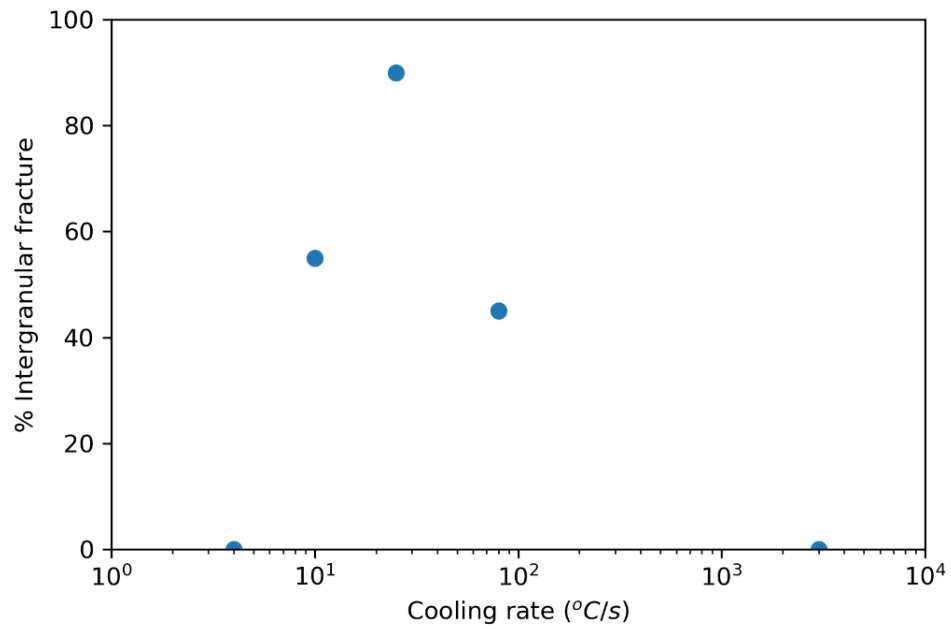


Figure 6.2: Variation of true fracture strain with yield stress. Note: arrows indicate decreasing cooling rates

A similar observation on the loss of true fracture strain due to the occurrence of intergranular fracture was reported by Poole et. al. [35]. The subsequent increase in the true fracture strain can be attributed to the significant drop in the yield stress. Evensen et. al. [72] suggested that the intergranular fracture can occur if the boundaries reach a local critical stress, i.e., the critical stress to nucleate voids at particles on the grain boundary. It is likely that the drop in yield stress leads to a lower stress on the boundaries reaching values below the critical stress, avoiding the damage on the grain boundary and intergranular fracture. In the T4 recrystallized condition, the true fracture strain increases with decrease in yield strength. It is once again assumed that the stresses in the boundaries do not reach the critical stress required for the occurrence of intergranular fracture (transgranular fracture was observed in all cases). Figure 6.3a and 6.3b show the variation of percentage of intergranular fracture with true fracture strain and cooling rates respectively, for a T6 recrystallized microstructure.



(a)



(b)

Figure 6.3: Variation of percentage of intergranular fracture for a T6 recrystallized microstructure with (a) true fracture strain and (b) cooling rate

From Figure 6.3a, it can be observed that the magnitude of true fracture strain is higher in the absence of intergranular fracture. From Figure 6.3b, it can be noted that with an initial decrease in the cooling rates the percentage of intergranular fracture increases. With further decrease in cooling rates, the percentage of intergranular fracture decreases. This suggests a transition in the mode of fracture, from intergranular to transgranular type of fracture. This also suggests a presence of two competing mechanisms:

1. With decreasing cooling rates, both the width of the precipitate free zones (PFZs) and the number of grain boundary precipitates increases. Localization of strain occurs in the soft PFZs that promote the formation of microvoids at the grain boundary precipitates [73]. This increases the propensity of the occurrence of intergranular fracture with decreasing cooling rates
2. With a decrease in cooling rates, the yield stress decreases. This leads to a decrease in the stresses at the boundaries. If the stress drops below a local critical stress, the propensity of the occurrence of intergranular fracture decreases

It is therefore important to understand the localization of strain within the PFZs in the grain boundaries. Section 6.2 will show the results for simulations of localization of strain in the PFZs using a polycrystal plasticity model.

6.2 Polycrystal plasticity

This section summarizes the results of the polycrystal plasticity simulations that were developed to examine the local stress and strain distribution of an aluminum alloy with precipitate free zones (PFZs) at the grain boundaries. The results include observations on the localization of strain in the PFZ, and on the effect of the strength of the PFZs relative to the grain interior and width of the PFZs on the local strain components. The details of the model were outlined in Chapter 4.

Figure 6.4 shows the simulated stress-strain response of the initial microstructure subjected to a uniaxial tensile load, where the green and blue dashed lines represent the constitutive behavior assumed for the material in the PFZ and the grain interior, respectively.

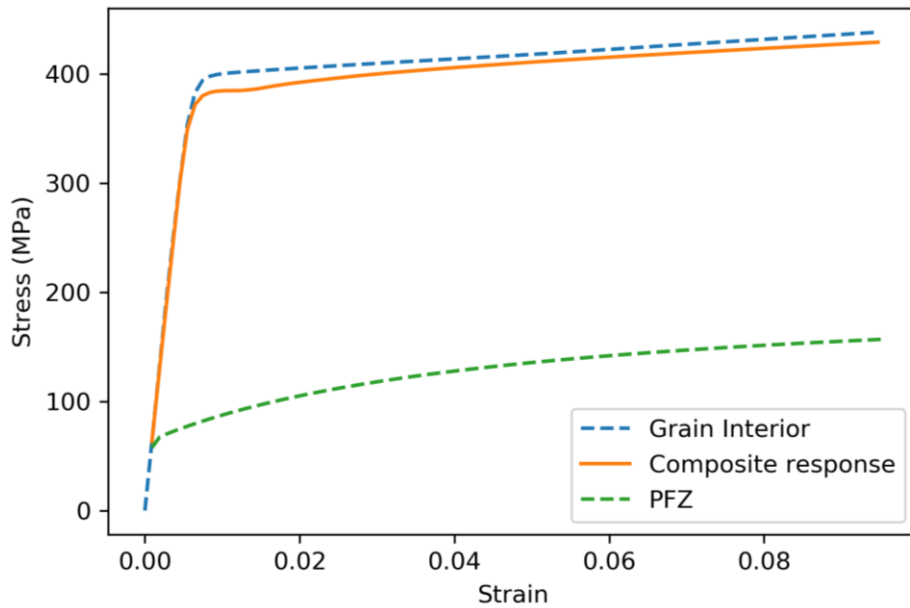


Figure 6.4: Macroscopic tensile curve of the initial microstructure with the presence of PFZs

From Figure 6.4, it can be observed that the presence of PFZ in the microstructure does not significantly affect the macroscopic tensile properties, only decreasing the yield stress by 5% and the flow stress at a strain of 0.05 by 1.67%.

6.2.1 Observations on strain localization when PFZs are parallel and at 60° to the loading axis

Figure 6.5 shows a contour plot of the normalized strain for a microstructure where the ratio of length of one side of the hexagonal grain, a , to PFZ width was 85. For a material with a grain size of $40\mu\text{m}$, this corresponds to a PFZ width of $\approx 350\text{nm}$, which is similar to observations of Mansouri [83] on a non-copper containing alloy. The normalized strain is defined as the ratio of von Mises equivalent strain to the far-field strain.

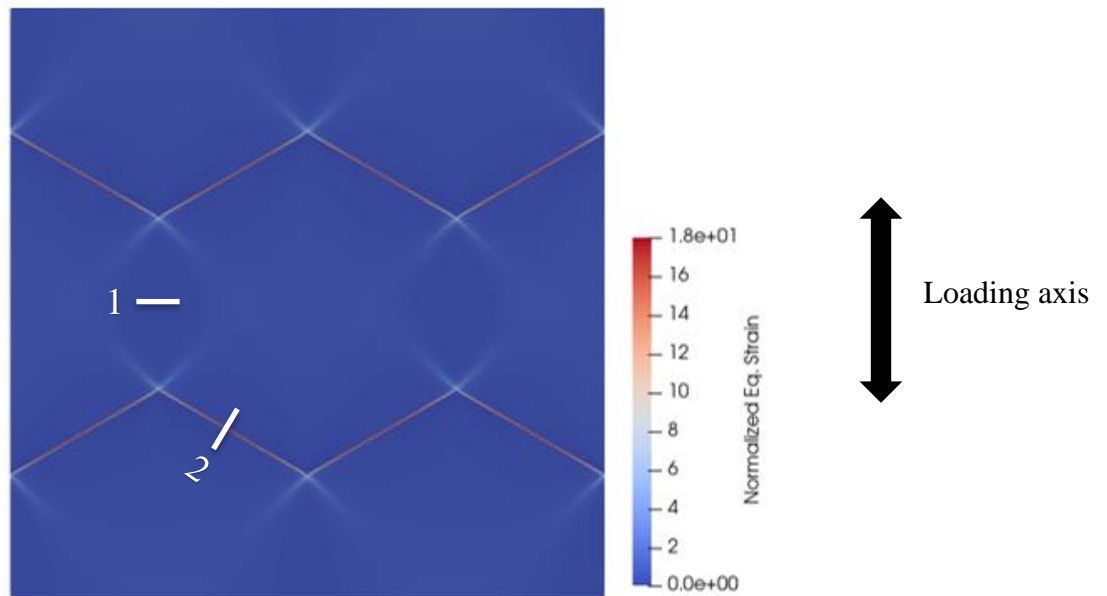


Figure 6.5: Contour plot of the normalized strain for $a/h = 85$ with a uniaxial tensile load parallel to the grain boundary

From Figure 6.5 it can be observed that the magnitude of normalized strain is significantly higher in the PFZ of boundaries that are oriented at 60° with respect to the loading axis. However, for PFZs of grain boundaries parallel to the loading axis, there appears to be little localization of plastic deformation.

To examine the localization of strain in the PFZs, the variation of the normalized strain ($\epsilon_{eq}/\epsilon_{far-field}$) was plotted along lines 1 and 2 (as shown in Figure 6.5). The far field strain is calculated by averaging the magnitude of strain across the lines, extended to the entire microstructure. Figures 6.6a and 6.6b show this variation for the PFZ parallel to loading axis and at 60° to the loading axis, respectively.

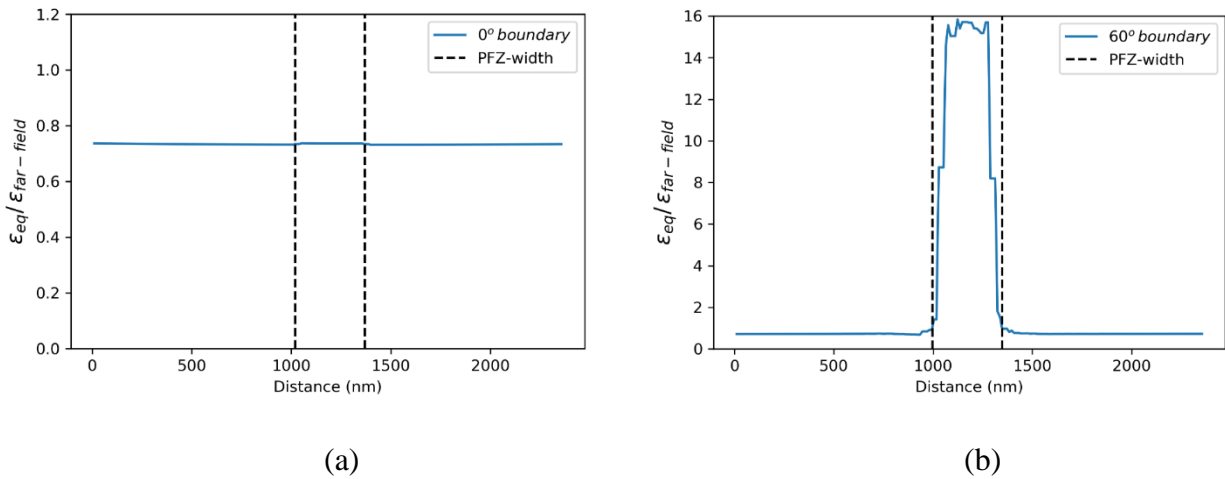


Figure 6.6: Magnitude of normalized strain along (a) line 1 (0° boundary) and (b) line 2 (60° boundary)

It can be observed that for the PFZ parallel to the loading axis, there is no localization of strain in the PFZ (note: this overall value has a normalized strain less than unity and although not shown, the normalized strain in the grain interior is slightly greater than unity). In contrast, Figure 6.6b

shows that the simulations predict a strain localization of ≈ 16 times the far field equivalent strain and that the area where localization occurs corresponds to the PFZ.

6.2.1.1 Effect of far-field strain

The evolution of the magnitude of the localization was examined for different far field strains in Figure 6.7. It can be observed that the magnitude of the equivalent strain at the PFZ decreases with increasing strain.

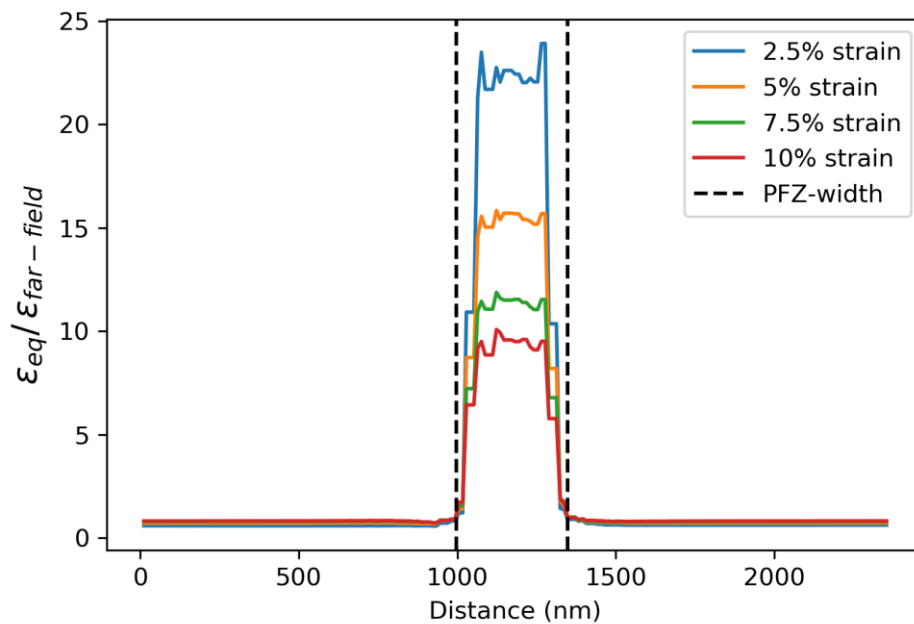


Figure 6.7: Evolution of normalized strain at the 60° boundary for a microstructure with the loading axis parallel to the grain boundary

At a far-field applied strain of 2.5%, the equivalent strain in the PFZ is ≈ 23 times the far-field strain. The magnitude decreases to ≈ 16 times the far-field strain at 5% strain, ≈ 11 time at 7.5% and ≈ 9 times at 10%. It should be noted that all the results henceforth will be shown at a strain of 5%.

6.2.1.2 Shear and normal strains in the coordinate system of the grain boundary

To further understand the contributions of different components of strain, ϵ_{xx} (parallel to the 60° grain boundary), ϵ_{yy} (out-of-plane strain), ϵ_{zz} (perpendicular to the 60° boundary) and shear strain ϵ_{xz} were plotted along line 2 as shown in Figure 6.8. The details of coordinate transformations were outlined in Section 4.10.5.

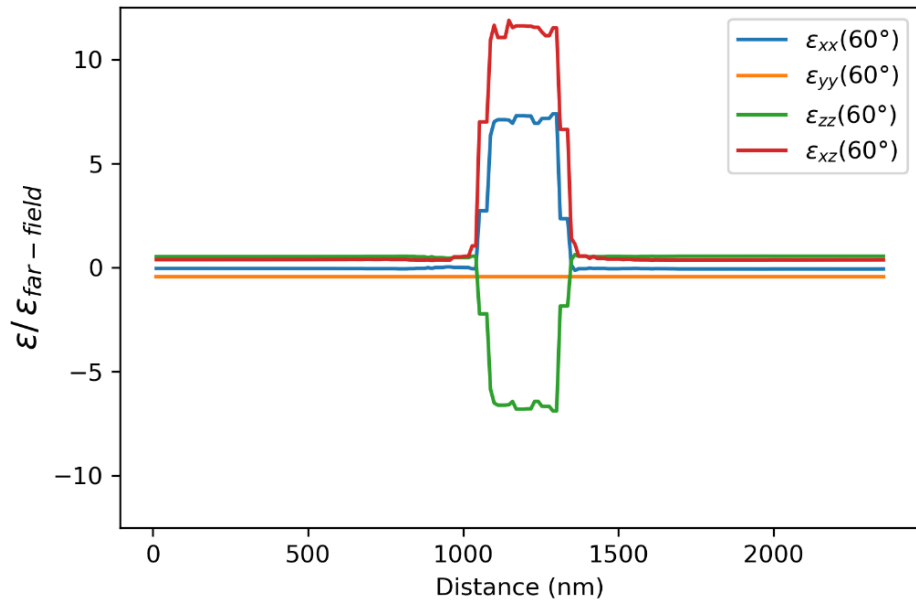


Figure 6.8: Magnitude of normalized strain components along the 60° boundary, far-field strain of 5%

From Figure 6.8, it can be observed that shearing on the PFZs has the highest contribution to the localization. The magnitude of shear strain parallel to the boundary is ≈ 12 times the far-field strain. The next largest contribution is from the strain parallel to the boundary, which is ≈ 7 times the far-field strain. It can also be observed that the strain component perpendicular to the boundary is \approx similar in magnitude of ϵ_{xx} , but opposite in direction, consistent with nearly plane strain deformation.

6.2.1.3 Distribution of hydrostatic stress

Turning to the stress distribution, Figure 6.9 shows a contour plot of the hydrostatic stress on the 0° and 60° boundary for a microstructure with $a/h = 85$.

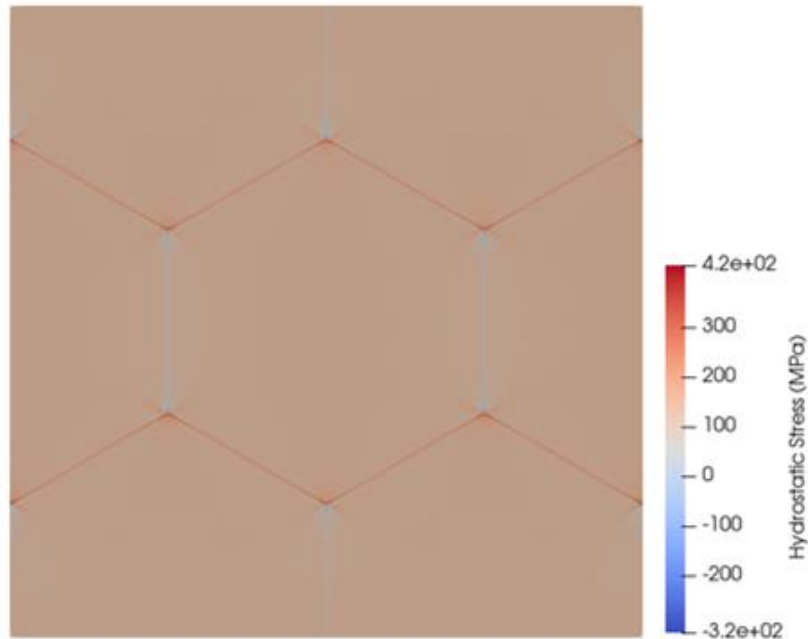


Figure 6.9: Contour plot of the hydrostatic stress for $a/h = 85$ with a uniaxial tensile load parallel to the grain boundary, far-field strain of 5%

From Figure 6.9, it can be observed that the maximum positive hydrostatic stress is observed near the grain boundary triple junctions. The boundaries oriented parallel to the loading direction have the least amount of hydrostatic stress. The role of hydrostatic stress could be a consideration for damage nucleation and growth and is an area for future work.

6.2.1.4 Effect of the ratio of flow stress in PFZ to grain interior

Figure 6.10 shows the effect of the relative flow stress of the PFZ to the grain interior on the localization of strain. In these simulations, the strength of the grain interior was kept constant

while the yield stress of the material in the PFZ was varied. The ratio given in Figure 6.10 is the ratio of the strength of the grain interior to that of the PFZ. It can be observed that with increasing differences in the strengths between the interior and the PFZ, the magnitude of strain localization on the boundary increases.

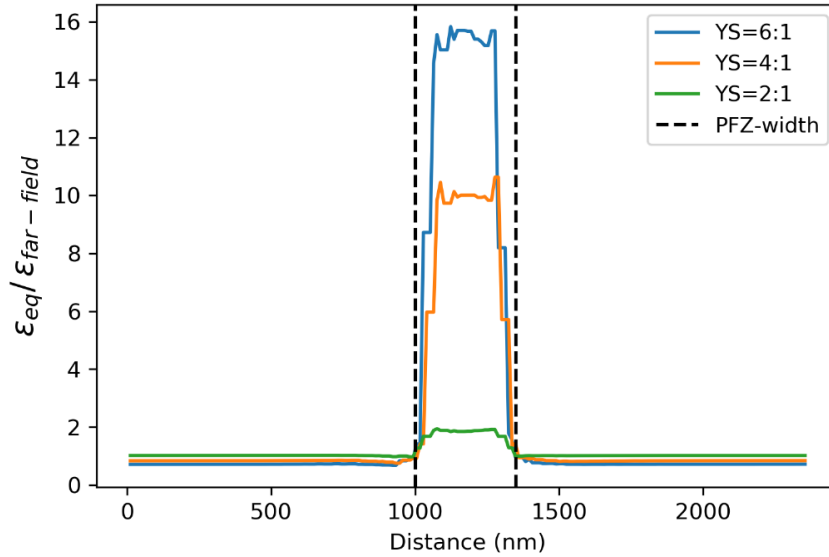


Figure 6.10: Magnitude of normalized strain across the 60° boundary (line 2) with varying PFZ strengths at far-field strains of 5%

6.2.1.5 Effect of PFZ width

The results for the effect of normalized PFZ width for $a/h = 85$ and $a/h = 45$, on localization are shown in Figure 6.11, for a loading direction of 60° with respect to the PFZ. It can be observed that with increasing PFZ width, the magnitude of strain localization on the boundary decreases. The evolution of strain localization in the PFZ, with varying widths of PFZs is shown in Figure 6.12. As the strain evolves from 5% (Figure 6.12a) to 7.5% (Figure 6.12b), it can be observed that the decrease in the magnitudes of strain amplification is higher for the microstructure with $a/h = 85$.

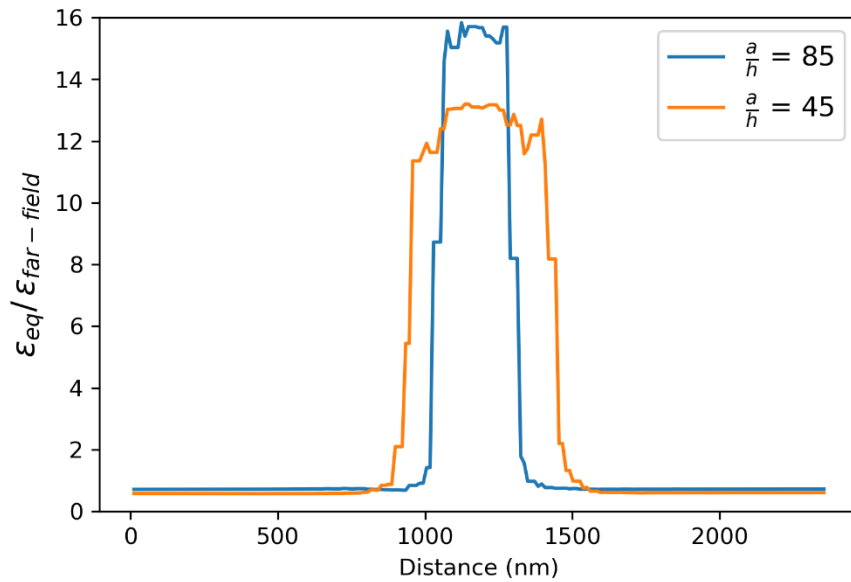


Figure 6.11: Magnitude of normalized strain on the 60° boundary (line 2) for a microstructure with $a/h = 85$ and $a/h = 45$

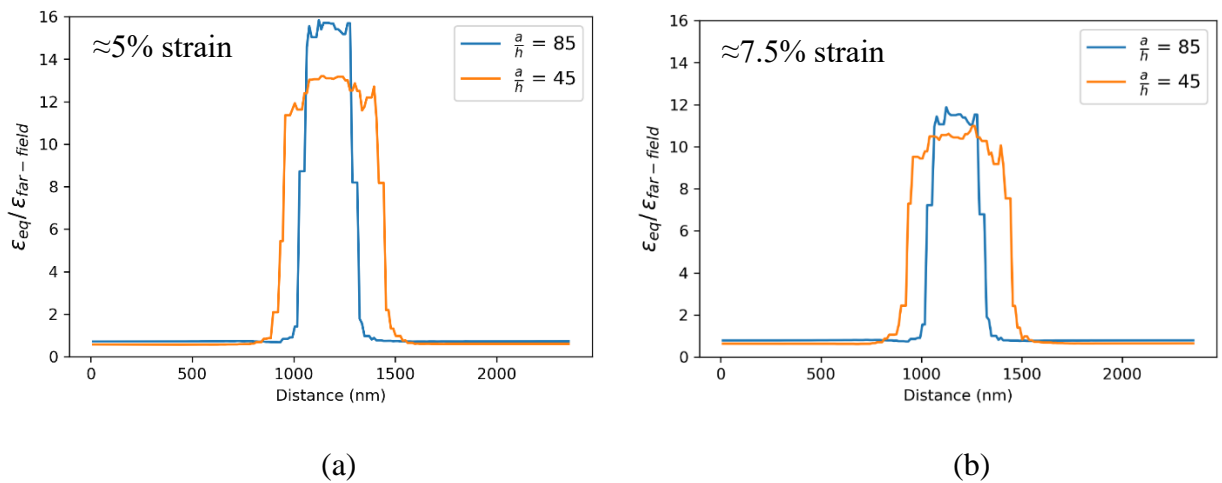


Figure 6.12: Magnitude of normalized strain on the 60° boundary (line 2) for microstructures with $a/h = 85$ and $a/h = 45$ at (a) 5% strain and (b) 7.5% strain

6.2.2 Observations on strain localization when PFZs are perpendicular and at 30° to the loading axis

Figure 6.13 shows a contour plot of the normalized strain for the simulation cell. It can be observed that the normalized strain is higher on the PFZ oriented at 30° to the loading axis compared to the PFZ perpendicular to the loading axis. The variation of normalized strain along line 3 and line 4, as indicated in Figure 6.13, are shown in Figure 6.14. The magnitude of equivalent strain in the 30° PFZ reaches to ≈ 8 times the far-field strain, which is $\approx 50\%$ less compared to the 60° PFZ shown in section 6.2.1. The strains in the PFZs perpendicular to the loading axis is essentially equal to the far field strain.

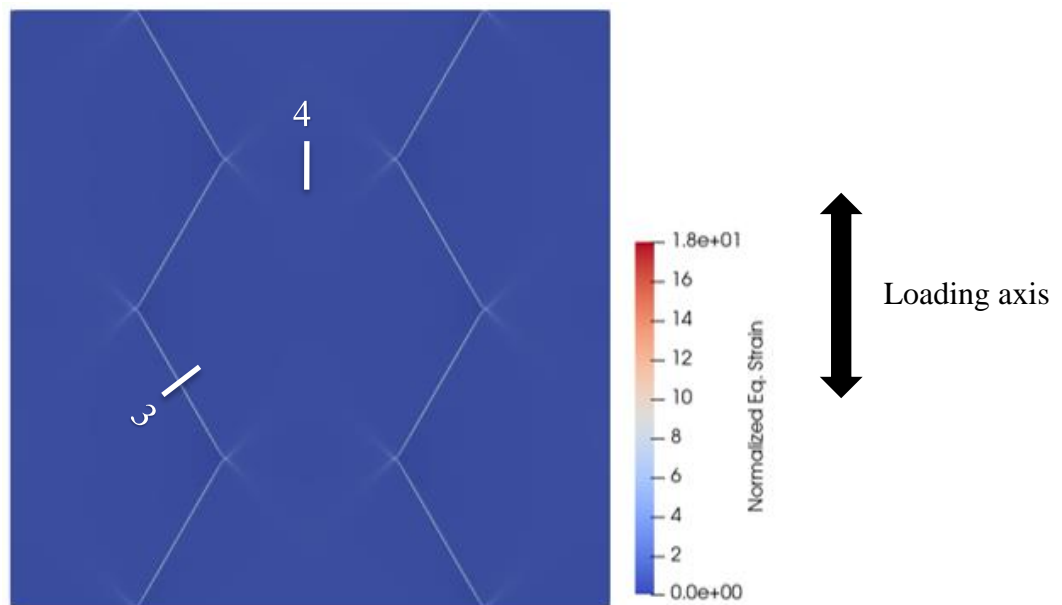


Figure 6.13: Contour plot of the normalized strain for $a/h = 85$ with a uniaxial tensile load perpendicular to the grain boundary

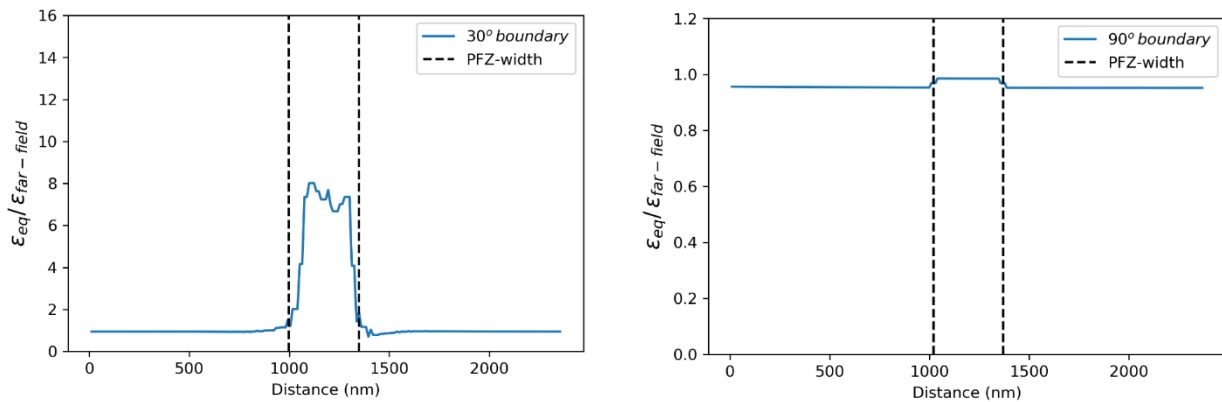


Figure 6.14: Magnitude of normalized strain along (a) line 3 (30° boundary) and (b) line 4 (90° boundary)

6.2.2.1 Shear and normal strains in the coordinate system of the grain boundary

Figure 6.15 shows the contributions of the normalized strain components, ϵ_{xx} (parallel to the 30° grain boundary), ϵ_{yy} (out-of-plane strain), ϵ_{zz} (perpendicular to the 30° boundary) and shear strain ϵ_{xz} along line 3.

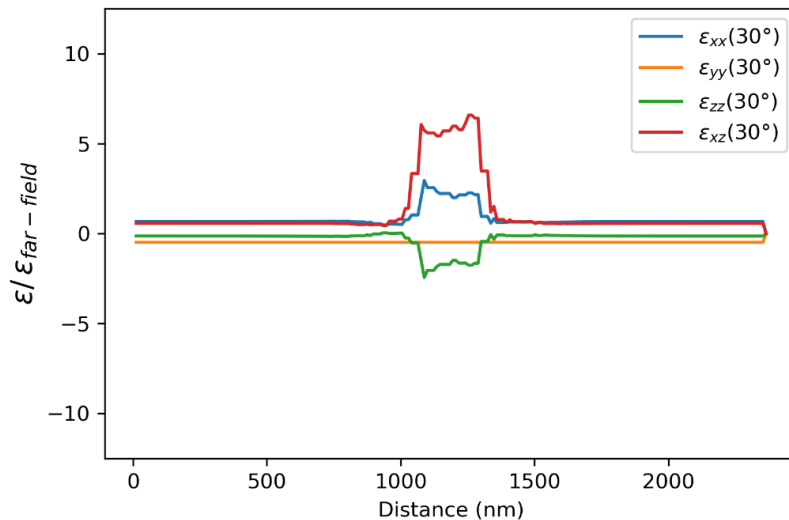


Figure 6.15: Magnitude of normalized strain components along the 30° boundary

Similar to the 60° boundary, shearing parallel to the boundary has the largest contribution to localization. The magnitude of the shear strain on the 30° boundary is ≈ 5 times the far-field strain. Once again, the strain perpendicular to the boundary is equal and opposite in direction to the strain parallel to the boundary.

6.2.2.2 Distribution of hydrostatic stress

Figure 6.16 shows a contour plot of the hydrostatic stress on the 30° and 90° boundary. It can be observed that the maximum hydrostatic stress is on the boundary oriented normally to the loading direction. The boundaries located obliquely to the loading axis have significant shearing which relaxes the component of hydrostatic stress. These results are consistent with the finite element observations made by Khadyko et. al. [78].

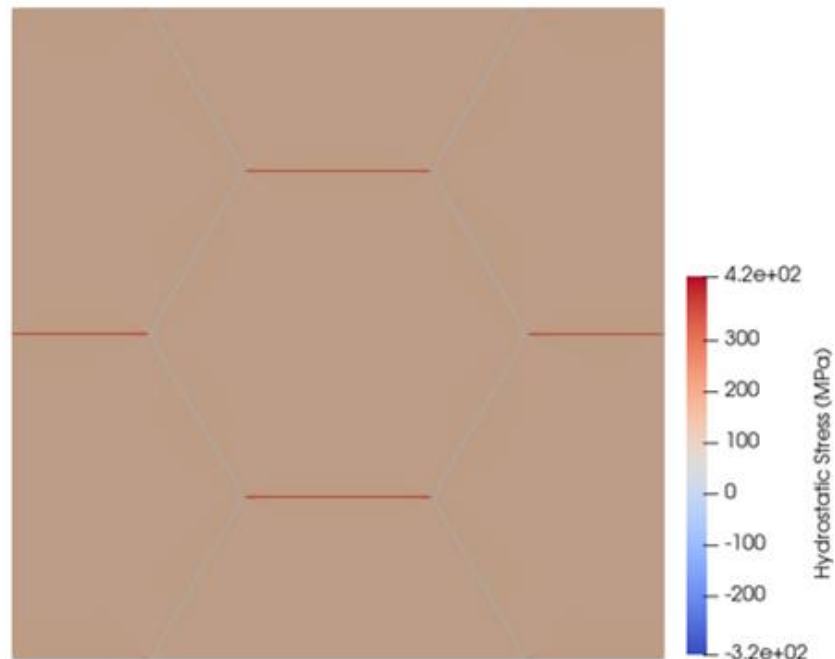


Figure 6.16: Contour plot of the hydrostatic stress for $a/h = 85$ with a uniaxial tensile load perpendicular to the grain boundary

6.3 Effect of copper

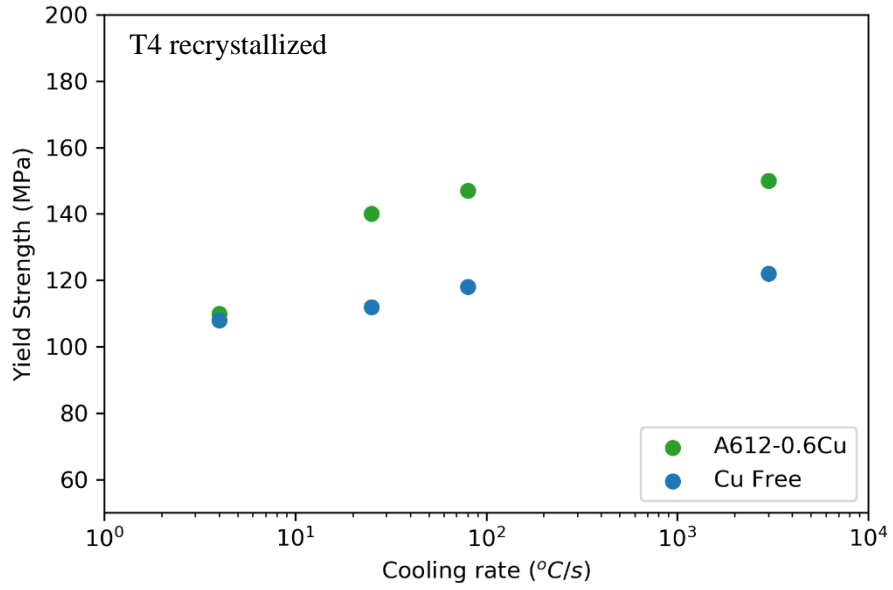
This section compares the effect of cooling rates on the mechanical behavior of Cu free alloys with alloys containing 0.6 wt.% Cu. The results for the copper free alloys were taken from the work of Sarmady [60], who followed a similar procedure on the Cu free version of the current alloy. The differences in the tensile properties is due to the formation of different precipitates that nucleate and grow during cooling, and aging treatments, i.e., β'/β vs Q'/Q .

T4 temper

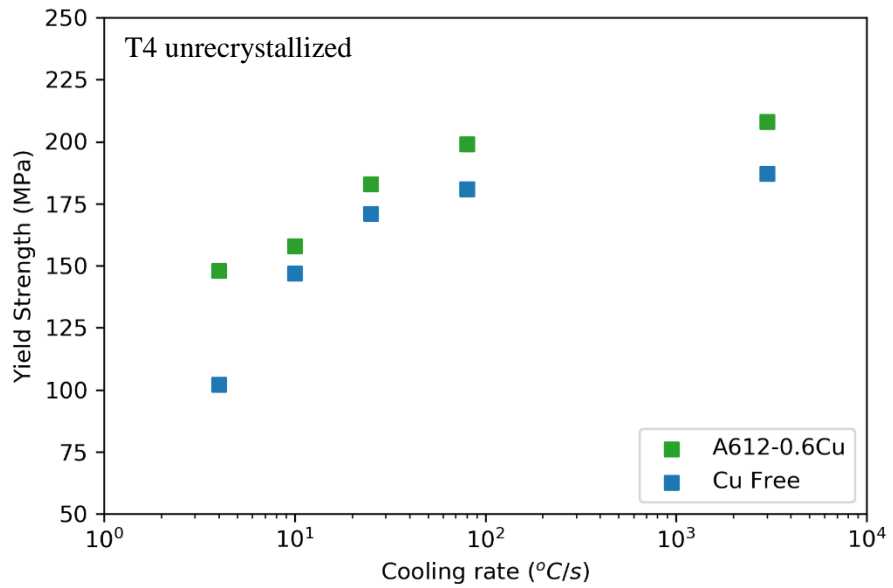
Figures 6.17a and 6.17b show the variation of 0.2% offset yield strength with cooling rate at T4 temper for recrystallized and unrecrystallized samples respectively. For the Cu free recrystallized microstructure, it can be observed that the yield strength drops from ≈ 122 MPa to ≈ 108 MPa (a difference of 14 MPa) with decreasing cooling rate, while the yield stress drops from ≈ 150 MPa to ≈ 110 MPa (a difference of 40 MPa) for Cu containing recrystallized microstructure. On the other hand, for Cu free unrecrystallized microstructure, the yield stress drops from ≈ 187 MPa to ≈ 102 MPa (a difference of 85 MPa), while it drops from ≈ 208 MPa to ≈ 148 MPa (a difference of 60 MPa) for Cu containing unrecrystallized microstructure.

T6 temper

Figure 6.18a and 6.18b show the variation of 0.2% yield strength with cooling rate at T6 temper for recrystallized and unrecrystallized alloys respectively. For Cu free recrystallized microstructure, it can be observed that the yield stress decreases from ≈ 334 MPa to ≈ 271 MPa (a difference of 63 MPa) with decreasing cooling rate, while the yields stress drops from ≈ 329 MPa

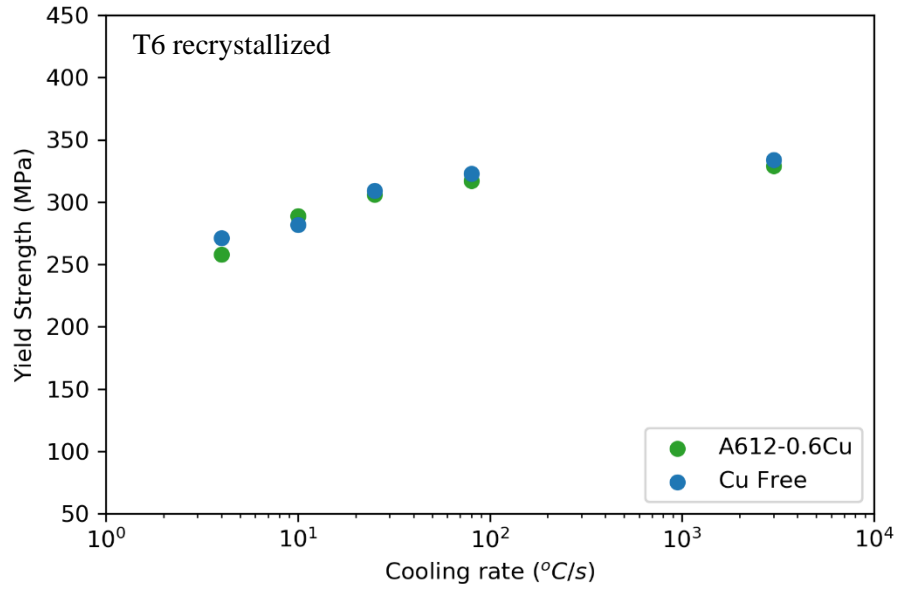


(a)

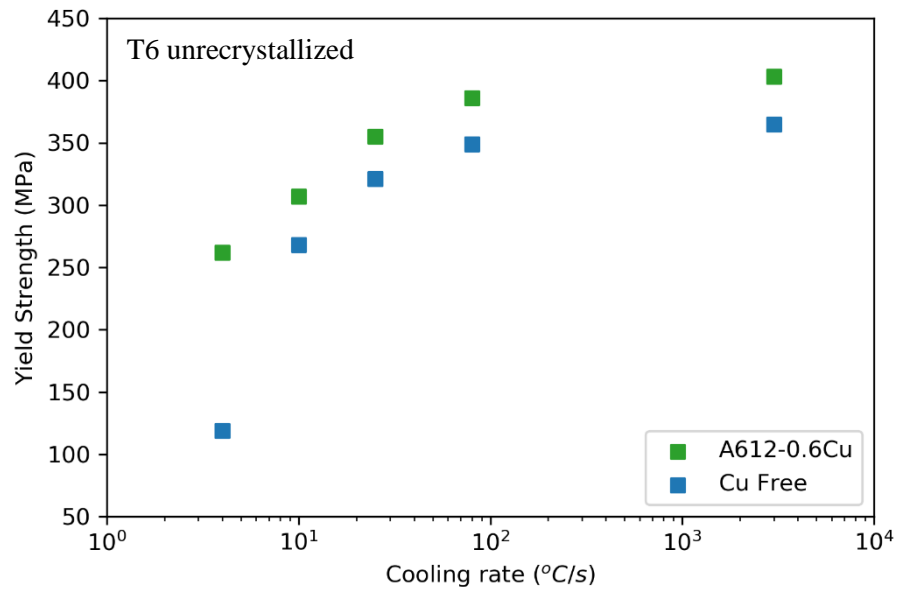


(b)

Figure 6.17: Variation of yield stress with cooling rate for alloys with and without Cu at T4 temper for (a) recrystallized microstructure and (b) unrecrystallized microstructure



(a)



(b)

Figure 6.18: Variation of yield stress with cooling rate for alloys with and without Cu at T6 temper for (a) recrystallized microstructure and (b) unrecrystallized microstructure

to ≈ 258 MPa (a difference of 81 MPa) for Cu containing recrystallized microstructure. On the other hand, for Cu free unrecrystallized microstructure, the yield stress drops from ≈ 365 MPa to ≈ 119 MPa (a difference of 246 MPa), while it drops from ≈ 403 MPa to ≈ 262 MPa difference of 141 MPa) for Cu containing unrecrystallized microstructure.

From Figures 6.17 and 6.18, it can be seen that the presence of Cu makes the unrecrystallized microstructure less quench sensitive, and on the other hand, the recrystallized alloys are more quench sensitive when they contain 0.6 wt.% Cu. The differences in the behavior of the two alloys is speculated to be due to the unique nucleation characteristics of the precipitates on the heterogeneous nucleation sites. A more accurate explanation would require further investigation (e.g. TEM analysis) on the nature of precipitates, and the fracture process.

Chapter 7: Summary and recommendations for future work

7.1 Summary

The aim of this work was to investigate the quench sensitivity of an AA6xxx alloy with 0.6 wt.% Cu for two initial microstructures. The key results are summarized as follows:

- (a) The as-received microstructure was characterized using EBSD. It was found that a solution treatment of 5 minutes at 550 °C did not cause significant recrystallization in the material
- (b) A process route was developed to produce a recrystallized microstructure. The initial material was cold rolled to $\approx 19\%$, and a recrystallized grain with a major axis size of $\approx 43\ \mu\text{m}$ and a minor axis size of $\approx 14\ \mu\text{m}$ was obtained after the solution treatment
- (c) From the modified Jominy end-quench tests, it was found that the hardness for both the initial microstructures decreased with decreasing cooling rates. This was rationalized based on the precipitation of non-hardening precipitates during slow cooling which was consistent with the FEGSEM micrographs
- (d) Gleeble 3500 thermomechanical simulator was used to obtain intermediate cooling rates of 10 °C/s, 25 °C/s and 80 °C/s. These samples were subsequently subjected to ageing either at room temperature (T4) or at 180 °C for 4 hours (T6). Tensile tests were then conducted on these samples to study the variation of yield stress, ultimate tensile stress (UTS), true fracture strain and true fracture stress with the cooling rates
- (e) Both yield stress and UTS was found to decrease with decreasing quench rates. Variation of true fracture strains and true fracture stresses, however, was more complicated. It was also found that the unrecrystallized grain structure was more quench sensitive than the

recrystallized structure, which was speculated to be due to the presence of higher density of heterogeneous nucleation sites in the unrecrystallized structure

- (f) The effect of Cu on quench sensitivity was complex: quench sensitivity in the unrecrystallized microstructure decreased in the presence of Cu, while the sensitivity increased in the recrystallized alloys
- (g) For a T6 recrystallized microstructure, a transition between transgranular and intergranular fracture was observed with decreasing cooling rates. This was attributed to the increase in the number of grain boundary precipitates, with decreasing cooling rates, which increases the number of nucleation sites for intergranular fracture
- (h) From the polycrystal plasticity model, strain localization was observed on boundaries oriented at different angles w.r.t the loading axis, for a 2-D hexagonal microstructure. Among the 0° , 30° , 60° and 90° boundaries, it was found that the localization was highest in the boundaries oriented 60° to the loading axis

7.2 Recommendations for future work

- a) Conducting additional Gleeble tests on both the microstructures followed by tensile tests without ageing, to study the effect of natural ageing at different cooling rates
- b) Detailed TEM studies to understand the nature of precipitates, on the grain boundaries and within the grain interior, that are formed during cooling and during artificial ageing
- c) Further investigation to explain the mode of fracture in the unrecrystallized alloys, using different magnification SEM images, as it was difficult to characterize them into transgranular and intergranular fracture

- d) Study the effect of grain orientation on the degree of strain localization within the PFZs using the crystal plasticity software, DAMASK

References

1. The Aluminum Association: <https://www.aluminum.org/product-markets/automotive>
2. V. Ramaswamy, R. Pareek, A. Giri, G. Anugula, V. Srivatsa, S. Adhikari, *Corrosion performance evaluation of aluminum alloys for automotive applications*, NCCI, 2012.
3. W. J. Joost, *Reducing vehicle weight and improving U.S. energy efficiency using integrated computational materials engineering*, TMS, 2012.
4. G. Scamans, *Electric vehicles spike demand for high strength aluminum extrusions*, Light Metal Age, 2018.
5. The Aluminum Association: <https://www.aluminum.org/news/unprecedented-growth-expected-automotive-aluminum-multi-material-vehicles-ascend-new-survey>
6. "Basic Metallurgy: 6000 series aluminum extrusion alloys,
<http://www.vosbltd.com/site/wp-content/uploads/2015/10/extrusion-basic-metallurgy.pdf>
7. G. Razaz, *Casting practices influencing inclusion distribution in Al billets*, Thesis, Karlsatds Universitet, 2012.
8. R. E. O. Pelayo, *Direct chill and fusion casting of aluminum alloys*, Thesis, University of Waterloo, 2012.
9. Z. Zhang, Unpublished work, University of British Columbia.
10. Y. L. Liu, S. B. Kang, H. W. Kim, *The complex microstructure in as-cast Al-Mg-Si alloy*, Materials Letters **41**, 1999.
11. C. Liu, *Microstructure evolution during homogenization and its effect on the high temperature deformation behavior in AA6082 based alloys*, Doctoral Thesis, 2017.
12. Y. Birol, *The effect of homogenization practice on the microstructure of AA6063 billets*, Journal of Materials Processing Technology **148**, 2004.

13. N. C. W. Kujipers, W. H. Kool, P. T. G. Koenis, K. E. Nilsen, I. Todd, S. Van der Zwaag, *Assessment of different techniques for quantification of α -Al(FeMn)Si and β -AlFeSi intermetallics in AA 6xxx alloys*, *Materials Characterization* **49**, 2002.
14. Chapter 3, *Influence of heat treatment upon microstructure of casting aluminum alloys*, *Casting Aluminum Alloys, Their Physical and Mechanical Metallurgy*, 2007.
15. G. Zhang, H. Nagaumi, Y. Han, Y. Xu, C. M. Parish, T. Zhai. *Effects of Mn and Cr additions on the recrystallization behavior of Al-Mg-Si-Cu alloys*, *Materials Science Forum* **877**, 2017.
16. X. Wang, J. Qin, H. Nagaumi, R. Wu, Q. Li, *The effect of α -Al(MnCr)Si dispersoids on activation energy and workability of Al-Mg-Si-Cu alloys during hot deformation*, *Advances in Materials Science and Engineering*, 2020.
17. C. L. Liu, Q. Du, N. C. Parson, W. J. Poole, *The interaction between Mn and Fe on the precipitation of Mn/Fe dispersoids in Al-Mg-Si-Mn-Fe alloys*, *Scripta Materialia* **152**, 2018.
18. T. Sheppard, *Extrusion of aluminum alloys*, Kluwer Academic Publishers, 1999.
19. S. J. Andersen, C. D. Marioara, A. Frøseth, R. Vissers, H. W. Zandbergen, *Crystal structure of the orthorhombic U_2 -Al₄Mg₄Si₄ precipitate in the Al-Mg-Si alloy system and its relation to β' and β'' phases*, *Materials Science and Engineering A* **390**, 2005.
20. K. Matsuda, Y. Sakaguchi, Y. Miyata, Y. Uetani, T. Sato, A. Kamio, S. Ikeno, *Precipitation sequence of various kinds of metastable phases in Al-1.0 mass% Mg₂Si-0.4 mass% Si alloy*, *Journal of Materials Science* **35**, 2000.

21. T. Saito, C. D. Marioara, J. Røyset, K. Marthinsen, R. Holmestad, *The effects of quench rate and pre-deformation on precipitation hardening in Al-Mg-Si alloys with different Cu amounts*, Materials Science and Engineering A, 2014.
22. J. K. Sunde, C. D. Marioara, R. Holmestad, *The effect of low Cu additions on precipitate crystal structures in overaged Al-Mg-Si(-Cu) alloys*, Materials Characterization **160**, 2020.
23. L. Ding, Z. Jia, J. Nie, Y. Weng, L. Cao, H. Chen, X. Wu, Q. Liu, *The structural and compositional evolution of precipitates in Al-Mg-Si-Cu alloy*, Acta Materialia **145**, 2018.
24. Y. Weng, Z. Jia, L. Ding, S. Muraishi, X. Wu, Q. Liu, *The multiple orientation relationships and morphology of β' phase in Al-Mg-Si-Cu alloy*, Journal of Alloys and Compounds **767**, 2018.
25. A. Bobel, K. Kim, C. Wolverton, M. Walker, G. B. Olson, *Equilibrium composition variation of Q-phase precipitates in aluminum alloys*, Acta Materialia **138**, 2017.
26. H. Maeng, Y. Choi, S. Lee, *Model of precipitation hardening of Al-Mg-Si alloys under aging*, Materials Science and Heat Treatment **61**, 2019.
27. C. H. Liu, Y. X. Lai, J. H. Chen, G. H. Tao, L. M. Liu, P. P. Ma, C. L. Wu, *Natural-ageing-induced reversal of the precipitation pathways in an Al-Mg-Si alloy*, Scripta Materialia **115**, 2016.
28. M. W. Zandbergen, Q. Xu, A. Cerezo, G. D. W. Smith, *Study of precipitation in Al-Mg-Si alloys by Atom Probe Tomography I. Microstructural changes as a function of ageing temperature*, Acta Materialia **101**, 2015.
29. M. Murayama, K. Hono, M. Saga, M. Kikuchi, *Atom probe studies on the early precipitation in Al-Mg-Si alloys*, Materials Science and Engineering A **250**, 1998.

30. V. Fallah, B. Langelier, N. Ofori-Opoku, B. Raeisinia, N. Provatas, S. Esmaeili, *Cluster evolution mechanism during ageing in Al-Mg-Si alloys*, Acta Materialia **103**, 2016.
31. J. Banhart, C. S. T. Chang, Z. Liang, N. Wanderka, M. D. H. Lay, A. J. Hill, *Natural ageing in Al-Mg-Si alloys - a process of unexpected complexity*, Advanced Engineering Materials.
32. M. Song, I. Kim, J. Kim, S. Hong, *Effect of Cu contents on nanocluster formation and two-step ageing behavior in Al-Mg-Si alloys*, Metals and Materials International, 2019.
33. R. K. W. Marceau, A. de. Vaucorbeil, G. Sha, S. P. Ringer, W. J. Poole, *Analysis of strengthening in AA6111 during the early stage of ageing: Atom probe tomography and yield strength modeling*, Acta Materialia **61**, 2013.
34. J. Kim, E. Kobayashi, T. Sato, *Influence of natural ageing time on two step ageing behavior of Al-Mg-Si-(Cu) alloys*, Materials Transactions **56**, 2015.
35. W. J. Poole, X. Wang, J. D. Embury, D. J. Lloyd, *The effect of manganese on the microstructure and tensile response of an Al-Mg-Si alloy*, Materials Science and Engineering A **755**, 2019.
36. T. Saito, C. D. Marioara, S. J. Andersen, W. Lefebvre, R. Holmestad, *Aberration-corrected HAADF-STEM investigations of precipitate structures in Al-Mg-Si alloys with low Cu additions*, Philosophical Magazine **94**, 2014.
37. L. Ding, A. Orekhov, Y. Weng, Z. Jia, H. Idrissi, D. Schryvers, S. Muraishi, L. Hao, Q. Liu, *Study of the Q'(Q)-phase precipitation in Al-Mg-Si-Cu alloys by quantification of atomic resolution transmission electron microscopy images and atom probe tomography*, Journal of Materials Science **54**, 2019.

38. J. K. Sunde, S. Wenner, R. Holmestad, *In-situ heating TEM observations on evolving nanoscale Al-Mg-Si-Cu precipitates*, Journal of Microscopy, 2019.
39. K. Strobel, M. A. Easton, M. D. H. Lay, P. A. Rometsch, S. Zhu, L. Sweet, N. C. Parson, A. J. Hill, *Quench sensitivity in a dispersoid containing Al-Mg-Si alloy*, Metallurgical and Materials Transactions A **50**, 2019.
40. K. Strobel, M. D. H. Lay, M. A. Easton, L. Sweet, S. Zhu, N. C. Parson, A. J. Hill, *Effects of quench rate and natural ageing on the age hardening behavior of aluminium alloy AA6060*, Materials Characterization **111**, 2016.
41. J. Im, J. Jeon, M. Song, S. Hong, J. Kim, *Influence of natural ageing time and Mg/Si ratio ($Mg + Si = 1.3 \text{ mass\%}$) on the two-step ageing behavior in Al-Mg-Si alloys*, Metals and Materials International **25**, 2019.
42. C. S. T. Chang, I. Wieler, N. Wanderka, J. Banhart, *Positive effect of natural pre-ageing on precipitation hardening in Al-0.44 at% Mg-0.38 at% Si alloy*, Ultramicroscopy **109**, 2009.
43. B. Milkereit, M. J. Starink, P. A. Rometsch, C. Schick, O. Kessler, *Review of the quench sensitivity of aluminium alloys: analysis of the kinetics and nature of quench-induced precipitation*, Materials, 2019.
44. A. H. Geisler, *Phase transformations in solids*, Wiley, 1951.
45. S. Liu, X. Wang, Q. Pan, M. Li, J. Ye, K. Li, Zhuowei Peng, Yuqiao Sun, *Investigation of microstructure evolution and quench sensitivity of Al-Mg-Si-Mn-Cr alloy during isothermal treatment*, Journal of Alloys and Compounds **826**, 2020.
46. M. Conserva, P. Fiorini, *Interpretation of Quench Sensitivity in Al-Zn-Mg-Cu alloys*, Metallurgical Transactions **4**, 1973.

47. K. Strobel, M. A. Easton, L. Sweet, M. J. Couper, J. Nie, *Relating quench sensitivity to microstructure in 6000 series aluminum alloys*, *Materials Transactions* **52**, 2011.
48. B. Milkereit, O. Kessler, C. Schick, *Recording of continuous cooling precipitation diagrams of aluminium alloys*, *Thermochimica Acta* **492**, 2009.
49. B. Milkereit, N. Wanderka, C. Schick, O. Kessler, *Continuous cooling precipitation diagrams of Al-Mg-Si alloys*, *Materials Science and Engineering: A* **550**, 2012.
50. X. Zhang, X. Zhou, J. Nilsson, *Corrosion behaviour of AA6082 Al-Mg-Si alloy extrusion: The influence of quench cooling rate*, *Corrosion Science*, 2019.
51. X. Zhang, X. Zhou, J. Nilsson, Z. Dong, C. Cai, *Corrosion behaviour of Al-Mg-Si alloy extrusion: Recrystallized and non-recrystallized structures*, *Corrosion Science* **144**, 2018.
52. W. J. Poole, X. Wang, D. J. Lloyd, J. D. Embury, *The shearable-non-shearable transition in Al-Mg-Si-Cu precipitation hardening alloy: implications on the distribution of slip, work hardening and fracture*, *Philosophical Magazine* **85**, 2007.
53. D. H. Bratland, Ø. Grong, H. Schercliff, O. R. Myhr, S. Tjøtta, *Modelling of precipitation reactions in industrial processing*, *Acta Metallurgica* **45**, 1997.
54. P. N. T. Unwin, C. W. Lorimer, R. B. Nicholson, *The origin of the grain boundary precipitate free zone*, *Acta Metallurgica* **17**, 1969.
55. D. A. Porter and K. E. Easterling, *Phase transformations in metals and alloys*, Second edition, 1992.
56. N. Yang, P. Saidi, M. R. Daymond, J. J. Hoyt, *Modeling of particle coarsening and precipitation free zones*, *Modelling and Simulation in Materials Science and Engineering*, 2017.

57. T. Saito, C. D. Marioara, J. Røyset, R. Holmestad, *Influence of low copper addition on quench sensitivity of Al-Mg-Si alloys*, *Advanced Materials Research* **922**, 2014.
58. K. Strobel, *Quench sensitivity in 6xxx series aluminum alloys*, Doctoral Thesis, 2013.
59. Z. Yang, X. Jiang, X. Zhang, M. Liu, Z. Liang, D. Leyvraz, J. Banhart, *Natural ageing clustering under different quenching conditions in an Al-Mg-Si alloy*, *Scripta Materialia* **190**, 2021.
60. N. Sarmady, *The effect of quench rate and initial grain structure on the mechanical behavior of an Al-Mg-Si-Mn aluminum alloy*, Thesis, 2018.
61. P. F. Thomason, *Ductile fracture of Metals*, Pergamon Press, 1990.
62. M. J. Worswick, Z. T. Chen, A. K. Pilkey, D. Lloyd, S. Court, *Damage characterization and damage percolation modelling in aluminum alloy sheet*, *Acta Materialia* **49**, 2001.
63. M. F. Ashby, C. Gandhi, D. M. R. Taplin, *Fracture mechanism maps and their construction for F.C.C metals and alloys*, *Acta Metallurgica* **27**, 1979.
64. S. H. Goods, L. M. Brown, *Overview no. 1 – The nucleation of cavities by plastic deformation*, *Perspectives in Creep Fracture*, 1983.
65. F. Hannard, T. Pardoen, E. Maire, C. Le Bourlot, R. Mokso, A. Simar, *Characterization and micromechanical modelling of microstructural heterogeneity effects on ductile fracture of 6xxx aluminium alloys*, *Acta Materialia* **103**, 2016.
66. J. R. Rice, D. M. Tracey, *On the ductile enlargement of voids in triaxial stress fields*, *Journal of Mechanics and Physics of Solids* **17**, 1969.
67. S. K. Yerra, C. Tekoglu, F. Scheyvaerts, L. Delannay, P. Van Houtte, T. Pardoen, *Voids growth and coalescence in single crystals*, *International Journal of Solids and Structures* **47**, 2010.

68. L. M. Brown, J. D. Embury, *The initiation and growth of voids at second phase particles*, 1973.
69. A. Davidkov, R. H. Petrov, P. De Smet, B. Schepers, L. A. I. Kestens, *Microstructure controlled bending response in AA60016 Al alloys*, *Materials Science and Engineering A* **528**, 2011.
70. Drucker (Edited by Victor F Zackay), *High-strength materials*, John Wiley & Sons, 1964
71. T. Pardoen, D. Dumont, A. Deschamps, Y. Brechet, *Grain boundary versus transgranular ductile fracture*, *Journal of Mechanics and Physics of Solids* **51**, 2003.
72. J. D. Evensen, N. Ryum, J. D. Embury, *The intergranular fracture of Al-Mg-Si alloys*, *Materials Science and Engineering* **18**, 1975.
73. A. K. Vasudevan, R. D. Doherty, *Grain boundary ductile fracture in precipitation hardened aluminum alloy*, *Acta Metallurgica* **35**, 1987.
74. S. Thomesen, O. S. Hopperstad, O. R. Myhr, T. Børvik, *Influence of stress state on plastic flow and ductile fracture of three 6000-series aluminum alloys*, *Materials Science and Engineering A* **783**, 2020.
75. P. Castany, F. Diologent, A. Rossoll, J. F. Despois, C. Bezencon, A. Mortensen, *Influence of quench rate and microstructure on bendability of AA6016 aluminium alloys*, *Materials Science and Engineering A* **559**, 2013.
76. G. Bao, J. W. Hutchinson, R. M. McMeeking, *Particle reinforcement of ductile matrices against plastic flow and creep*, *Acta Metallurgica* **39**, 1991.
77. M. Mansouri, N. C. Parson, M. Li, W. J. Poole, *The Dependence of local strain distribution on Quench rate for the extruded Al-Mg-Si-Mn-Fe alloys*, *Light Metals*, 2019.

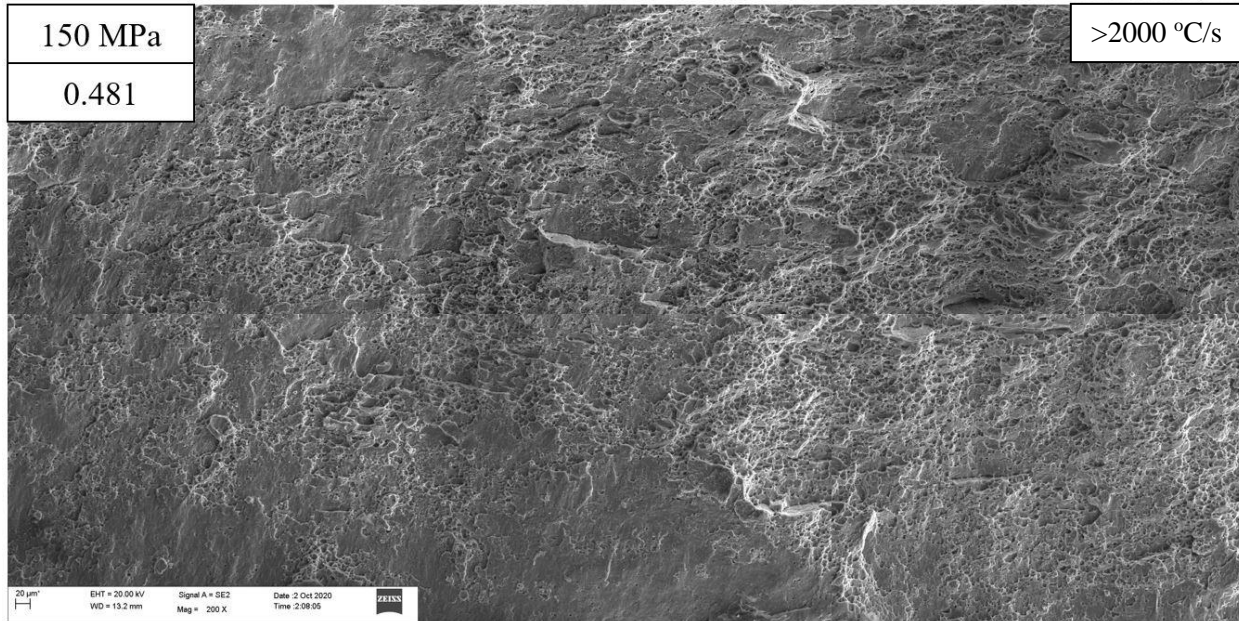
78. M. Khadyako, C. D. Marioara, I. G. Ringdalen, S. Dumoulin, O. S. Hopperstad, *Deformation and strain localization in polycrystals with plastically heterogeneous grains*, International Journal of Plasticity **86**, 2016.
79. B. Frodal, E. Christiansen, O. R. Myhr, O. S. Hopperstad, *The role of quench rate on the plastic flow and fracture of three aluminium alloys with different grain structure and texture*, International Journal of Engineering Science **150**, 2020.
80. P. Eisenlohr, M. Diehl, R. A. Lebensohn, F. Roters, *A spectral method solution to crystal elasto-viscoplasticity at finite strains*, International Journal of Plasticity **46**, 2013.
81. F. Roters, M. Diehl, P. Shanthraj, P. Eisenlohr, C. Reuber, S. L. Wong, T. Maiti, A. Ebrahimi, T. Hochrainer, H. O. Fabritius, S. Nikolov, M. Friak, N. Fujita, N. Grilli, K. G. F. Janssens, N. Jia, P. J. J. Kok, D. Ma, F. Meier, E. Werner, M. Stricker, D. Weygand, D. Raabe, *DAMASK - The Düsseldorf Advanced Material Simulation Kit for modeling multi-physics crystal plasticity, thermal, and damage phenomena from the single crystal up to the component scale*, Computational Materials Science **158**, 2019.
82. DAMASK material properties documentation
<https://damask.mpie.de/bin/view/Documentation/MaterialConfig>
83. M. Mansouri, *Doctral thesis*, University of British Columbia, 2021.
84. D. Steele, D. Evans, P. Nolan, D. J. Lloyd, *Quantification of grain boundary precipitation and the influence of quench rate in 6xxx aluminum alloys*, Materials Characterization, 2007.
85. P. J. J. Kok, *Crystal plasticity based predictions of mechanical properties from heterogeneous steel microstructures*, IOP Conference Series, Materials Science and Engineering, 2019.

86. P. Franciosi, M. Berveiller, A. Zaoui, *Latent hardening in copper and aluminum single crystals*, Acta Metallurgica **28**, 1980.
87. X. Wang, Unpublished TEM work, McMaster university, 2020
88. S. K. Chaudhury, D. Apelian, *Effects of Mg and Cu content on quench sensitivity Al-Si-Mg alloy*, International Journal of Metal Casting **10**, 2016.
89. T. F. Morgeneyer, M. J. Starink, S. C. Wang, I. Sinclair, *Quench sensitivity of toughness in an Al alloy: Direct observation and analysis of failure initiation at the precipitate-free zone*, Acta Materialia **56**, 2008.

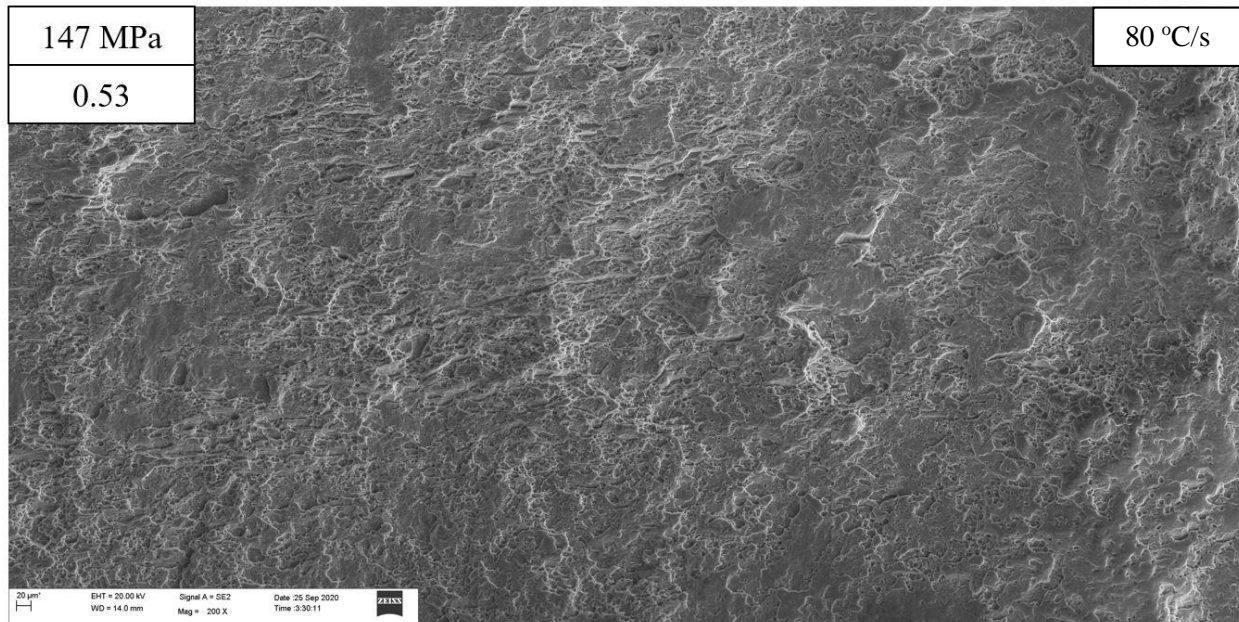
Appendices

Appendix A

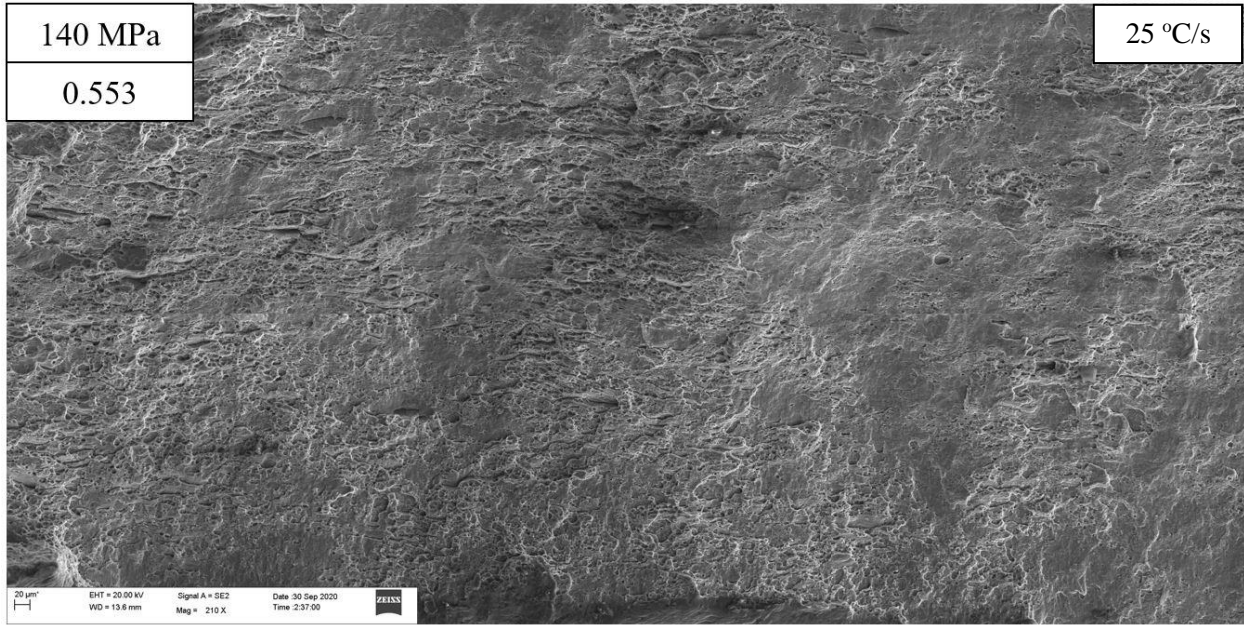
Medium magnification fracture surface maps for a T4 tempered recrystallized alloys.



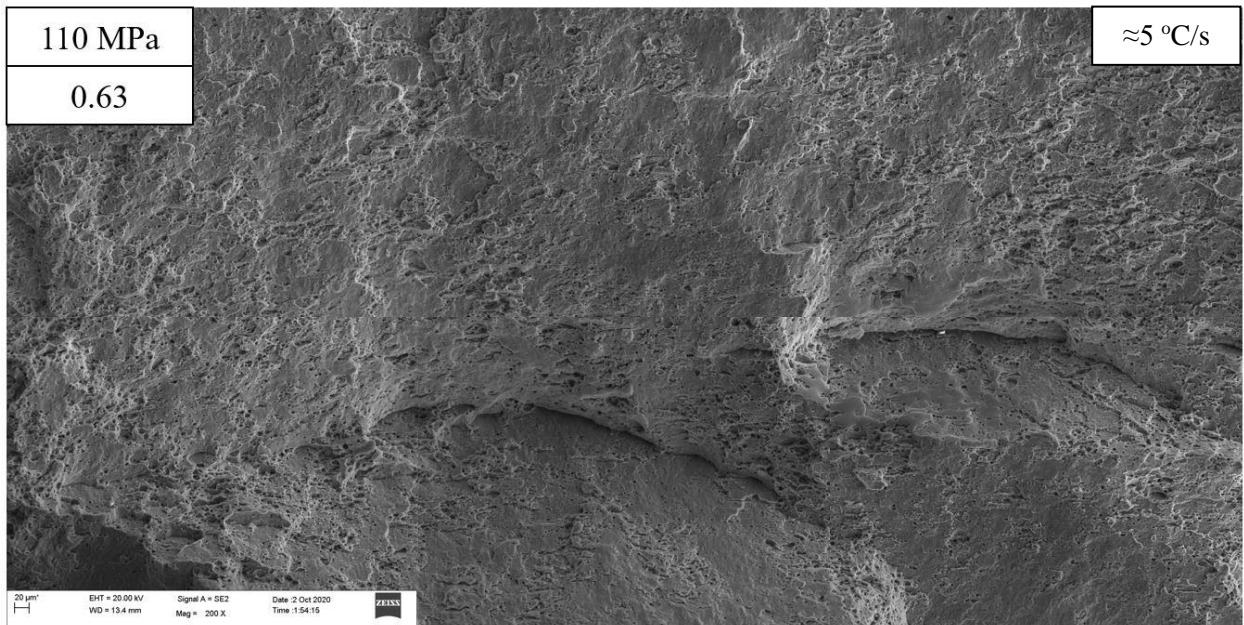
(a)



(b)



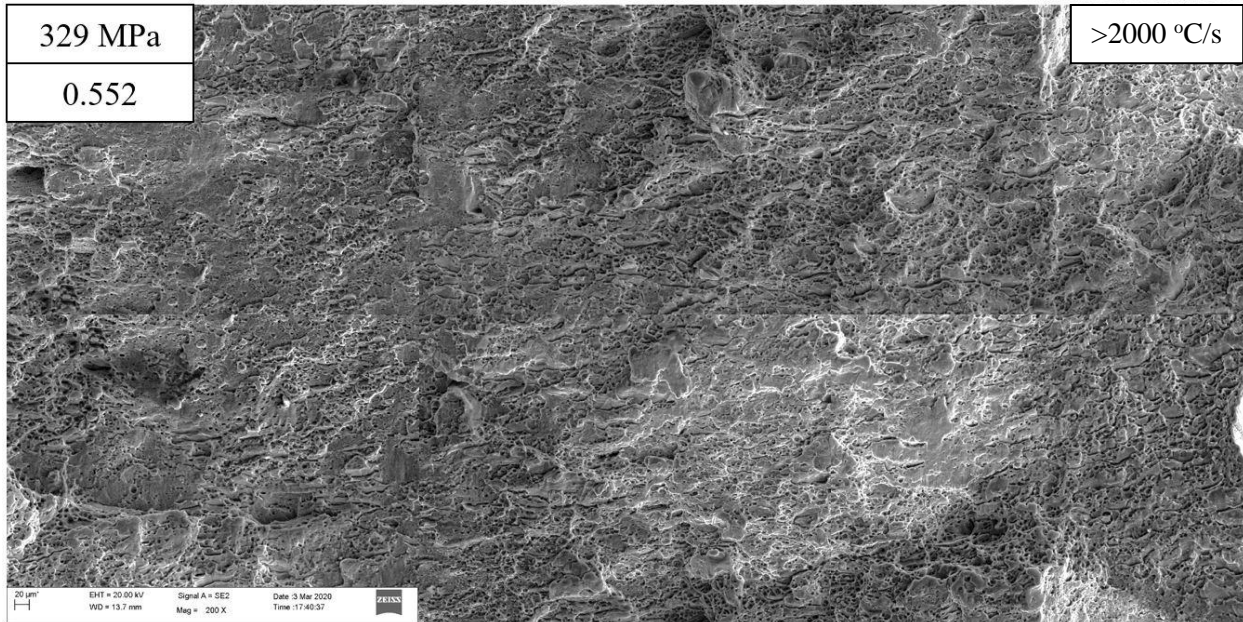
(c)



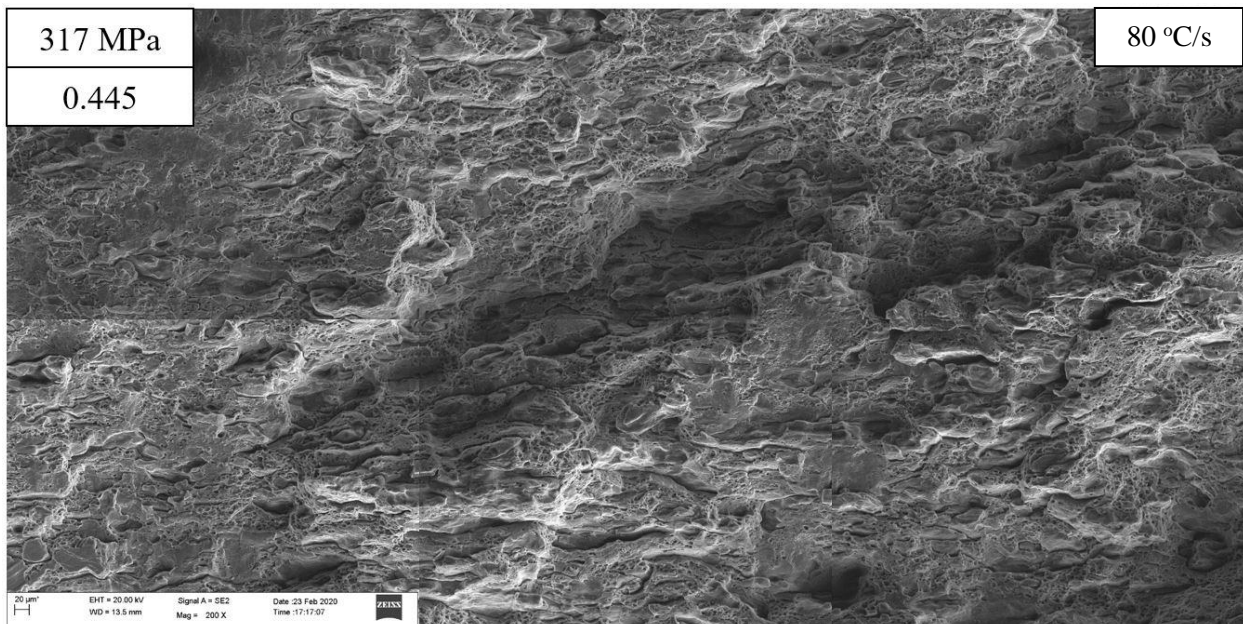
(d)

Appendix B

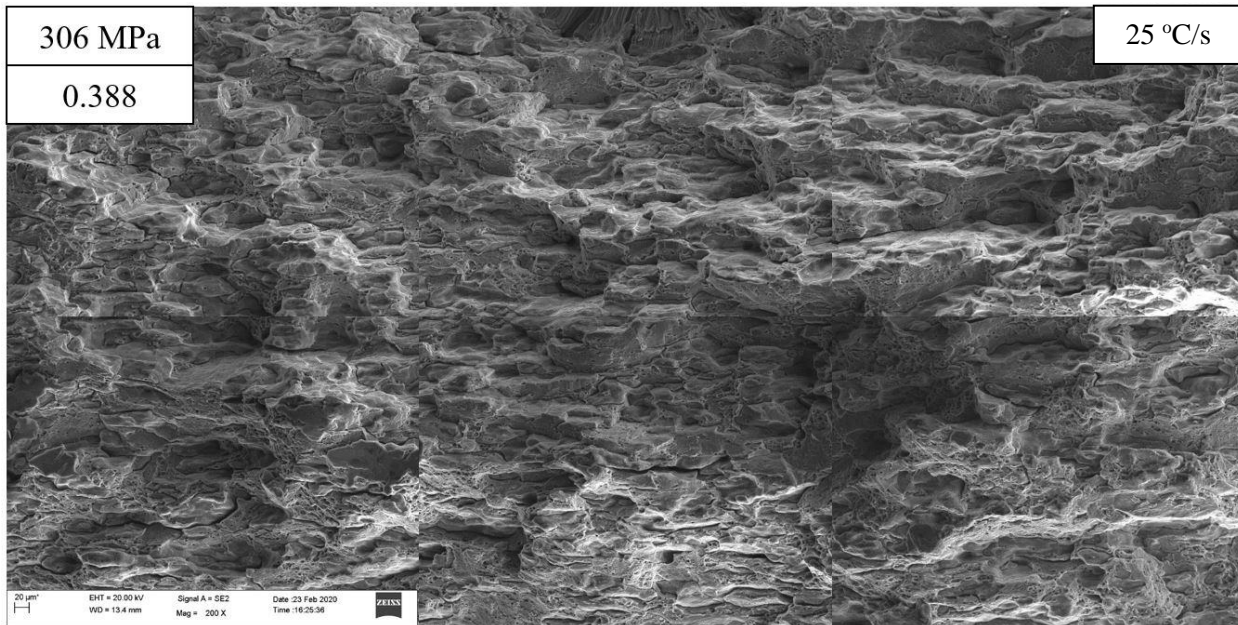
Medium magnification fracture surface maps for a T4 tempered recrystallized alloys.



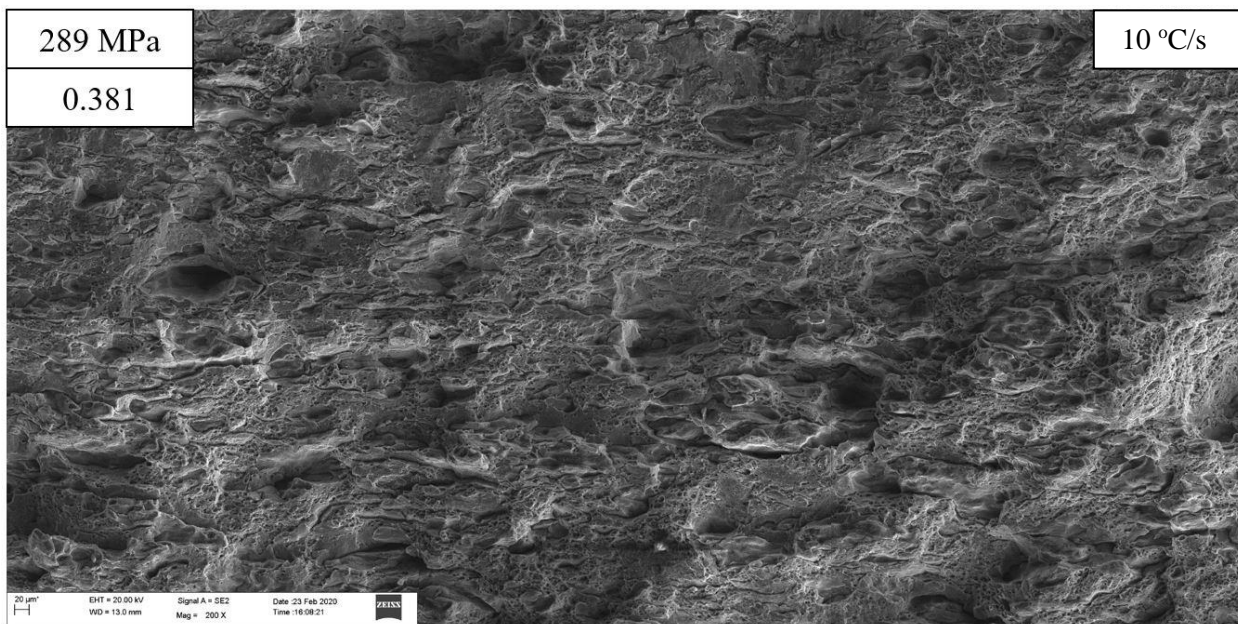
(a)



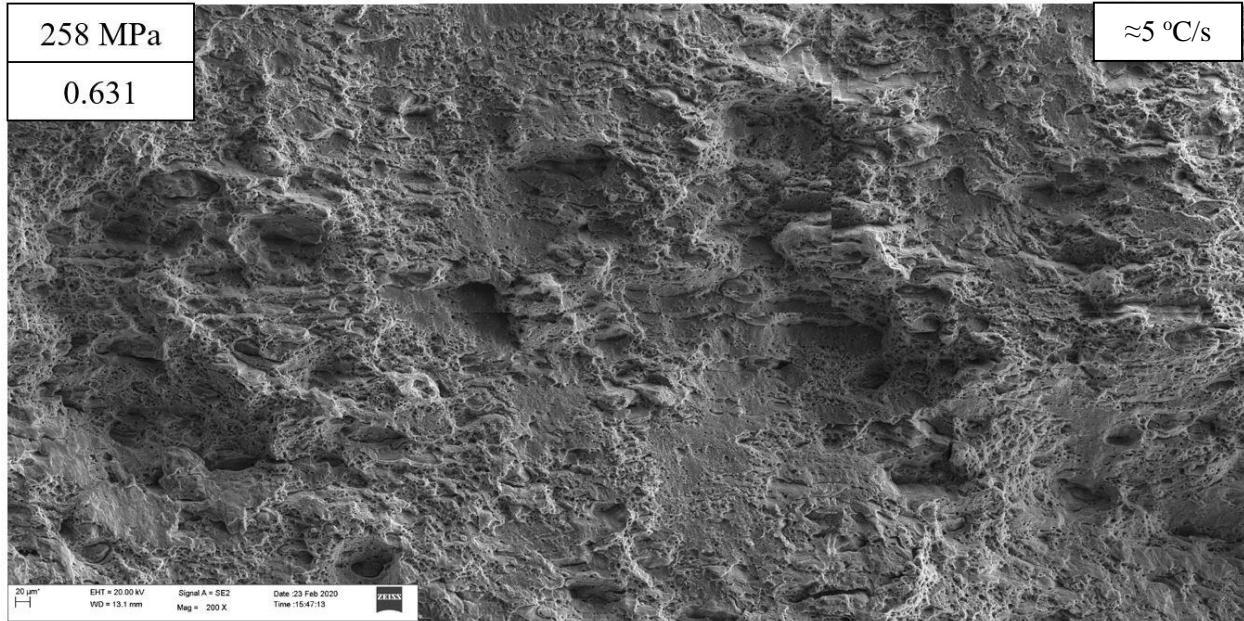
(b)



(c)



(d)



(e)